Preparation of Correlated Many-Body States Using Rydberg Atom Tweezer Arrays

A THESIS PRESENTED
BY
DAVID D. NOACHTAR
TO
THE DEPARTMENT OF PHYSICS

IN PARTIAL FULFILLMENT OF THE REQUIREMENTS
FOR THE DEGREE OF
MASTER OF SCIENCE
IN THE SUBJECT OF
QUANTUM SCIENCE AND TECHNOLOGY

HARVARD UNIVERSITY
CAMBRIDGE, MASSACHUSETTS
NOVEMBER 2023

Thesis advisor: Professor Norman Yao David D. Noachtar

Preparation of Correlated Many-Body States Using Rydberg Atom Tweezer Arrays

Abstract

Programmable quantum simulators have proven a powerful tool for studying strongly correlated matter. In particular Rydberg atoms trapped in optical tweezer arrays have been established as an interesting playground for analog quantum simulation of quantum materials due to their tunable interactions and the ability to arrange hundreds of atoms in a wide range of lattice geometries. Recent investigations have studied a plethora of phases of matter in these systems including spin liquids and antiferromagnets. However, cooling into these phases remains an elusive challenge as adiabatic methods become notoriously difficult upon approaching a phase transition. In this work, we use matrix product state methods to investigate two cooling approaches that engineer the system to act as its own bath.

The first one, *conformal cooling*, involves sudden time evolution under a spatially modulated Hamiltonian to induce a temperature gradient, resulting in entropy flowing from one subsystem into another upon equilibration. Rydberg atom tweezer arrays are a natural candidate for this ansatz due to their precise spatial control. This enables rescaling the interactions between Rydberg atoms by appropriately changing the interatomic distance. We explore the phase diagram of the one-dimensional Rydberg blockade model as an experimentally viable proof of concept. While ergodicity breaking impedes cooling in the $\mathbb{Z}_2$ phase, we identify the critical point between the $\mathbb{Z}_2$ and paramagnetic phases as a promising candidate for preparing low-energy states. Optimizing over the parameters of the spatial modulation, we observe *overcooling* for shallow linear modulations at a transient time scale, wherein the cooling exceeds thermodynamic expectations by more than a factor of 2. We explain this phenomenon in terms of mobile long-lived quasiparticles at the system-bath boundary and investigate its contribution to cooling in the thermodynamic limit. However due to the lack of finite-temperate order in the 1D Rydberg blockade model, cooling into the ground state is required to observe order which posits a challenge. To this end, we propose the 2D Rydberg blockade model as a more promising candidate to perform conformal cooling as it exhibits antiferromagnetic order at finite temperature. Our discussion focuses on potential applications in near-term experimental implementations.

We also investigate a second approach for preparing low-temperature states via thermofield-double (TFD) states. We study the ground state of two locally coupled spin-$\frac{1}{2}$ isotropic Heisenberg chains, which exhibit TFD-like behavior, up to chain lengths of $L = 256$. A comparison of the correlations shows excellent agreement at short distances between the coupled ground state and a corresponding Gibbs state with deviations at long length scales. A perturbative argument for small

coupling strengths g predicts these deviations to vanish, provided that the energy gap between the ground state and first excited state scales sublinearly in g. Our results indicate a linear gap scaling in good agreement with conformal field theory predictions, resulting in a nonvanishing first-order correction to the ground state. Finally we discuss the adiabatic preparation of this ground state to perform finite-temperature quantum simulation. A key advantage over existing methods is the guarantee of a nonvanishing gap along the adiabatic path, making it suitable for finite-temperature quantum simulation on near-term experiments.

Contents

Listing of figures

This work is dedicated to my family and friends who accompanied and joined me along this 402-day journey.

Acknowledgments

How much can a place change you? Over the past year, I had the rare chance to experience this first hand. My time at Harvard University in the group of Professor Norman Yao has left a deep impact on me, both scientifically and personally. While this thesis officially marks the end of this incredible chapter of my life, I am certain that there is more to come and I am grateful for all of the opportunities it has provided me so far. From learning exciting physics, meeting and getting to know inspiring people, to a plethora of new experiences, Cambridge has become a second home for me and will always have a special place in my heart, no matter where I might find myself.

First and foremost, I want to thank my advisor, Professor Norman Yao, for all of his support. Norm took me in when I was looking for a change of scenery, unsure of what would come next, and welcomed me into his group. From the moment I met him in March 2022, his endearing attitude has fascinated me. He helped me grow as a person and a scientist alike and encouraged me to continue challenging myself. When it felt like little progress was being made, Norm taught me how to refocus, take a step back and consider the broader picture. Whenever I was in need of encouragement, he would found the words to nudge me in the right direction. He always took time whenever I needed to talk, be it about science or personal life—acknowledging both the difficulties and successes alike. I also want to express my gratitude for supporting and guiding me through the process of graduate applications. While it was certainly difficult and took a toll on me, Norm provided a voice of reason and encouragement when I needed it. I could write a lot more to express how thankful I am to have worked with Norm, but in the spirit of keeping things to the point, I will encapsulate it in one sentence. This has been the most transformative year of my life in many ways and I am eternally grateful to Norm for this experience.

I also want to thank Professor Ignacio Cirac for supporting my decision to pursue my master's thesis in the US and recommending Norm as a potential advisor. While this was certainly not the easy way, ultimately it was the right path for me and I am thankful for his insights and advice.

My year in Norm's group would not have been as inspiring, exciting, and entertaining without the wonderful members of the group. Sabrina Chern, Julia Wei and Andrea Pizzi were essential in making me feel welcomed and introducing me to the group. Thanks to your kindness I felt in the right place from the moment I joined the group. I also want to highlight and thank Maxwell Block who supported me on both of my projects. There are few people—if any—who have had as much of an impact on my scientific approach and thinking and I could not have asked for someone better

to work with. He understood my strengths and weaknesses and always took the time to discuss my results, always looking for next steps. The same goes for Sabrina who provided me with valuable feedback when I was unsure where to go or what to do next. The opportunity to work closely with Sabrina and Max has taught me a lot and was an important influence for me to pursue a doctoral degree. Johannes Feldmeier inspired me with many new ideas to pursue in a crucial phase of the project. I want to thank Jack Kemp, Bryce Kobrin and Tommy Schuster for their help and support with the TFD project. Jack took many hours to introduce me to conformal field theory and taught me the basics of how to apply it in practice. He guided me through an essential stage of this project and helped me bring light to our observations. Bryce provided me with the bigger picture and motivation behind this project when I needed it and gave me a new perspective on how to think about quantum thermalization.

It was my great pleasure to share an office with Helia Kamal—I could not have imagined a better office mate than her. Whenever I needed a break from work or just someone to talk to, she was always happy to join me and get distracted for a moment. I want to thank all of the Yao theory group for insightful discussions over lunch and during coffee breaks. Vincent Liu and Marcus Bintz inspired me to read up about the newest tensor network techniques, Dominik Kufel got me excited about quantum neural states and Philip Crowley taught me about the intricacies of interpreting superconductivity measurements. Esther Wang and Yi Tan were the perfect companions when it came to building the new group website. Outside of the Yao group, there were many amazing people I got to interact with who welcomed me into the community—I want to highlight Eirini Mandopoulou, Oriol Rubies Bigordà and Yi Zhu. The Harvard physics football get-togethers provided a weekly opportunity to forget about quantum physics and have a good time with great competitors including Francisco Machado, Johannes Feldmeier and Gabriel Lamanuzzi.

I am grateful to Kari and Caleb Kuelzer for hosting me in their home. Over the past year, they were my first point of contact for any question, be it inside tips for Cambridge or advice on how to make the perfect dough. From the moment I arrived in the US they made me feel at home and treated me as part of their family, always having an open ear when I needed one.

Sasha Geim turned my world upside down and made my year in Cambridge all the more memorable. She was the best thing that could have happened to me and made the time more special than it already was. From exploring the greater Cambridge and Boston area to taking late-night walks around Mount Auburn, the time spent together was the best part of my year. I am forever thankful to you for all of the lovely memories and hopefully many more to come.

My friends in Munich, in particular Anna-Lena Huber and Alina Ruprecht, supported me in the difficult decision to leave my home. Knowing that they were always only a phone call away gave me a peace of mind. I am glad to have such close, kind and encouraging friends whenever I return to Munich.

Finally, I want to thank my parents, Regine and Soheyl Noachtar, for supporting me through every step of my journey. Our weekly phone calls eased the difficulty of leaving Munich. During their visit to Cambridge I had the pleasure of introducing them to this wonderful place. My sister Isabel Noachtar, who keeps inspiring me to pursue the (sometimes rocky) path towards obtaining a doctoral degree, and Mario Harms, who for the past 12 years has has made me feel like his brother,

are the greatest travel companions and I am looking forward to exploring many new places with them. It is a special gift to have such a supportive family and I am truly grateful to have them by my side.

I want to conclude this by saying that I could not have imagined a better experience and I think that it was in large due to the fantastic and inspiring people that crossed my path. I will forever cherish the beautiful memories from this time and end with a fitting quote:

> *How lucky I am to have found something that makes saying goodbye so hard.*

0

Introduction

The study of phases of matter has a long tradition in physics. Generations of physicists, dating back to the ancient Greeks, have dedicated their work towards answering the fundamental question: which unique forms can matter take? Interestingly the study of the forms, or phases, of matter is subtle. While there are four common phases of matter (solid, liquid, gas and plasma) that the reader may be familiar with, an expansive catalogue has been discovered. Nowa-

days, efforts to explore these novel phases of matter and the transitions between them are at the heart of condensed matter and statistical physics. Among this plethora are crystals, superconductors, and Bose-Einstein condensates which have been extensively studied over the last century. These examples and many more fall under the Ginzburg-Landau paradigm describing symmetry-breaking phase transitions with local order parameters. Recently, more unconventional phases not captured by this formalism including topological ones have garnered attention.

A common aspect of all of the aforementioned exotic phases is that they emerge as a thermodynamic control parameter, most commonly the temperature, is tuned resulting in transitions between distinct phases. In condensed matter physics these transitions have historically been studied in solid-state materials, where well-established methods enable ever colder regimes: Liquid nitrogen can be used to reach 77 K and liquid helium is often used to cool to temperature of 4 K. Using state-of-the-art dilution fridges experiments can reach temperatures as low as 10 mK—sufficiently cold for the emergence of many interesting phases of matter. Specialized methods like adiabatic demagnetization can go beyond these limits in some cases.

Nevertheless these systems are ultimately limited by the tunability of the physical parameters. In 1982 Richard P. Feynman proposed an idea to improve the flexibility of materials that can be studied [17]: what if we built fully controllable synthetic quantum systems that we can use to simulate complicated models? Four decades later this is indeed becoming a reality. To complement conventional solid-state physics, extensive development of quantum simulation techniques enable engineering quantum many-body systems out of individual atoms, ions and photons. This enables a tremendous degree of control over the Hamiltonian—a feature largely absent in traditional condensed matter. There are two sides to this coin however: The precise control over the system parameters arises by isolating the system from the environment. At the same time this isolation makes it challenging to remove energy and entropy from the system.

The emergence of these platforms for quantum simulation has stimulated the development

of new strategies for cooling these systems to prepare low-entropy quantum states. They can be roughly grouped into three categories:

1. adiabatic preparation,
2. optimal control theory, and
3. engineering a subsystem of the system to act as its own bath.

We note that these methods are designed for analog quantum devices where one has some control over the Hamiltonian. Digital quantum computers, which make use of a discrete set of logical operations known as gates, have access to other methods including variational[75,86,37,80] or algorithmic cooling approaches[92].

Adiabatic preparation is based on the adiabatic theorem: if the Hamiltonian of a system is slowly changing, then the system will remain in the instantaneous ground state at all points during the evolution. In principle, this is a powerful method to prepare complex many-body states. Given a Hamiltonian $\mathcal{H}_0$ whose ground state $|\psi_0\rangle$ is easy to initialize, the target ground state $|\psi_1\rangle$ of Hamiltonian $\mathcal{H}_1$ is prepared by evolving under the Hamiltonian $\mathcal{H}(s) = (1-s)\,\mathcal{H}_0 + s\,\mathcal{H}_1$, where $s(t=0) = 0$. If $s(t)$ changes sufficiently slowly, then the adiabatic theorem guarantees that the final state for $s = 1$ is $|\psi_1\rangle$. However, the time scale for ensuring adiabaticity during the evolution is determined by the inverse gap of the Hamiltonian, i.e., the energy difference between the ground and the first excited state. Crossing a phase transition or critical point is accompanied by the gap becoming arbitrarily small, increasing the time scale for cooling unfavorably. While it can be successfully employed in some cases[4,7,14,64,59], the capabilities of adiabatic preparation are limited as interests shift to increasingly large and higher dimensional systems.

The second approach, optimal control theory, broadly involves optimizing an objective function via time-dependent control parameters given physical constraints. Historically, this has been applied

in a wide array of fields spanning from macroeconomics to aeronautics[34], for example to minimize the fuel use of spacecrafts by dynamically adjusting the rocket thrust. In the context of preparing low-temperature many-body states, this approach is often referred to as *shortcuts to adiabaticity*. In comparison to adiabatic preparation, where the leakage into excited states is avoided entirely, this approach aims to reproduce the final state by strategically taking faster shortcuts through excited states. Generically this requires elaborate time-dependent control of system parameters. It has led to improvements in atomic state preparation, in particular the stimulated Raman adiabatic passage[79], and faster quantum gates as recently demonstrated by Evered et al.. While the last decade has seen the development of various approaches and applications to engineered quantum systems, no encompassing theory exists[22]. For a comprehensive review of this topic, see the work by Guéry-Odelin et al..

The last approach is centered around engineering a subsystem to behave as the bath for the rest of the system[90,36], shifting entropy or energy from one subsystem into another. In the context of trapped atoms, this idea was brought up as early as 2009[69]. Since then, several approaches have been proposed including shifting entropy from one atomic species to another, seeking to trap excitations in the edge of the system to remove energy from the bulk and minimize finite size effects[36], or engineering an effective temperature gradient by partially rescaling the Hamiltonian of the system[90]. The latter idea is known as *conformal cooling*[90] and is a focus of this thesis*.

Outline

Here we investigate the first and third strategy as candidates for cooling engineered quantum many-body systems, i.e., adiabatic preparation and engineering the system to be its own bath. This thesis is organized as follows: Chapter 1 is dedicated to conformal cooling quenches. We first provide in-

*To avoid confusion, we note that conformal cooling refers to the approach proposed by Zaletel et al.. Coincidentally, it also refers to an unrelated method in plastic moulding.

tuition including thermodynamic arguments in Sec. 1.1, then we discuss Rydberg atoms trapped in tweezer arrays as natural candidates for implementing this protocol, and investigate the efficacy of this procedure throughout its phase diagram. Section 1.2.2 presents numerical results that demonstrate substantial cooling at the critical point between the disordered and the ordered phase which we will subsequently study in detail.

Another approach to engineering a system to be its own bath is by preparing a state whose reduced state on one half of the system is given by a thermal state. This is the case for the thermofield-double (TFD) state. In Ch. 2 our focus shifts towards the adiabatic preparation of the TFD in coupled chains. In Sec. 2.1 we highlight the motivation for preparing low-energy thermal states and present recent insights in this field from high-energy physics. We point out advantages of the proposed adiabatic approach to study low-temperature phases of matter over traditional approaches. In particular we demonstrate that dealing with vanishing gaps is generally less problematic. We study this protocol in the spin-$\frac{1}{2}$ isotropic Heisenberg model, where we combine numerical results with conformal field theory predictions to make encouraging findings for long chains.

Finally, we discuss our results in Ch. 3 with a focus on near-term implementation in Rydberg atom tweezer arrays. We conclude with insights into alternative experimental investigations as well as long-term prospects and challenges for the proposed approaches to cooling engineered many-body systems.

It is assumed throughout this work that the reader is familiar with quantum mechanics, the Dirac notation and two-level systems on the level of the Bloch sphere. For the remainder of this thesis we work with natural units, i.e., $\hbar = k_{\mathrm{B}} = 1$ for Planck's constant and the Boltzmann constant. We refer to relevant references and reviews for interested readers.

1

Conformal Cooling Quenches

The most natural way of cooling a physical system is to introduce a colder environment: putting an ice cube into a hot tea will eventually cool down the liquid to a more pleasant temperature. Conformal cooling borrows this idea for engineering a many-body system to be its own bath. This chapter focuses on using quenches under spatially deformed Hamiltonians to transfer entropy and energy out of the system of interest. Our results demonstrate substantial removal of

energy—beyond expected values—within experimentally viable time scales, although this cooling remains insufficient for the observation of ordered phases.

1.1 Intuition for Conformal Cooling

Introduced by Zaletel et al., conformal cooling works by spatially modulating the magnitude of the Hamiltonian in a subsystem. Imagine rescaling the Hamiltonian $\mathcal{H}$ to $\mathcal{H}' = \lambda\mathcal{H}$ ($\lambda > 0$) as is illustrated in Fig. 1.1a), thereby changing the energy scale from E to $E' = \lambda E$. Thermodynamic considerations then provide intuitive arguments. Conventionally, temperature is defined as the inverse derivative of the entropy at a given energy,

$$T = \left(\frac{\partial S}{\partial E}\right)^{-1}, \tag{1.1}$$

where S denotes the entropy and E is the energy. The temperature changes according to

$$T' = \left(\frac{\partial S}{\partial E'}\right)^{-1} = \left(\frac{\partial S}{\partial E}\frac{\partial E}{\partial E'}\right)^{-1} = \lambda\left(\frac{\partial S}{\partial E}\right)^{-1} = \lambda T \tag{1.2}$$

as is readily seen from Eq. (1.1).

While this lowers the temperature of the system, this is not helpful by itself: after all the goal is to reach low-entropy states, yet the entropy and the state is unaffected by this process. However, if brought in contact with a system at temperature T with respect to $\mathcal{H}$, this creates a temperature gradient across the two subsystems. Note that we refer to the subsystem with Hamiltonian $\lambda\mathcal{H}$ as the *bath* and the one with Hamiltonian $\mathcal{H}$ as the *system*. Following global thermal equilibration, the system and bath are left at some temperature T_f with $\lambda T < T_\mathrm{f} < T$. As seen in Fig. 1.1a) this generically implies a decrease in entropy as well—thus fulfilling the initial premise that we had set out for.

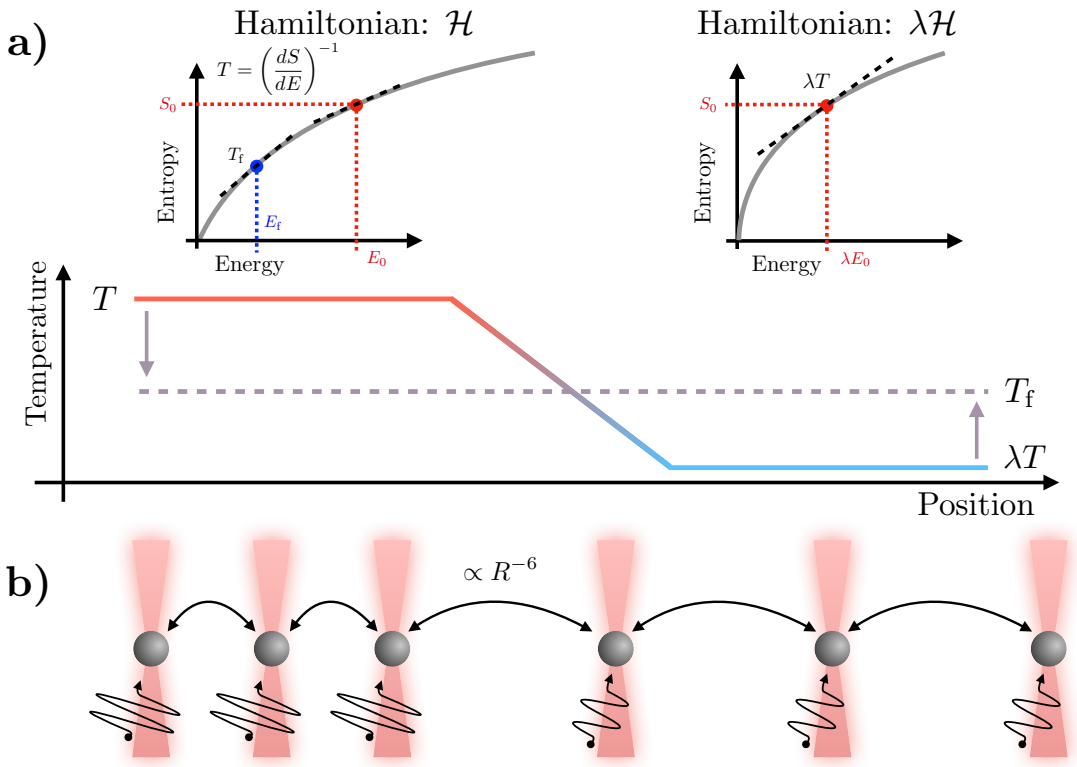

Figure 1.1: An illustration of conformal cooling. **a)** Rescaling the Hamiltonian $\mathcal{H}$ results in an equivalent change in temperature. Spatially modulating the magnitude of the Hamiltonian from $\mathcal{H}$ to $\lambda\mathcal{H}$ ($0 < \lambda < 1$) in a subsystem creates a temperature gradient from T to λT. After equilibration the entire system will be left at some final temperature T_f, therefore lowering the entropy in the strongly interacting subsystem on the left. **b)** Rydberg atoms in tweezer arrays are naturally amenable to conformal cooling due to the spatial control of optical tweezers and therefore the der Waals-interactions, which are proportional to R^{-6} with the interatomic distance R. As later discussions will show, this platform requires the spatial modulation of laser fields (shown as black waves). We note that this figure was inspired by Zaletel et al..

Conservation of energy determines the final temperature T_f. In a canonical ensemble the energy-temperature relation is given by

$$E(T) = \frac{1}{\mathcal{Z}} \mathrm{Tr}\left[\mathcal{H} \exp\left(-\frac{\mathcal{H}}{T}\right)\right], \tag{1.3}$$

where $\mathcal{Z} = \mathrm{Tr}\left[\exp\left(-\mathcal{H}/T\right)\right]$. For sufficiently small system sizes this can be obtained from the full spectrum of $\mathcal{H}$. Given two subsystems S of size N_S and B of size N_B with Hamiltonians H_S and

$H_B = \lambda H_S$, we can compare the initial energy and the energy after equilibration

$$(N_S + \lambda N_B) E_S(T_i) = N_S E_S(T_f) + \lambda N_B E_S\left(\frac{T_f}{\lambda}\right).$$

$E_S(T)$ is the energy-temperature relation in S and T_i is the initial temperature in the system. Note that the energy-temperature relation of B is related to E_S by

$$E_B(T) = \lambda E_S\left(\frac{T}{\lambda}\right)$$

which follows directly from Eq. (1.3). In general we consider systems on a discrete lattice with smooth deformations $\lambda_i \in [0, 1]$. In this case we use

$$\sum_{i=1}^{N} \lambda_i E_S(T_i) = \sum_{i=1}^{N} \lambda_i E_S\left(\frac{T_f}{\lambda_i}\right), \tag{1.4}$$

to determine the final temperature given T_i.

Conformal cooling makes two key assumptions: First, that the system and bath will equilibrate if left in contact for long enough. The eigenstate thermalization hypothesis (ETH) justifies this assumption for nonintegrable models. While discussing the full extent of quantum thermalization goes beyond the scope of this thesis, interested readers find a short review of thermalization in close quantum systems with a focus on ETH and integrability in App. B. Second, it relies on the ability to spatially modulate the Hamiltonian. While there are multiple experimental platforms that fulfill these two requirements, here we choose to focus on Rydberg atoms trapped in tweezer arrays. In the following section we introduce the Hamiltonian of this platform and discuss why it is a natural candidate for conformal cooling.

Rydberg Atom Tweezer Arrays

Developed in the context of optical dipole trapping, optical tweezers are laser beams with widths on the order of a micrometer. This method was originally employed in biology to capture and study single cells, bacteria and large molecules [3]. A key advantage of this technology is its spatial controllability. A single laser beam can be split to create an array of optical tweezers that can be spatially arranged into almost any geometry in 1D and 2D. The trapping of single neutral atoms has sparked interest in the quantum many-body community for the purpose of quantum simulation.

Atoms with a highly excited electron in a Rydberg state $|\mathrm{r}\rangle$ with principal quantum number $n \gg 1$ are also called *Rydberg* atoms and have a large dipole moment because of the large distance between the nucleus and the electron which scales as $\propto n^2$ [94]. In contrast to $|\mathrm{r}\rangle$, the electronic ground state $|\mathrm{g}\rangle$ with $n \sim 1$ has a negligible dipole moment (on the order of 10^{-3} times smaller than for the Rydberg state [4]). This is important because the atoms interact via dipole-dipole interactions with a R^{-3} dependence on the interatomic distance R. Due to the disparity in dipole moment, interactions involving the electronic ground state are insignificant.

However, two atoms in the same Rydberg state experience a strong interaction that is commonly referred to as *Rydberg blockade*. While dipole-dipole interactions turn out to be highly offresonant [94], van der Waals interactions with a R^{-6} dependence on the interatomic distance R are the dominant contribution. This corresponds to a two-photon process: First, one atom emits a photon that the other one absorbs. Then that process is reversed, returning the population back to its original state. In mathematical terms we write the interaction between two atoms separated by the distance R as

$$V_{\mathrm{int}} = \frac{C}{R^6}\, \hat{n}_1 \otimes \hat{n}_2. \tag{1.5}$$

Here we introduce the projector into the Rydberg state $\hat{n}_i = |\mathrm{r}_i\rangle\langle\mathrm{r}_i|$ (i=1,2) and the van der

Waals coefficient $C \propto n^{11}$ which strongly depends on the principal quantum number[94]. $\otimes$ denotes the tensor product. To induce these interactions, the atoms can be coherently excited from $|\mathrm{g}\rangle$ to $|\mathrm{r}\rangle$ by a near-resonant laser field with Rabi frequency $\Omega > 0$ and detuning $\Delta \in \mathbb{R}$. The resulting Hamiltonian of N Rydberg atoms in a tweezer array reads

$$\mathcal{H} = \sum_{1 \leq i < j \leq N} V_{ij}\, \hat{n}_i \otimes \hat{n}_j + \sum_{i=1}^{N} \left(\frac{\Omega}{2}\, \hat{\sigma}_i^{\mathrm{x}} - \Delta\, \hat{n}_i \right), \tag{1.6}$$

where $\hat{\sigma}^{\mathrm{x}} = |\mathrm{g}\rangle\langle\mathrm{r}| + |\mathrm{r}\rangle\langle\mathrm{g}|$ is a Pauli operator corresponding to a Rabi drive and $V_{ij} = C/(r_{ij}^6)$ the interaction between Rydberg atoms—r_{ij} is the distance between sites i and j. We note that any distance is given in units of the characteristic lattice spacing a.

It is useful to define the Rydberg blockade radius, R_{b}, such that $C = \Omega R_{\mathrm{b}}^6$. The name originates from the repulsive interaction V_{ij} between atoms in the Rydberg state. Given two atoms with one in the Rydberg state and the other in the electronic ground state, it is highly energetically unfavorable to excite the second atom at the same time if they are separated by less than R_{b}—thus one atom is effectively *blocking* the other from being in the Rydberg state.

As a central goal of this thesis is to prepare low-entropy many-body states, we introduce the phase diagram of the Rydberg atom array Hamiltonian on a one dimensional lattice with regular interatomic spacing a. For $R_{\mathrm{b}} < 1$, the interactions are sufficiently weak such that the atoms behave practically independently in the ground state, resulting in a disordered phase. For $R_{\mathrm{b}} > 1$ we find that the disordered phase persists at large negative detuning due to atoms in the Rydberg state being energetically unfavorable. However as Δ is tuned to positive values, the Rydberg state becomes energetically favorable competing with the cost of the repulsive van der Waals interaction between neighboring sites. For $\Delta \gtrsim \Omega$, this results in an ordered phase with two degenerate ground states alternating between $|\mathrm{g}\rangle$ and $|\mathrm{r}\rangle$—therefore breaking $\mathbb{Z}_2$ translation symmetry. This is analogous to antiferromagnetic order in quantum magnetism and was first discovered by Bernien et al.. The

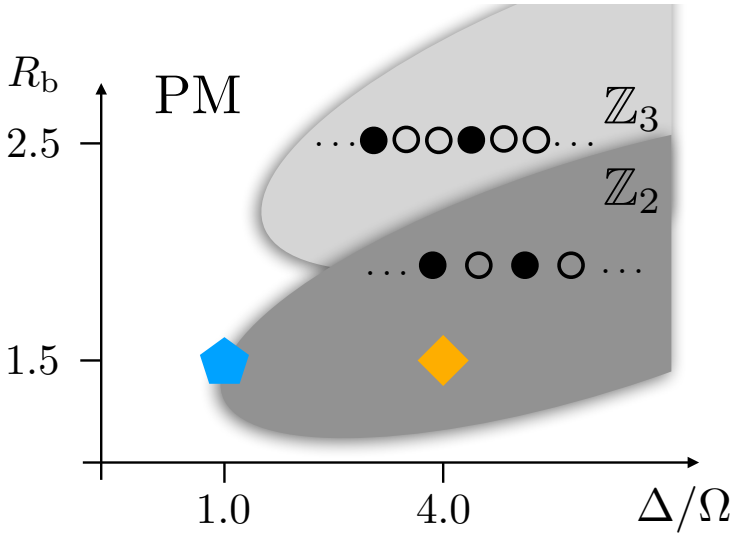

Figure 1.2: Ground state phase diagram of the one-dimensional Rydberg atom tweezer array. The relevant parameters are the blockade radius R_b in units of the lattice spacing a and the ratio between the laser detuning and the Rabi frequency, Δ/Ω. At $\Delta/\Omega \leq 0$ the ground state is paramagnetic resulting in a disordered phase. As Δ/Ω is increased for $R_\mathrm{b} > 1$, ordered phases arise that break $\mathbb{Z}_n$ translation symmetry—this is illustrated for the $\mathbb{Z}_2$ and $\mathbb{Z}_3$ phases. The blue pentagon and orange square correspond to the parameter points that are subject to our investigation: the critical point at $\Delta/\Omega = 1$ and the $\mathbb{Z}_2$ phase at $\Delta/\Omega = 4$ for $R_\mathrm{B} = 1.5$. For more information, we refer to the main body.

phase transition between the ordered and disordered phases falls into the Ising universality class, which is described by a conformal field theory of central charge $c = \frac{1}{2}$—similar to the critical point of the transverse-field Ising model[68].

As R_b is tuned to larger values, the blockade radius encompasses multiple lattice sites and ordered phases emerge with a unit cell of n sites of which only one is in the Rydberg state. These phases have $\mathbb{Z}_n$ order and break $\mathbb{Z}_n$ translational symmetry. The ground state is denoted $|\mathbb{Z}_n\rangle$ and is n-fold degenerate given by n possible sites for the Rydberg excitation in the unit cell. An illustration of the phase diagram is given in Fig. 1.2.

The system also has a natural mapping to a spin-$\frac{1}{2}$ Ising model by identifying $\hat{n} = (\hat{\sigma}^z + \mathbb{I}_2)/2$ with the Pauli operator $\hat{\sigma}^z = |\mathrm{r}\rangle\langle\mathrm{r}| - |\mathrm{g}\rangle\langle\mathrm{g}|$, where $\mathbb{I}_2$ is the identity matrix of a two-level system, thereby mapping Eq. (1.6) to a mixed-field Ising chain which has been extensively studied in the

literature (cf. App. C). For finite transverse and longitudinal fields, this model is nonintegrable, i.e., it does not have an extensive number of quasi-local conserved quantities, and is expected to thermalize according to the ETH. This means that the Rydberg atom array naturally satisfies the first key assumption that we made for conformal cooling.

Recalling the second key assumption—the ability to spatially modulate the Hamiltonian, we go back to Eq. (1.6). We can see how to spatially modulate the magnitude of the interaction Hamiltonian in the limit of nearest-neighbor interactions ($V_{ij} = 0$ for $|i-j| > 2$). Let $r_{i,i+1}$ be the distance between sites i and its nearest neighbor $i+1$. Then, we find that rescaling the interaction term by λ can be achieved by changing the interatomic separation from $r_{i,i+1}$ to $r'_{i,i+1} = r_{i,i+1}/(\lambda^{-\frac{1}{6}})$:

$$\lambda \frac{C}{r_{i,i+1}^6} = \frac{C}{(r_{i,i+1}/\lambda^{-\frac{1}{6}})^6} = \frac{C}{r_{i,i+1}'^6}. \tag{1.7}$$

This is also where conformal cooling gets its name: the interaction is spatially modulated by adjusting the distance between the atoms, which trivially corresponds to a conformal transformation in 1D systems.

In addition, the single-site terms corresponding to the laser fields also have to be rescaled appropriately, e.g., by applying a spatially varying light shift on the transition between $|\mathrm{g}\rangle$ and $|\mathrm{r}\rangle$. There are also experimental proposals for single-site addressing using individual laser beams [87,81], however, this is not scalable.

Both of these aspects are achievable in near-term experimental platforms. In fact the precise real-time control over the atomic positions is a distinguishing feature of tweezer arrays over alternative platforms [5,29]. This is in large achieved using acousto-optical deflectors (AOD) to dynamically change the laser potentials of the atomic traps [29]. Groups around the world are also exploring options for single-site resolved laser fields using AODs [1]. Fig. 1.1b) illustrates a proposal for conformal cooling in Rydberg atom arrays.

In conclusion the Rydberg atom array in one-dimensional systems fulfills the two key ingredients for conformal cooling: the ability to spatially modulate the magnitude of the Hamiltonian and dynamics that tend towards thermal equilibrium.

1.2 Conformal Cooling Quenches in the Rydberg Phase Diagram

In the following section, we explore conformal cooling quenches as a means of preparing low-entropy states starting from disordered states. Recalling our aim of probing ordered ground states, we are primarily interested in the $\mathbb{Z}_2$ phase of Fig. 1.2. We will discuss the efficacy of our approach and show that the critical point of the model in Eq. (1.6) is better suited for conformal cooling. By quenching close to the critical point, we look for the emergence of criticality. We propose a simple scheme to optimize the cooling procedure and discover an effect that we call *overcooling*, wherein the amount of energy removed on a short time-scale highly exceeds the equilibrium expectation. Finally we focus on scaling our approach—in App. D we probe the thermodynamic limit for the exactly solvable transverse-field Ising model at its critical point which shares a common low-energy description with Eq. (1.6).

Our procedure works as follows: We initialize the system in the uniform product state $|\psi(0)\rangle = \otimes_{i=1}^{N} |\vartheta, \phi_i\rangle$ which can be done efficiently[4]. Afterwards, we perform a quench by drastically changing the Hamiltonian and evolve the system using the spatially modulated Hamiltonian

$$\mathcal{H} = \sum_{i=1}^{N-1} \lambda_i J \, \hat{n}_i \otimes \hat{n}_{i+1} + \sum_{i=1}^{N} \lambda_i \left(\frac{\Omega}{2} \, \hat{\sigma}_i^x - \Delta \, \hat{n}_i \right), \tag{1.8}$$

where $\lambda_i > 0$ is the spatial modulation and we denote $J \equiv C/a^6$ as the scale for the interaction energy. A natural figure of merit for conformal cooling is how much energy is removed from the system over the course of the quench. It is useful to define a local Hamiltonian on each site for this

purpose. We follow the convention of Goto et al. and introduce

$$\hat{h}_i = \mathcal{H}\Big|_i = \lambda_i \left(\frac{\Omega}{2} \hat{\sigma}_i^x - \Delta \hat{n}_i \right) + \frac{1}{2} \left(\lambda_i J \, \hat{n}_i \otimes \hat{n}_{i+1} + \lambda_{i-1} J \, \hat{n}_{i-1} \otimes \hat{n}_i \right) \tag{1.9}$$

as the local energy density operator. In open boundary conditions, which we assume for the remainder of this chapter, we set $\hat{n}_0 = \hat{n}_{N+1} = 0$. We observe that $\sum_{i=1}^{N} \hat{h}_i = \mathcal{H}$ as we expect. The energy in the system is then

$$E_S(t) = \sum_{i \in S} \langle \psi(t) | \hat{h}_i | \psi(t) \rangle,$$

where $|\psi(t)\rangle = \exp(-\mathrm{i}\mathcal{H}t)|\psi(0)\rangle$ with the initial state $|\psi(0)\rangle$ and i is the imaginary unit. Using Eq. (1.3) we can convert the energy density into local temperature profiles given the energy-temperature relation. Strictly speaking defining a microscopic temperature on a lattice is a subtle task. Here, we simply match the energy density of the time-evolved state with a Gibbs state of the same energy density. This is physically motivated by the ETH which predicts that these values should match in equilibrium.

Lastly we give a short discussion of the initial state $|\psi(0)\rangle$, which we take to be a uniform and therefore uncorrelated product state. We know that it takes the form $\otimes_{i=1}^{N} |\vartheta, \phi_i\rangle$, where

$$|\vartheta, \phi\rangle = \cos\left(\frac{\vartheta}{2}\right) |\mathrm{r}\rangle + e^{i\phi} \sin\left(\frac{\vartheta}{2}\right) |\mathrm{g}\rangle$$

is an arbitrary state on the surface of the Bloch sphere, where ϑ is the polar angle and ϕ the azimuthal angle. Ideally, we would like to initialize the lowest-energy uniform product state which also has the lowest initial temperature, allowing for better cooling. We can easily compute the energy of $|\psi(0)\rangle$

with regard to the Hamiltonian in Eq. (1.8) parametrized by ϑ and ϕ:

$$E(\vartheta,\phi) = \langle \vartheta,\phi|\mathcal{H}|\vartheta,\phi\rangle = \sum_{i=1}^{N-1} \lambda_i J \left[\frac{1+\cos(\vartheta)}{2}\right]^2 + \sum_{i=1}^{N} \lambda_i \left[\frac{\Omega}{2}\sin(\vartheta)\cos(\phi) - \Delta\frac{1+\cos(\vartheta)}{2}\right].$$

We used the representation of $|\vartheta,\phi\rangle$ on the Bloch sphere

$$\begin{aligned}\langle \vartheta,\phi|\hat{\sigma}^x|\vartheta,\phi\rangle &= \sin(\vartheta)\cos(\phi)\\ \langle \vartheta,\phi|\hat{\sigma}^y|\vartheta,\phi\rangle &= \sin(\vartheta)\sin(\phi)\\ \langle \vartheta,\phi|\hat{\sigma}^z|\vartheta,\phi\rangle &= \cos(\vartheta).\end{aligned}$$

For $\Omega > 0$ it becomes clear that the $E(\vartheta,\phi)$ is minimized for $\phi = \pi$. In the blockade limit we assume $J \gg \Delta, \Omega$[4] and find that $\vartheta = \pi$ minimizes the initial energy. This means that all atoms are initialized in their electronic ground state which can be efficiently prepared using optical pumping[4], i.e., we use $|\psi(0)\rangle = \otimes_{i=1}^{N}|g_i\rangle$ with $\langle\psi(0)|\mathcal{H}|\psi(0)\rangle = 0$.

Another consideration is the shape of the spatial modulation considered here. Following the proposal by Zaletel et al. we choose a flat profile for the system ($\lambda_i = 1$) and the bath ($\lambda_i = \lambda_{\text{bath}}$). To avoid mismatching of heat conductivities at the boundary between the two regions, it is generally preferable to have a smooth deformation. Therefore we introduce an intermediate region, the *ramp*, and interpolate linearly between the other two regions. This leaves a number of parameters that we optimize for improved cooling: the size of the bath N_{B}, the size of the ramp N_{R}, and the rescaling constant in the bath $\lambda_{\text{bath}} = \min_i(\lambda_i)$. Of course there are a plethora of alternative spatial modulations to consider including parabolic[36] and sinusoidal[19] shapes—we note that our results do not rely on the specific choice of spatial modulation.

As for the Hamiltonian parameters, we choose $\Omega = 0.5$ and $R_{\text{b}} = 1.5$ for all simulations in this section, i.e.,$J = \Omega R_{\text{b}}^6 \approx 5.7$. Any energy will be expressed in units of Ω. Fig. (1.3) shows

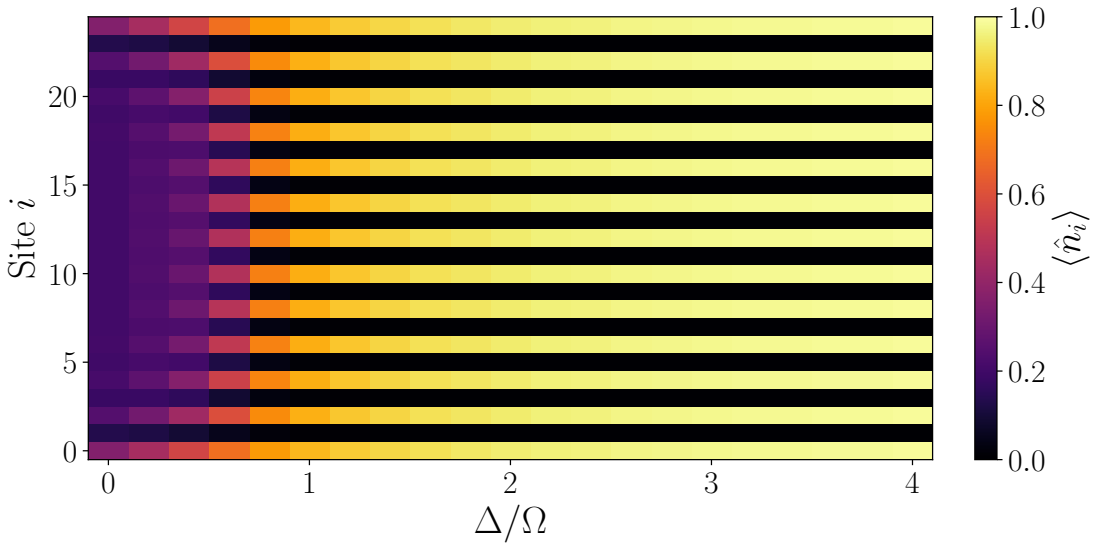

Figure 1.3: Spontaneous breaking of the translational $\mathbb{Z}_2$ symmetry in a one-dimensional Rydberg atom tweezer array of length $L = 25$. The plot shows the population on each site, $\langle \hat{n}_i \rangle$, for different Δ/Ω. As the ratio Δ/Ω is tuned to large positive values, the ground state undergoes a phase transition: at $\Delta/\Omega = 0$ there are no Rydberg excitations; at $\Delta/\Omega = 4$ every second site is in the excited Rydberg state. For numerical details we refer to the main text. $\Omega = 0.5, R_b = 1.5$.

the ground state phase transition from the paramagnetic to the $\mathbb{Z}_2$ ordered phase and the associated translational symmetry-breaking in a Rydberg array of size $L = 25$. At $\Delta/\Omega = 4$ (orange square in Fig. 1.2), we observe clear $\mathbb{Z}_2$ order so we choose this parameter for investigations in the ordered phase. The critical point is roughly given by $\Delta/\Omega = 1$ (blue pentagon in Fig. 1.2), consistent with the literature [30], and will be subject to further study in later sections.

Since we are employing matrix product state methods to study the many-body dynamics, we note the following numerical parameters which are explained in more detail in App. A. We choose the maximum bond dimension of the matrix product state $\chi_{\max} = 512$ and the minimal Schmidt value $\lambda_{\min} = 10^{-10}$. The time step is taken to be $\delta t = 0.05\ \Omega^{-1}$. Fig. 1.3 shows results obtained via the density-matrix renormalization group with maximum bond dimension $\chi_{\max} = 512$. We assert that the following results are converged in these parameters.

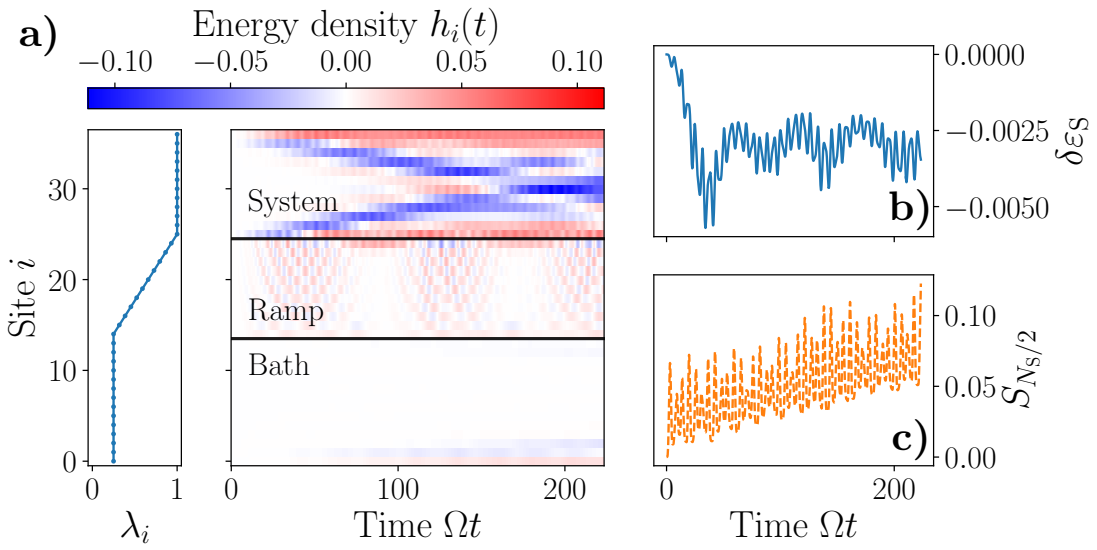

Figure 1.4: Conformal cooling quench in the $\mathbb{Z}_2$ phase. **a)** On the left we plot the spatial modulation; on the right is the change in energy density for every site i as a function of time Ωt. We see that energy is accumulating at the edges of the system (black edges), but not effectively leaking into the ramp as we would expect from diffusive dynamics. **b)** The average energy change in the system $\delta\varepsilon_S = (N_S)^{-1}\sum_{i\in S} h_i(t)$ shows a slight decrease for short times before saturating—fast oscillations can be observed throughout the evolution. **c)** The half-chain entanglement entropy $S_{N_S/2}$ of the system as a function of time (see text for details). We see large, fast oscillations consistent with a) and a slow linear increase in $S_{N_S/2}$. This behavior is indicative of quantum many-body scars which were first observed in the Rydberg blockade model by Bernien et al.. $N_S = 12, N_R = 11, N_B = 14, \lambda_{\text{bath}} = 0.25$.

1.2.1 $\mathbb{Z}_2$ Phase

We begin by investigating conformal cooling quenches in the $\mathbb{Z}_2$ phase of the 1D Rydberg blockade model. The goal is to find energy transfer from the system into the bath and ultimately to observe the subsequent build-up of $\mathbb{Z}_2$ correlations. Since we are dealing with a quantum phase transition, we need to reach very low temperatures to observe this, ideally cooling below the gap of the Hamiltonian. Therefore, we will first investigate the general efficacy of conformal cooling using a spatial modulation similar to the one employed by Zaletel et al. before optimizing the parameters of the spatial modulation and then increasing the respective subsystem sizes to study the scalability of this approach.

In Fig. 1.4 we plot different metrics of diagnosing the dynamics of conformal cooling. First, Fig. 1.4a) shows the spatial modulation λ_i on the left. The right panel of Fig. 1.4a) depicts the change in energy density

$$h_i(t) = \langle \hat{h}_i(t) - \hat{h}_i(0) \rangle \tag{1.10}$$

in time. We note that $\langle \hat{h}_i(0) \rangle = 0 \ \forall \ i$, i.e., any change in the energy coincidences with the energy. At early times, the dynamics in the energy density are dominated by the edges of the system: the atom at each edge absorbs energy which is compensated by the center of the system. The ramp also shows an increase in energy—however, only on a short time scale, as this energy becomes localized in the ramp, bouncing between its two boundaries which are shown as black edges in Fig. 1.4a). This is surprising as the model is nonintegrable for this particular choice of Hamiltonian parameters, meaning it is generally expected to exhibit diffusive energy transport at high temperatures[41]—in fact the spin-$\frac{1}{2}$ mapping of this Hamiltonian shows this property[32].

At the same time, there is also no meaningful energy exchange with the bath. One factor is the increased time scale of dynamics due to the rescaled magnitude of the bath: if we decouple the bath, its dynamics will happen slower than in the decoupled system, exactly by a factor of $\lambda_{\text{bath}}^{-1} = 4$. We need to take this into account as this will impact the time scales for local thermalization of the bath and hence the time scale for global thermalization. A similar phenomenon was observed by Zaletel et al..

In Fig. 1.4b) we investigate the change in the energy of the system which we introduced as the figure of merit for conformal cooling. We denote the average energy density in the system as $\varepsilon_S = E_S/N_S$ with $\delta\varepsilon_S$ being the relative change in this quantity. While it decreases at early times, it saturates quickly, therefore confirming the lack of energy diffusion into the ramp. The amount of cooling is also significantly less than thermodynamic expectations from Eq. (1.4). Initially the sys-

tem has an approximate temperature of $T_\mathrm{i} = 20.2$ in units of Ω. This is obtained from Eq. (1.3) via exact diagonalization on a chain of length $L = 12$ with open boundary conditions where we asserted the convergence in the chain length. In combination with the spatial modulation in Fig. 1.4a) we would expect a final temperature $T_\mathrm{f} = 15.2$ from Eq. (1.4) corresponding to $\varepsilon_\mathrm{S} = -0.2$. This is more than an order of magnitude greater than the observed cooling.

Fig. 1.4 provides an explanation for this observation. The half-chain entanglement entropy of the system

$$S = -\mathrm{Tr}\left(\rho_\mathrm{hc}\log(\rho_\mathrm{hc})\right),$$

where ρ_hc is the reduced state of one half of the system, exhibits an oscillatory behavior with a very slow, linear increase up to time scales of $\Omega t = 200$. This is a stark contrast to ergodic behavior, where we expect to see a sharp linear increase until saturation at a volume-law state, for which the entanglement entropy scales linearly in the system size[32]. Our dynamics on the other hand are in line with observations for quantum many-body scars which have been discovered in the Rydberg blockade model[4]. These are states which retain high support within a small subspace of the overall Hilbert space as the state is evolved for long times[27]. This leads to ergodicity breaking and hence nonthermal dynamics. Quantum many-body scar states have been a topic of high interest recently in the field of quantum thermalization[50,27,65,76,31]. The recent discovery that the initial state considered here, $|\psi(0)\rangle = \bigotimes_i |\mathrm{g}\rangle$, is in fact a scar state in the $\mathbb{Z}_2$ phase, is important to our analysis[12,53,41]. An intuitive argument for the ergodicity breaking is the lack of resonant transitions of $|\psi(0)\rangle$ via state flips $|\mathrm{g}\rangle \rightarrow |\mathrm{e}\rangle$, which are facilitated by the Rabi drive, therefore effectively limiting the state space that the initial state explores at short to intermediate times. In fact, for $\Delta \gg \Omega$ the Hilbert space factors into dynamically disconnected subsectors with the same number of Rydberg atoms in the chain[33]. Due to this nonthermal behavior, the thermodynamic arguments break down as the

state is not expected to thermalize on an accessible time scale which fits into our observations in Fig. 1.4.

This might suggest that one should just start with a different initial state at higher energy, therefore circumventing the issues of many-body scarring. It turns out that the many-body scars also have a significant impact on the infinite-temperature energy transport as found by Ljubotina et al., resulting in superdiffusive instead of the expected diffusive energy transport. In combination with the factorization of the Hilbert space into dynamically disconnected subsectors, this suggests that generic states do not exhibit ergodic dynamics until long time scales. As Zaletel et al. emphasize, rapid local thermalization is an essential ingredient for conformal cooling based on macroscopic gradients in the energy density. Failure to satisfy this condition breaks the thermodynamics arguments leading to unexpected behavior. Intriguingly recent investigations [12,53,88] discovered connections between the observed quantum many-body scar states and the critical point of Eq. (1.6). They find that quenching scar states with the (near-)critical Hamiltonian leads to the restoration of thermalizing behavior. In particular this includes the initial state we consider, leading us to probe conformal cooling near the critical point.

1.2.2 Near criticality

Criticality plays a central role in the field of statistical physics where it describes the transition between two phases of matter, e.g., from a paramagnetic to an antiferromagnetic phase as we consider. This critical behavior is generally characterized by universality classes, that seek to uniquely identify certain scaling relations as a system approaches criticality at low energies. This is achieved via the renormalization group [85] and predicts for example how the correlation length ξ scales with respect to

a control parameter τ

$$\xi \propto |\tau|^{-\nu}. \tag{1.11}$$

τ is used to tune between the different phases; examples include the normalized temperature $(T - T_c)/T_c$ or in our case the normalized chemical potential $(\Delta - \Delta_c)/\Delta_c$ where T_c and Δ_c are the corresponding critical values. ν is a *critical exponent* and plays an important role as the correlation length can be accessed via correlation functions of the form

$$\langle \hat{\mathcal{O}}_i \hat{\mathcal{O}}_j \rangle - \langle \hat{\mathcal{O}}_i \rangle \langle \hat{\mathcal{O}}_j \rangle \propto \exp(-\frac{|i-j|}{\xi})$$

for some local operator $\hat{\mathcal{O}}_k$ acting only on site k. Critical exponents correspond to the scaling of different properties, e.g., the order parameter or specific heat, and can often be related to one another. Together a set of critical exponents identifies a given universality class—for instance, $\nu = 1$ in the 2D Ising universality class*. The study of universality classes is an important aspect of statistical physics because it can uncover fundamental connections between different physical models. A similar treatment also extends to the dynamics of the model amplifying the significance of critical exponents beyond low-energy physics [23]. While Rydberg atom tweezer arrays have previously been used to perform analog quantum simulation of dynamical critical phenomena in one- and two-dimensional systems [30,14], preparing (near-)critical ground states still remains an elusive challenge due to the vanishing energy gap. Here, we explore conformal cooling quenches near the critical point of the Rydberg blockade model as a possible candidate to study critical phenomena at low temperatures. For this purpose we choose $\Delta/\Omega = 1$ which is close to the phase transition in Fig.1.3. We note that similar ideas were suggested in the context of spatially inhomogeneous quenches of conformal field theories [20].

*We note that $\nu = 1$ is not unique to this universality class.

We repeat the same strategy as in Sec. 1.2.1: we evolve the state $|\psi(0)\rangle = \bigotimes_i |g\rangle$ under the Hamiltonian in Eq. (1.8) tuned near criticality for the same spatial deformation as in Fig. 1.4. We observe the breakdown of quantum many-body scarring as the half-chain entanglement entropy saturates in Fig. 1.5c); therefore we would expect thermodynamic arguments to hold. The energy density dynamics in Fig. 1.5a) show clear energy transport across the system-ramp boundary. Energy is transferred from the system into the ramp, therefore cooling the system and heating the ramp. Interestingly, the lost energy spreads throughout the system seemingly ballistically without dispersion as indicated by a blue wave packet arising at $\Omega t = 50$. An interesting feature is the dispersion of energy in the ramp starting from the system-ramp boundary at $\Omega t \approx 100$ which may indicate diffusive behavior at long times (gray dashed line in Fig. 1.5a)).

Fig. 1.5b) underlines the observation that energy is leaving the system and with $\delta\varepsilon_S$ saturating at -0.02 which is roughly a fourfold increase over the cooling in the $\mathbb{Z}_2$ phase. However from Eq. (1.4) we would expect to reach $\varepsilon_S = -0.24$ and a temperature decrease from $T_i = 5.9$ to $T_f = 3.7$ which is much less than the observed minimum temperature of 5.6. This further emphasizes the need for optimizing the amount of cooling, especially given that the ground state has energy density $\varepsilon_S = -0.61$.

Despite the energy transport into the ramp, the bath is not absorbing energy effectively at the time scales that are accessible. Recall that energy transport is only possible through resonant processes, e.g., an atom only absorbs resonant light. In a many-body case there are an abundance of possible transitions. Here a useful figure of merit for energy transport is the energy variance of the subsystem since it reflects the width of its energy distribution. A system with a large energy variance will be spread out over many energy eigenstates allowing for more possible transitions than a system with small energy variance. Here we consider the energy variance which is given by

$$\Delta(\mathcal{H}_{\text{bath}}) = \sqrt{\langle \mathcal{H}_{\text{bath}}^2 \rangle - \langle \mathcal{H}_{\text{bath}} \rangle^2},$$

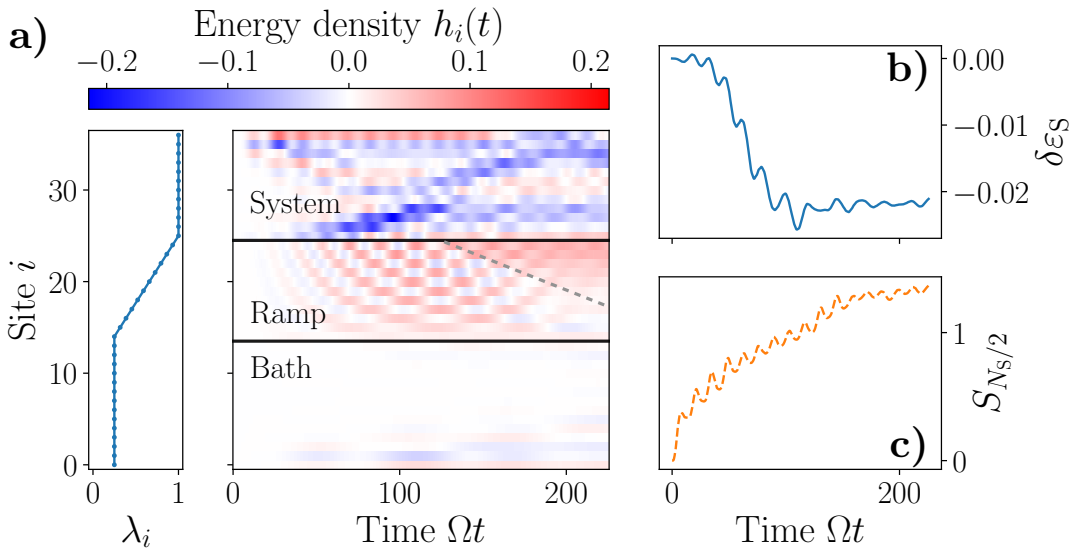

Figure 1.5: Conformal cooling quench near the critical point. **a)** The left panel depicts the Hamiltonian deformation with the spatially resolved dynamics of the change in energy density to the right. At early times the system emits energy into the ramp which is dispersed throughout; a lack of diffusion into the bath persists however. While early-time behavior exhibits coherent oscillations in the dynamics, there is seemingly an onset of diffusion at late times $\Omega t \approx 100$ (gray dashed line). **b)** The system shows a clear decrease in its average energy up to $\Omega t = 100$ before saturating at $\delta\varepsilon_S \approx -0.02$—a substantial improvement over quenches in the $\mathbb{Z}_2$ phase (cf. Fig. 1.4). **c)** The half-chain entanglement entropy indicates thermalizing behavior with a sharp linear increase in time. $N_S = 12, N_R = 11, N_B = 14, \lambda_{\text{bath}} = 0.25$.

where $\mathcal{H}_{\text{bath}} = \sum_{i\in B} \hat{h}_i$. Trivially, we would expect it to be reduced by λ_{bath} in comparison to the system at an equal length. This means that the bath cannot effectively absorb energy from the system for small λ_{bath}.

Another perspective to consider are strong zero modes which are conserved operators localized at the edge of a system. Recently, work on coupled transverse-field Ising chains differing only in magnitude found these long-lived states localized at the boundary between the two chains[51]. Olund et al. attribute this to a lack of resonant processes at this boundary due to the different magnitudes of the Hamiltonians. This localized mode may hinder energy transport across the boundary and therefore lead to very long time scales for cooling. We conclude that a flat bath is therefore unlikely to contribute to the cooling.

Now that we have an understanding that energy transport between the system and ramp is possible close to the critical point, our next step is to improve the amount of cooling. For this purpose, we optimize over the parameters of the spatial deformation for a given system. Here we consider a system of size $N_S = 8$ coupled to bath-ramp structures at each end. This contrasts the end-to-end configuration that we employed so far. One advantage of coupling to a bath at each end is that cooling will generally happen at half the time scale. Following the Heisenberg equation of motion, the rate of change of the system's energy is given by

$$\partial_t \mathcal{H}_S \propto [\mathcal{H}, \mathcal{H}_S] = \left([\hat{h}_{i_L-1}, \hat{h}_{i_L}] + [\hat{h}_{i_R}, \hat{h}_{i_R-1}] \right)$$

where i_L and i_R mark the left and right ends of the system and $\mathcal{H}_S = \sum_{i \in S} \hat{h}_i$. For an end-to-end configuration only one of the two terms would appear. As we seek to outperform current state preparation approaches, the time scale for preparing the final state is naturally a consideration which is why we choose to work with this setup.

Besides the system size, we also fix the size of the combined ramp-bath structure on each side to $(N_R + N_B)/2 = 8$ with a total length of $N_S + N_R + N_B = 24$. We adjust the length of the ramp N_R, and the lowest rescaling factor, λ_{bath}, in Fig. 1.6. As a figure of merit we again consider the change of the energy in the system. To obtain the maximal amount of cooling, we simply take the minimal value of ε_S after we let the system evolve up to $\Omega t \approx 250$. At these times we observe that the system reaches a minimum or stationary value.

In Fig. 1.6 we find that the cooling is optimal for long and shallow ramps. First of all, these results confirm our previous discussion that flat baths do not effectively cool the system due to poor energy transport properties and the emergence of a long-lived mode at the bath-ramp boundary that hinders transport. Fig. 1.6 shows the optimal cooling for $N_R = 16$ and $\lambda_{\text{bath}} = 0.75$ with the minimal energy density $\varepsilon_S = -0.17$, a substantial improvement over the previous case and significantly

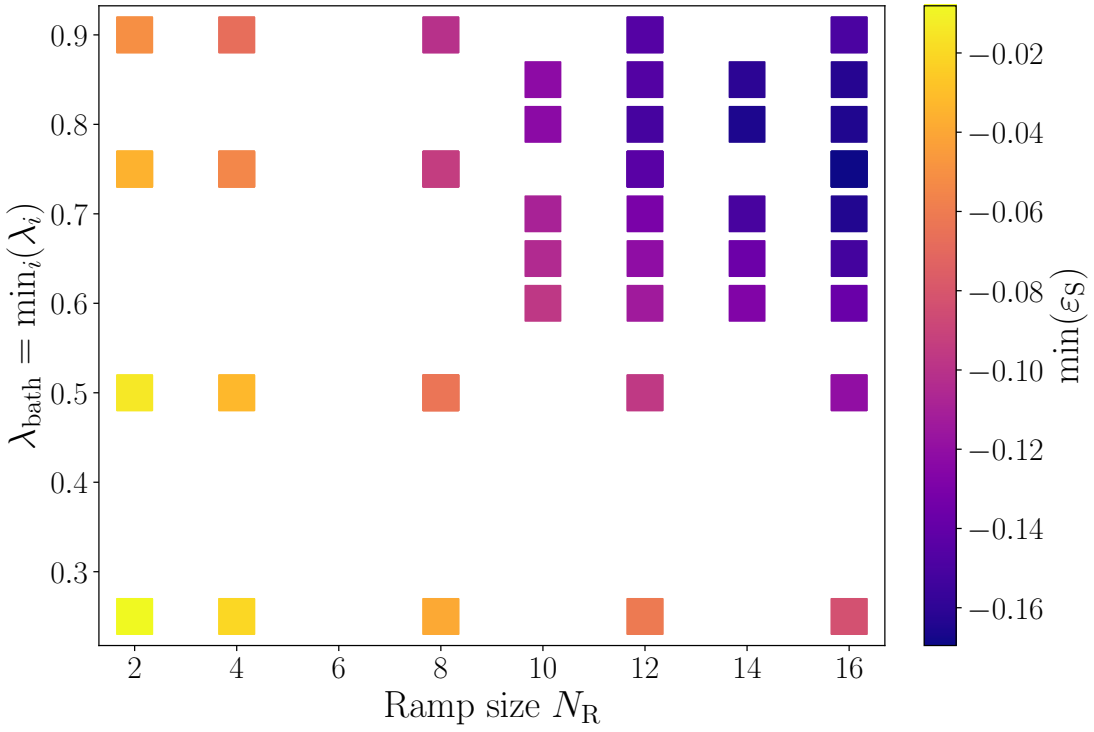

Figure 1.6: Optimization of cooling near the critical point via tuning of the spatial deformation parameters N_{R} and λ_{bath}. The minimum energy density in the system, ε_{S}, shows a clear tendency towards optimal cooling for long, shallow ramps. By focusing on this parameter region we identify $N_{\text{R}} = 16$ and $\lambda_{\text{bath}} = 0.75$ as the optimal parameters with $\min(\varepsilon_{\text{S}}) \approx -0.17$ which is an order of magnitude improvement over Fig. 1.5b). $N_{\text{S}} = 8$.

closer to the ground state at $\varepsilon_{\text{S}} = -0.61$.

Fig. 1.7 shows the dynamics for the optimal parameters identified in Fig. 1.6. We observe rapid energy transport out of the system into the ramp up to $\Omega t = 180$ (cf. Fig. 1.7a)). The system emits energy into the ramp which is ultimately accumulating at the outer edges of the ramp. This is expected from heat diffusion, however, the dynamics at later times strongly deviate from diffusive behavior as the system reabsorbs most of the energy lost. This indicates transient energy transport that differs from the expected diffusive behavior. As previously mentioned, the superdiffusive energy transport in the closely related *PXP* model on the time scales, that we investigate[41], may be responsible for our observations. While Ljubotina et al. study infinite temperature transport, we

consider a specific initial state at finite energy which can also exhibit different dynamics behavior constrained by approximate conservation laws or dynamic constraints. This may also suggest a close connection to integrability.

The change in the average energy density of the system shows an interesting time dependence in Fig. 1.7b): from numerical inspection we find $\delta\varepsilon_S \propto -t^2$ up to $\Omega t = 180$, i.e., while the system is releasing energy into the ramp. In fact this t^2-scaling occurs rather generically for shallow ramps in Fig. 1.6 suggesting a more general behavior. Perturbation theory suggests this scaling for short times—it is surprising that it persists up to such late times. During our discussion in Ch. 3 we will propose a potential toy model to explain this behavior.

Intriguingly, among the many differences between this case and the previously discussed scenarios, there is one particularly interesting feature: the cooling outperforms the equilibrium expectation (cf. Eq 1.4) as we see in Fig. 1.7b). The minimum energy density corresponds to a temperature of $T_{\text{min}} = 4.3$, which is better than the expected cooling to $T_f = 5.3$. One striking feature of Fig. 1.7a) is the cooling of the system's two central sites to a temperature of $T = 2.4$. We find this *overcooling* to be a phenomenon worthy of deeper investigation because it has several interesting implications: First, it shows that we can surpass thermodynamic expectations on intermediate time scales. This suggests a cooling protocol where the system is decoupled at the time when the minimum in ε_S is reached; here this would be $\Omega t \approx 180$. Afterwards the system would evolve on its own to eventually equilibrate. This time scale may be attainable on near-term experiments: assuming a Rabi frequency of $\Omega = 2\pi \times 5.5\,\text{MHz}$, we find that cooling requires evolution up to $t = 180\Omega^{-1} \approx 5.2\,\mu\text{s}$ which is reasonable for current experimental capabilities [15,66]. The second advantage of overcooling is its time scale which is inherently fast than thermalization. Conformal cooling requires that the system thermalizes on a global scale, a process that can take exponentially long in the system size [40,9]. For instance, the given model shows thermalization on time scales beyond the reach of our numerical investigation for the system sizes considered here. Therefore this

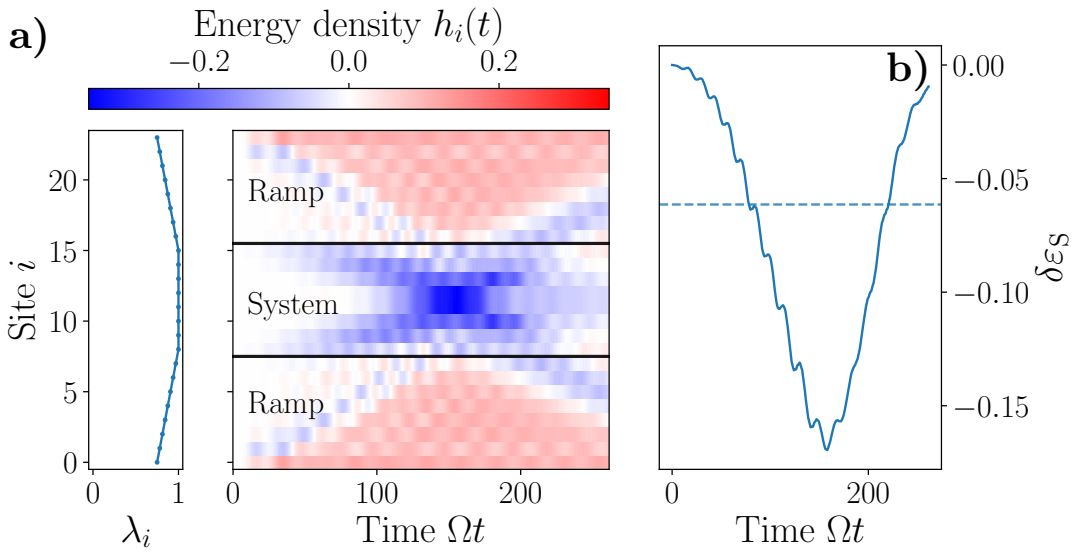

Figure 1.7: Dynamics of the optimal conformal cooling quench from Fig. 1.6. **a)** The spatial modulation on the left corresponds to a long and shallow ramp. Energy transport is evident in the energy density dynamics on the right. Cooling spreads from the edges of the system into its bulk while the outer edges of the ramp accumulate energy. This behavior shares similarities with heat diffusion with a spatially dependent heat conductivity as shown on the left. **b)** The system's energy density decreases sharply up to $\Omega t = 180$ before rebounding back to its initial value. The minimum corresponds to the reported value of $\min(\varepsilon_S) = -0.17$. The dashed line shows the thermodynamic expectation derived from Eq. (1.4); the observed cooling is more than a factor 2 greater than this value. $N_S = 8, N_R = 16, N_B = 0, \lambda_{\text{bath}} = 0.75$.

transient overcooling effect may lead to faster state preparation. Ultimately this effect needs a more detailed understanding, especially in terms of scalability which we will investigate in the following section.

1.2.3 Scaling of overcooling

One interesting prospect of overcooling is how the amount of cooling depends on the system parameters, i.e., how does it impact the cooling in the thermodynamic limit. For this purpose, we again turn to the end-to-end configuration of the spatial modulation, which makes reaching large system and ramp sizes more viable. We work with long and shallow ramps which generically exhibited the overcooling and increase the system and the ramp size, while keeping the slope the ramp

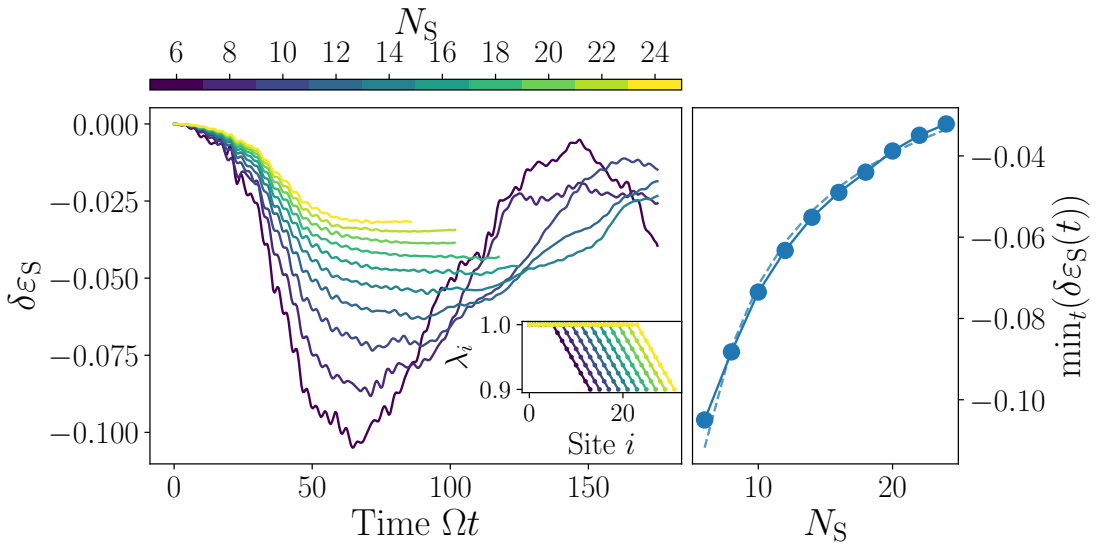

Figure 1.8: Scaling of overcooling with the system size N_S with a fixed ramp. **a)** Over a range of system sizes the average energy density of the system ε_S shows a minimum occurring around $\Omega t \approx 75$. As N_S is increased a plateau arises before the system ultimately absorbs energy again. The inset shows the corresponding spatial modulations, where $\lambda_i = 1$ for $i = 0, \ldots, N_S - 1$. **b)** The minimum of ε_S in time shows a monotonic increase proportional to $N_S^{-0.9}$, where the scaling was extracted from a fit (dashed line). Effectively the ramp can only absorb a finite amount of energy from the system—further increasing the system will therefore not result in improved cooling. $N_R = 8, \alpha = 0.125$.

fixed. There is of course one caveat with this approach: the linear ramp cannot be extrapolated to the thermodynamic limit ($N_R \to \infty$) while keeping the constraint $0 < \lambda_i < 1$; instead it will eventually reach negative values and diverge, a feature that cannot be obtained in our experimental proposal. However, we can still see the scaling without this limitation for sufficiently shallow ramps. We expect the scaling to be generic for long, shallow ramps, depending only weakly on the slope of the ramp. Our approach takes one case that exhibits overcooling and introduces new subsystems to investigate how conformal cooling performs. We choose either $N_S = 8$ and scale N_R, or $N_R = 8$ and scale N_S instead, with a slope of $\alpha = (1 - \min_i(\lambda_i))/N_R = 0.125$.

In Fig. 1.8a) we show the dynamics of ε_S as we gradually increase the system size from $N_S = 6$ to $N_S = 24$. Smaller systems show a larger decrease in the average energy density, which is expected because $\varepsilon_S \propto N_S^{-1}$. In fact, the early-time emission of energy should be identical across all system

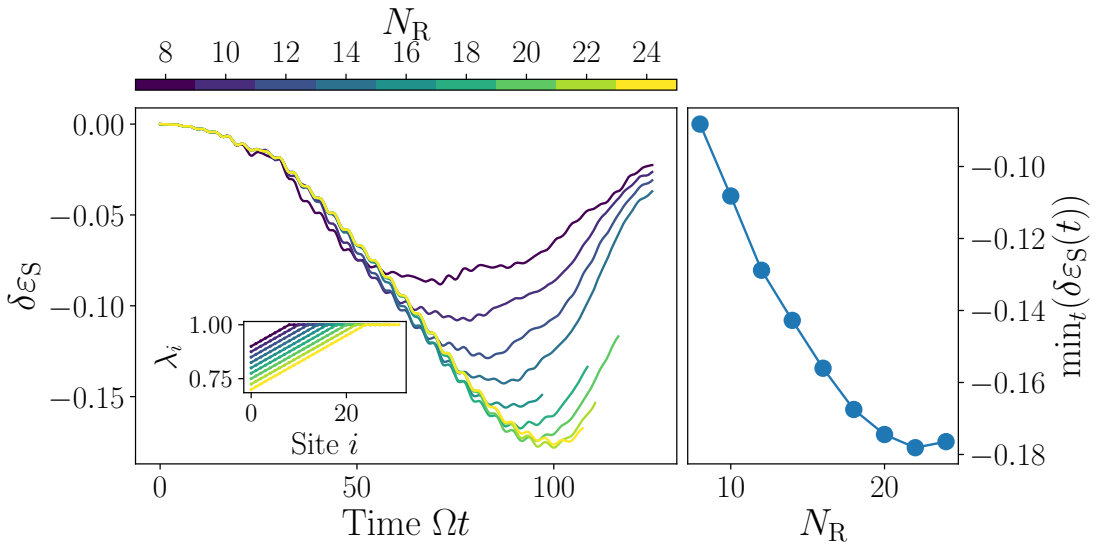

Figure 1.9: Scaling of overcooling with the ramp size N_R at a fixed system size $N_S = 8$ and ramp slope $\alpha = 0.125$. **a)** The average energy density in the system shows lower minima as the ramp size is increased; the inset shows the spatial modulation where $\lambda_i = 1$ for $i = N_R, \ldots, N_R + N_S - 1$. We observe saturation in the minimum beyond $N_R = 2.5N_S$. **b)** The maximum amount of cooling, $\min_t(\varepsilon_S(t))$, indeed saturates for large ramps, suggesting that overcooling can only remove a certain amount of energy.

sizes, as the Lieb-Robinson bounds suggest that it takes a finite time for energy from the additional system to reach the system-ramp boundary. This is indeed observed as the dynamics deviate at times $\Omega t > 50$. While the system reabsorbs nearly the entire energy emitted shortly after reaching its minimal value similarly to what was observed in Figs. 1.4 and 1.7, this is not the case for larger system where it instead saturates for a time that increases with system size—at sufficiently large times we would expect to see the reabsorption for any system size. The plateau value roughly corresponds to the minimum of ε_S in Fig. 1.8b). It shows a monotonic increase indicating that cooling vanishes in the thermodynamic limit as one would generically expect. One way of understanding these results is that the ramp only has a finite amount of energy it can absorb which will be saturated for some system size.

This also demonstrates that the overcooling can be attributed in large part to long-lived quasipar-

ticles localized at the system-ramp boundary that travel ballistically through the system. For larger system sizes they spend a longer time in the system before leaving into the ramp. This agrees with our observation that ε_S remains constant for a time that increases with the system size.

Fig. 1.9 shows the scaling of ε_S with the ramp size. While early-time dynamics are again similar, we see that cooling improves for larger ramp sizes in Fig. 1.9a). For increasingly large N_R, the minimum of ε_S saturates however, suggesting that cooling cannot be improved by further increasing the ramp size. Fig. 1.9b) corroborates this result as maximum cooling shows no improvement beyond $N_R \approx 2.5 N_S$. This result is in contrast with the thermodynamic prediction that cooling should always improve as more resources for cooling, e.g., a larger ramp, are introduced.

These results suggest that overcooling is a finite size effect originating at the boundary between the system and the ramp or open boundary conditions as observed in Fig. 1.7a). However, these effects will only lead to a constant improvement over the thermodynamic expectation at small system sizes. Therefore it would be necessary to simultaneously increase the system and ramp size to see overcooling vanish. This is beyond the scope of the current investigation given the requirement to reach both large chain sizes and long run times to observe this prediction.

2

Adiabatic Preparation of the thermofield-double State

Studying phases of matter generally requires preparing the ground state of a given model. However, as previously discussed it is often sufficient to reach adequately low-entropy and low-temperature states to observe the relevant phenomena. This opens an alternative

avenue to cooling analogue quantum simulators: adiabatic preparation of low-temperature thermal states. We will first discuss the motivation and background behind this approach, focusing on the feasibility in different models. Afterwards, our investigation focuses on the spin-$\frac{1}{2}$ critical antiferromagnetic Heisenberg model. We use CFT arguments for the comparison of correlation functions of thermal states and the ground states of coupled chains.

2.1 Background

Rydberg tweezer arrays can be used to study finite-temperature phase transitions as recently demonstrated by Chen et al., as these platforms move towards 2D and 3D geometries, where finite-temperature order arises more generally[49]. Formally, this requires studying states of the form

$$\rho_\beta = \frac{\exp\left(-\beta\mathcal{H}\right)}{\mathcal{Z}}, \tag{2.1}$$

where $\beta = 1/T$ is the inverse temperature, $\mathcal{H}$ is the system's Hamiltonian, and $\mathcal{Z} = \mathrm{Tr}\left[\exp\left(-\beta\mathcal{H}\right)\right]$ is the partition function. These *Gibbs* states are mixed states with a purity

$$\mathrm{Tr}\left(\rho_\beta^2\right) < 1.$$

for any finite β. It turns out that ρ_β is the state with the maximal entropy at a given energy. The second law of thermodynamics predicts that systems tend towards it as they evolve in time. As per ETH (cf. App. B) we generally expect subsystems of closed quantum systems to thermalize in non-integrable models.

The preparation of Gibbs states is still an open question. One way of studying finite-temperature phenomena is to quench a state at some finite energy and waiting for it to thermalize. While this does not prepare an exact Gibbs state, expectation values of local observables approach the canonical

ones. This section explores the prospect of adiabatic approaches. There is one fundamental problem with this idea however: ρ_β is a mixed state, i.e., not an eigenstate of H, so the adiabatic theorem does not apply. Instead we consider a purification of ρ_β on two identical subsystems L and R. This is known as the *thermofield-double* (TFD) state

$$|\mathrm{TFD}\rangle = \frac{1}{\sqrt{\mathcal{Z}}} \sum_n \mathrm{e}^{-\frac{\beta E_n}{2}} |E_{n,\mathrm{L}}\rangle \otimes |E^*_{n,\mathrm{R}}\rangle. \tag{2.2}$$

$\{E_n, |E_n\rangle\}_n$ is the set of energy eigenvalues and eigenstates of $\mathcal{H}$ defined on each subsystem and the index n iterates through the number of eigenvalues of the Hamiltonian—d^L for a chain of L d-level systems. We also define $|E^*_n\rangle = \Theta|E_n\rangle$, where Θ is an antiunitary operator such as time-reversal. Taking the partial trace over one of the two subsystems reveals that

$$\rho_{\beta,\mathrm{S}} = \mathrm{Tr}_{\bar{\mathrm{S}}} \left(|\mathrm{TFD}\rangle\langle\mathrm{TFD}| \right),$$

where $\mathrm{S} \in \{\mathrm{L}, \mathrm{R}\}$ and $\bar{\mathrm{S}}$ is the compliment of S. Of course the purification of ρ_β is not unique, in fact there are many states similar to the TFD, but with complex phases in each term of the sum resulting in the same reduced density matrix. In summary we can study thermal states given a TFD-like state by discarding one half of the system and only taking expectation values within the remaining half.

Interestingly the thermofield-double state is of particular importance in the context of quantum gravity. The AdS/CFT correspondence relates gravity in the bulk of a $d+1$-dimensional Anti-de Sitter (AdS) space to conformal field theories (CFTs) on its d-dimensional boundary. Effectively every phenomenon or measurement in one theory maps to an equivalent one in the other. It turns out that the dual of the TFD in the CFT is a two-sided black hole in the gravity theory[44]. One intuitive connection relates to black holes emitting thermal radiation such that they can be described

as being in a Gibbs state—a result famously derived by Stephen Hawking[25]. The hypothesis of this connection led to optimism that unresolved questions regarding black holes could be addressed by studying the TFD state of two boundary CFTs [10,28,72,45]. Subsequent explorations have found that a perturbative interaction between the two sides can lead to a traversable wormhole, i.e., information can be transferred from one side to the other similar to quantum teleportation [62,28,18].

These developments have spawned a rich literature around the protocols for preparing thermofield-double states on digital quantum computers [72,93,86] and identifying Hamiltonians whose ground states approximate the TFD [10,45]. Maldacena & Qi show that the Sachdev-Ye-Kitaev model [46] admits a TFD-like ground state using exact calculations. This work also opens a pathway to a more general investigation using conformal field theory—we will pursue this effort in our analysis. Intriguingly Cottrell et al. find a broad class of models that exhibit TFD-like ground states: those satisfying the eigenstate thermalization hypothesis [10]. The exact results of Cottrell et al. rely on specific nonlocal interactions between the two sides, making them unrealistic for near-term implementation on experimental platforms. Cottrell et al. claim however that local interactions suffice to evoke a ground state close to the TFD with a gap that is on the order of the temperature if the decoupled model obeys ETH. This thesis aims to test this hypothesis and present a new perspective using CFT arguments.

These results are encouraging considering that many models including the Rydberg atom array Hamiltonian fall within these categories. Ultimately our goal is to test these hypotheses and find an *experimentally relevant* Hamiltonian of the form

$$H = \mathcal{H}_{\mathrm{L}}^{0} + \mathcal{H}_{\mathrm{R}}^{0} - g\mathcal{H}_{\mathrm{LR}} \tag{2.3}$$

that has the TFD state as its ground state such that we can use adiabatic means of preparing it. Here $\mathcal{H}_{\mathrm{L,R}}^{0}$ is the Hamiltonian of each subsystem, g is the dimensionless coupling strength, and $\mathcal{H}_{\mathrm{LR}}$

is the coupling between the two subsystems. By experimentally relevant we require that $\mathcal{H}_{\mathrm{LR}}$ be spatially local in terms of operators of each chain, i.e.,

$$\mathcal{H}_{\mathrm{LR}} = \sum_{k=1}^{K} \hat{\mathcal{O}}_{k,\mathrm{L}} \otimes \hat{\mathcal{O}}^*_{k,\mathrm{R}}, \tag{2.4}$$

where $\hat{\mathcal{O}}_{k,\mathrm{S}}$ ($\mathrm{S} \in \{\mathrm{L},\mathrm{R}\}$) are Hermitian operators with support only on S and some finite range around site k and $\hat{\mathcal{O}}^*_k = \Theta \hat{\mathcal{O}}_k \Theta^{-1}$. The coupling comprises K operators on each side—in practice we choose K to be on the order of the chain size L. We choose this interaction such that its ground state is the thermofield-double state at infinite temperature

$$|I\rangle = \frac{1}{\sqrt{d^L}} \sum_n |E_{n,\mathrm{L}}\rangle \otimes |E^*_{n,\mathrm{R}}\rangle,$$

which is a highly entangled state between the two systems. Tracing out L or R leaves a reduced density matrix that is proportional to the identity on the other system. This means that the interaction leads to a competition in the ground state of H: while $\mathcal{H}^0_{\mathrm{L}} + \mathcal{H}^0_{\mathrm{R}}$ favors the individual and uncorrelated ground states $|E_{0,\mathrm{L}}\rangle \otimes |E^*_{0,\mathrm{R}}\rangle$, the coupling seeks to maximize correlations between the two sides.

By assuming the validity of the eigenstate thermalization hypothesis, Cottrell et al. showed that the ground state of Eq. (2.3) is close to the TFD. A key assumption of their analysis is that the ground state lies in the subspace of states $|n_{\mathrm{LR}}\rangle = |E_{n,\mathrm{L}}\rangle \otimes |E^*_{n,\mathrm{R}}\rangle$. We denote this as the *diagonal* subspace and its complement as the *offdiagonal* subspace. According to ETH the matrix elements of the operators $\hat{\mathcal{O}}_k$ are given by

$$O^k_{ij} \equiv \langle i|\hat{\mathcal{O}}_k|j\rangle = \delta_{ij}\mathcal{O}(E_i) + \frac{1}{\sqrt{\rho(\bar{E})}}\xi_{\mathcal{O}}(\bar{E},\omega)R^k_{ij}, \tag{2.5}$$

where δ_{ij} is the Kronecker delta, $\mathcal{O}(E_i)$ is a smooth function of the energy E_i corresponding to the

microcanonical expectation value, $\rho(E)$ is the density of states at energy E, R_{ij} are elements of a random matrix with mean zero and unit variance and $\xi_{\mathcal{O}}(\bar{E}, \omega)$ is a smooth function of the average energy $\bar{E} = (E_i + E_j)/2$ and the energy difference $\omega = E_i - E_j$. We assume R^k_{ij} to be Gaussian random variables which is a common assumption. Explicitly evaluating the matrix elements of the coupling Hamiltonian, we find

$$\begin{aligned}\langle E_{n,\mathrm{L}}, E^*_{m,\mathrm{R}}|\hat{H}_{\mathrm{LR}}|E_{a,\mathrm{L}}, E^*_{b,\mathrm{R}}\rangle &= \sum_{k=1}^{K}\langle E_{n,\mathrm{L}}|\hat{\mathcal{O}}_{k,\mathrm{L}}|E_{a,\mathrm{L}}\rangle\langle E^*_{m,\mathrm{R}}|\hat{\mathcal{O}}^*_{k,\mathrm{R}}|E^*_{b,\mathrm{R}}\rangle \\ &= \sum_{k=1}^{K}\langle E_n|\hat{\mathcal{O}}_k|E_a\rangle\langle E_b|\hat{\mathcal{O}}_k|E_m\rangle. \end{aligned} \tag{2.6}$$

To obtain this result we use the following property of the antiunitary operator Θ

$$\langle E^*_i|\hat{\mathcal{O}}^*_l|E^*_j\rangle = \langle E_i|\Theta^{-1}\hat{\mathcal{O}}^*_l|E^*_j\rangle^* = \langle E_i|\Theta^{-1}\hat{\mathcal{O}}^*_l\Theta|E_j\rangle^* = \langle E_i|\hat{\mathcal{O}}_l|E_j\rangle^*,$$

where we identify $\hat{\mathcal{O}}^*_l = \Theta\hat{\mathcal{O}}_l\Theta^{-1}$ per definition. $\langle\phi|\vartheta\rangle^*$ is the complex conjugate of $\langle\phi|\vartheta\rangle$. Using Eq. (2.5) the matrix elements of Eq. (2.6) in the diagonal subspace evaluate to [10]

$$\langle E_{n,\mathrm{L}}, E^*_{n,\mathrm{R}}|\hat{H}_{\mathrm{LR}}|E_{m,\mathrm{L}}, E^*_{m,\mathrm{R}}\rangle = \sum_{k=1}^{K}\left|\langle E_n|\hat{\mathcal{O}}_k|E_m\rangle\right|^2 \sim \sum_{k=1}^{K}|R^k_{nm}|^2 \sim K. \tag{2.7}$$

For the elements in the offdiagonal subspace we find

$$\langle E_{n,\mathrm{L}}, E^*_{m,\mathrm{R}}|\hat{H}_{\mathrm{LR}}|E_{a,\mathrm{L}}, E^*_{b,\mathrm{R}}\rangle \sim \sum_{k=1}^{K}R^k_{na}R^k_{bm} \sim \sqrt{K} \tag{2.8}$$

using the central limit theorem, where either $n \neq m$ or $a \neq b$ [10]. An intuitive argument for the scaling of the matrix elements in the diagonal subspace is that the terms in the sum of Eq. (2.7) are non-negative, whereas the terms in Eq. (2.8) have relative phases that can cancel each other, thereby

effectively reducing the magnitude of the sum.

Since we choose an extensive number of couplings $K \sim L$, we expect the coupling between states in the diagonal subspace to dominate in the thermodynamic limit. Based on this argument it is reasonable to assume that the ground state lies in this subspace for large chains, as does the thermofield-double state given in Eq. (2.2). Cottrell et al. also assume that $\hat{\mathcal{O}}_k$ only couple states that are close in energy. They find that the low-energy behavior of the Hamiltonian with a coupling as in Eq. (2.4) can be approximated by a single harmonic oscillator and the ground state has the same entanglement structure as the TFD with a gap $\Delta \propto T$. While Cottrell et al. did not explicitly test this outside of a simple toy model, we will investigate this in the following chapter.

One model that has been extensively studied over the last decade in the context of coupled chains is the spin-$\frac{1}{2}$ anisotropic Heisenberg model, which is commonly known as the *XXZ* model. For a chain of length L the Hamiltonian is given by

$$\hat{H}_{\mathrm{XXZ}} = \sum_{i=1}^{L} \left(J_{\mathrm{x}} \hat{\sigma}_i^{\mathrm{x}} \otimes \hat{\sigma}_{i+1}^{\mathrm{x}} + J_{\mathrm{x}} \hat{\sigma}_i^{\mathrm{y}} \otimes \hat{\sigma}_{i+1}^{\mathrm{y}} + J_{\mathrm{z}} \hat{\sigma}_i^{z} \otimes \hat{\sigma}_{i+1}^{z} \right), \tag{2.9}$$

where J_z is the anisotropy parameter and we introduce the spin-$\frac{1}{2}$ Pauli matrices $\hat{\sigma}^{\mathrm{x}} = (|\downarrow\rangle\langle\uparrow| + \mathrm{h.c.})$, $\hat{\sigma}^{\mathrm{y}} = (-\mathrm{i}|\downarrow\rangle\langle\uparrow| + \mathrm{h.c.})$, and $\hat{\sigma}^{z} = (|\uparrow\rangle\langle\uparrow| - |\downarrow\rangle\langle\downarrow|$ with h.c. standing for the Hermitian conjugate where $\{|\downarrow\rangle, |\uparrow\rangle\}$ are the spin-$\frac{1}{2}$ basis states. For $J_{\mathrm{z}} = J_{\mathrm{x}} > 0$ it reduces to the isotropic antiferromagnetic Heisenberg model that we will study in this work. In 1D this model is critical and exhibits gapless Nambu-Goldstone bosons called *magnons*. Its low-energy subspace is described by a conformal field theory.

Early works [55,43,54] have analyzed the coupled system via the entanglement Hamiltonian $\mathcal{H}_{\mathrm{S}}$ which is defined for the reduced density matrix of a subsystem, S, via

$$\rho_{\mathrm{S}} \propto \exp\left(-\mathcal{H}_{\mathrm{S}}\right)$$

up to normalization. If ρ_S is a Gibbs state, then $\mathcal{H}_S$ is trivially given by the subsystem Hamiltonian multiplied with the inverse temperature $\beta = 1/T$. For the TFD state we then expect that $\mathcal{H}_S \propto \hat{H}^0$, i.e., the Hamiltonian of the uncoupled chain. Using perturbative analysis for both $g \gg 1$ and $g \ll 1$, it was found that the reduced state on each chain is approximately equal to a Gibbs state in leading order for the coupling in Eq. (2.4) for certain models[43,54,55,45]. Recently, Seki & Yunoki undertook a large-scale numerical study using exact diagonalization to probe these predictions. They find the perturbative agreement with small deviations in the nonperturbative regime. The results of Seki & Yunoki are promising in that the fidelty, a measure for how similar two quantum states are, remains close to its optimal value of 1. Correlations seemingly improve for larger system sizes, potentially suggesting agreement in the thermodynamic limit. Given the difficulty of representing the exponentially large Hilbert space on a classical computer, this study was unable to probe system sizes larger than $L = 12$ using exact diagonalization however. In the following section we use tensor network algorithms, most notably the density-matrix renormalization group[60] and minimally entangled typical thermal state sampling[71], to explore this problem for long chains up to $L = 256$(cf. App. A for numerical details). We also provide a CFT perspective inspired by Maldacena & Qi that gives insights into the scaling of the correlation functions which we are ultimately interested in.

2.2 Coupled Spin-$\frac{1}{2}$ Heisenberg Models

Suppose we have two identical spin-$\frac{1}{2}$ antiferromagnetic isotropic Heisenberg models

$$\mathcal{H}^0 = \sum_{i=1}^{L-1} \left(\hat{\sigma}_i^x \otimes \hat{\sigma}_{i+1}^x + \hat{\sigma}_i^y \otimes \hat{\sigma}_{i+1}^y + \hat{\sigma}_i^z \otimes \hat{\sigma}_{i+1}^z \right) \tag{2.10}$$

as given in Eq. (2.9), i.e., $J_\mathrm{x} = J_\mathrm{z} \equiv 1$, with the coupling

$$\mathcal{H}_\mathrm{LR} = \sum_{i=1}^{L} \left(\hat{\sigma}^\mathrm{x}_{i,\mathrm{L}} \otimes \hat{\sigma}^\mathrm{x}_{i,\mathrm{R}} - \hat{\sigma}^\mathrm{y}_{i,\mathrm{L}} \otimes \hat{\sigma}^\mathrm{y}_{i,\mathrm{R}} + \hat{\sigma}^\mathrm{z}_{i,\mathrm{L}} \otimes \hat{\sigma}^\mathrm{z}_{i,\mathrm{R}} \right). \tag{2.11}$$

This has the form of the local coupling in Eq. (2.4) with an extensive number of coupling operators. We note that the operators in subsystem R are subject to CPT conjugation resulting in the relative -1 in front of the $\hat{\sigma}^\mathrm{y}_{i,\mathrm{L}} \otimes \hat{\sigma}^\mathrm{y}_{i,\mathrm{R}}$ term in Eq. (2.11). The ground state of Eq. (2.11) is

$$|\mathrm{GS, LR}\rangle = \bigotimes_{i=1}^{L} \frac{1}{\sqrt{2}} (|\uparrow_{i,\mathrm{L}}\rangle \otimes |\downarrow_{i,\mathrm{R}}\rangle - |\downarrow_{i,\mathrm{L}}\rangle \otimes |\uparrow_{i,\mathrm{R}}\rangle),$$

i.e., singlets $|s_{i,\mathrm{LR}}\rangle = (|\uparrow_{i,\mathrm{L}}\rangle \otimes |\downarrow_{i,\mathrm{R}}\rangle - |\downarrow_{i,\mathrm{L}}\rangle \otimes |\uparrow_{i,\mathrm{R}}\rangle)/\sqrt{2}$ shared across sites of the same index i. The full Hamiltonian of two coupled models is

$$\begin{aligned} H = &\sum_{i=1}^{L-1} \left[\hat{\sigma}^\mathrm{x}_{i,\mathrm{L}} \otimes \hat{\sigma}^\mathrm{x}_{i+1,\mathrm{L}} + \hat{\sigma}^\mathrm{y}_{i,\mathrm{L}} \otimes \hat{\sigma}^\mathrm{y}_{i+1,\mathrm{L}} + \hat{\sigma}^\mathrm{z}_{i,\mathrm{L}} \otimes \hat{\sigma}^\mathrm{z}_{i+1,\mathrm{L}} \right] \\ &+ \sum_{i=1}^{L-1} \left[\hat{\sigma}^\mathrm{x}_{i,\mathrm{R}} \otimes \hat{\sigma}^\mathrm{x}_{i+1,\mathrm{R}} + \hat{\sigma}^\mathrm{y}_{i,\mathrm{R}} \otimes \hat{\sigma}^\mathrm{y}_{i+1,\mathrm{R}} + \hat{\sigma}^\mathrm{z}_{i,\mathrm{R}} \otimes \hat{\sigma}^\mathrm{z}_{i+1,\mathrm{R}} \right] \\ &- g \sum_{i=1}^{L} \left[\hat{\sigma}^\mathrm{x}_{i,\mathrm{L}} \otimes \hat{\sigma}^\mathrm{x}_{i,\mathrm{R}} - \hat{\sigma}^\mathrm{y}_{i,\mathrm{L}} \otimes \hat{\sigma}^\mathrm{y}_{i,\mathrm{R}} + \hat{\sigma}^\mathrm{z}_{i,\mathrm{L}} \otimes \hat{\sigma}^\mathrm{z}_{i,\mathrm{R}} \right] \end{aligned} \tag{2.12}$$

which can be represented as a ladder configuration with each leg corresponding to an isotropic Heisenberg model and the inter-chain coupling across the rungs (cf. Fig. 2.1). We note that the choice of inter-chain coupling is fairly generic, as long as it includes local operators. For an efficient description in terms of matrix product states, we map this to a chain of length $2L$ with next-nearest neighbor interactions.

This model is critical for $g = 0$, as the individual chains are critical Heisenberg models. $g > 0$ opens a gap with the *rung singlet* phase emerging for $g \gg 1$, i.e., singlets shared across each rung of

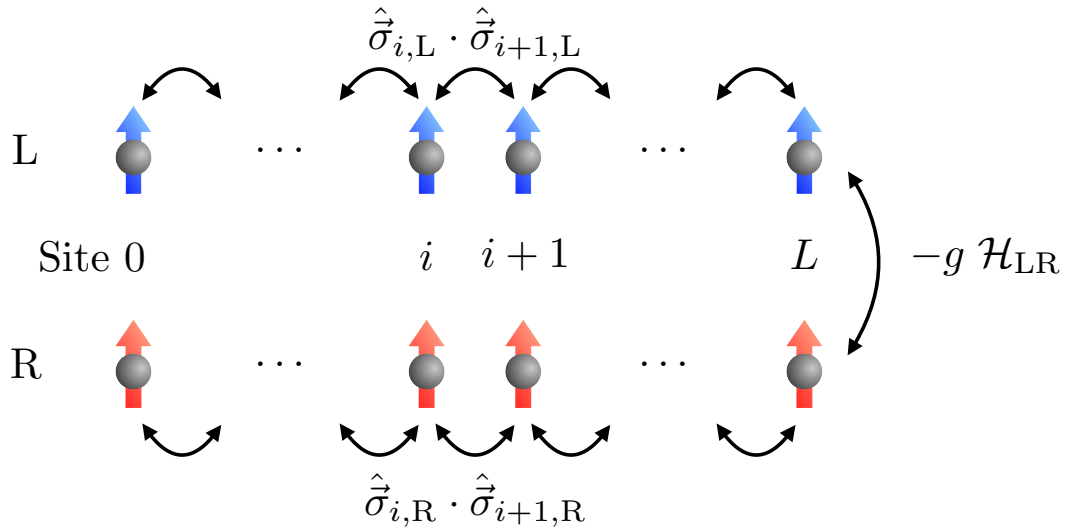

Figure 2.1: Illustration of two coupled spin-$\frac{1}{2}$ Heisenberg chains. We denote the chains as L (blue spins) and R (red spins)—each chain contains a total of L sites. The interaction within each chain is an isotropic Heisenberg coupling as in Eq. (2.10). The interchain interaction $\mathcal{H}_{\mathrm{LR}}$ is given in Eq. (2.11) with a relative coupling strength g.

the ladder. The $g \to \infty$ limit results in an infinite-temperature state on each leg of the ladder. This is evident from tracing out one half of a singlet giving

$$\rho_{i,\mathrm{L}} = \mathrm{Tr}_{i,\mathrm{R}} \left(|s_{i,\mathrm{LR}}\rangle\langle s_{i,\mathrm{LR}}| \right) = \frac{1}{2}\mathbb{I}_{2,\mathrm{L}}.$$

The reduced state of one left leg of the ladder is

$$\rho_{\mathrm{L}} = \mathrm{Tr}_{\mathrm{R}} \left(\bigotimes_{i=1}^{L} |s_{i,\mathrm{LR}}\rangle\langle s_{\mathrm{i,\,LR}}| \right) = \bigotimes_{i=1}^{L} \rho_{i,\mathrm{L}} = \frac{1}{2^L}\mathbb{I}_{L,\mathrm{L}},$$

where $\mathbb{I}_L = \bigotimes_{i=1}^{L} I_2$ is the identity matrix of a system consisting of L two-level systems, which coincides with the infinite-temperature Gibbs state $\lim_{\beta\to 0}(\rho_\beta)$ in Eq. (2.1).

Ultimately we are interested in the comparison between the Gibbs state and the coupled ground state at finite g by studying their spatial correlations within a single chain. We consider correlation

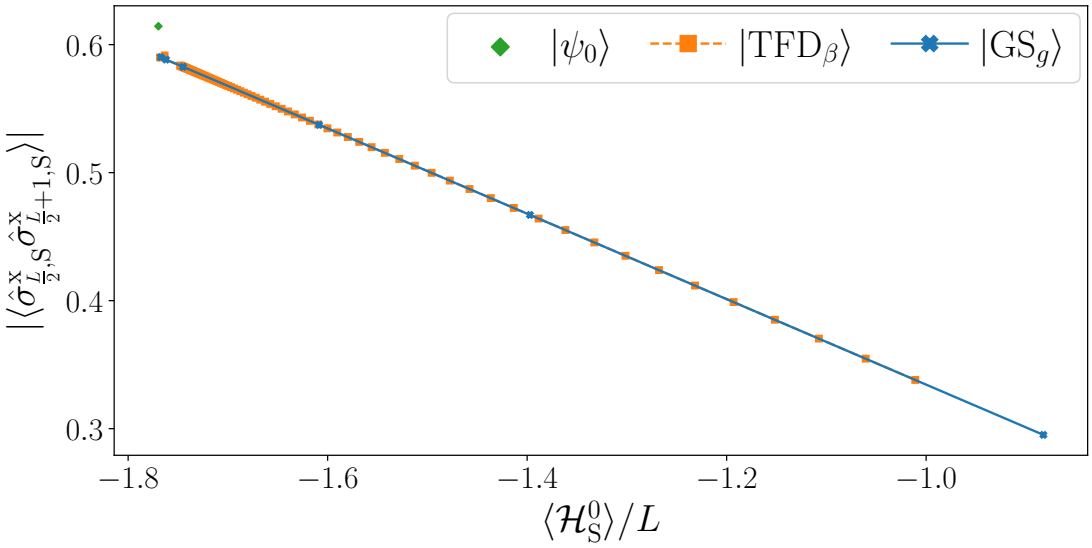

Figure 2.2: Short-range correlations of $\hat{\sigma}^{\mathrm{x}}_{\mathrm{S}}$ ($S \in \{\mathrm{L},\mathrm{R}\}$) for the coupled ground state $|\mathrm{GS}_g\rangle$, the Gibbs state $|\mathrm{TFD}_\beta\rangle$ and the ground state $|\psi_0\rangle$ of the uncoupled chain as a function of the single-sided energy density $\langle\mathcal{H}^0_{\mathrm{S}}\rangle/L$. There is excellent agreement between $|\mathrm{GS}_g\rangle$ and the $|\mathrm{TFD}_\beta\rangle$ at matching energy densities, suggesting a natural way of comparing the coupled ground state and the TFD. $L = 256$.

functions of the form

$$|\langle\hat{\sigma}^{\mathrm{x}}_{\mathrm{S},\frac{L}{2}}\hat{\sigma}^{\mathrm{x}}_{\mathrm{S},\frac{L}{2}+d}\rangle| = |\langle\psi|\hat{\sigma}^{\mathrm{x}}_{\mathrm{S},\frac{L}{2}}\hat{\sigma}^{\mathrm{x}}_{\mathrm{S},\frac{L}{2}+d}|\psi\rangle|, \tag{2.13}$$

as a function of the distance d between the sites in a single chain $\mathrm{S} \in \{\mathrm{L},\mathrm{R}\}$ for $|\psi\rangle \in \{|\mathrm{GS}_g\rangle, |\mathrm{TFD}_\beta\rangle, |\psi_0\rangle\}$ with the ground state of a single Heisenberg chain $|\psi_0\rangle$. Note that there is no difference between expectation values in one of the two legs of the ladder and in the choice of the Pauli matrix $\hat{\sigma}^\alpha$ ($\alpha \in \{\mathrm{x},\mathrm{y},\mathrm{z}\}$). We can neglect single expectation values $\langle\hat{\sigma}^\alpha_{i,\mathrm{S}}\rangle = 0$ for $\alpha = \mathrm{x},\mathrm{y},\mathrm{z}$ and $\mathrm{S} \in \{\mathrm{L},\mathrm{R}\}$ as they vanish for all states. Taking the absolute value avoids oscillations between positive and negative values due to the antiferromagnetic interaction.

A subtlety is the comparison between these two states which have different tunable parameters: β for the thermofield-double state $|\mathrm{TFD}_\beta\rangle$ and g for the coupled ground state $|\mathrm{GS}_g\rangle$. One approach is

maximizing the fidelity

$$F(\beta, g) = |\langle \mathrm{TFD}_\beta | \mathrm{GS}_g \rangle|,$$

i.e., the overlap between the thermofield-double state at inverse temperature β and the coupled ground state at coupling strength g. However this is inefficient to obtain numerically for large β, therefore significantly limiting this approach. Instead we follow a proposal by Seki & Yunoki and match the energy density in the single Heisenberg models

$$\begin{aligned} \varepsilon_\beta &= \frac{1}{L} \langle \mathrm{TFD}_\beta | \mathcal{H}^0 | \mathrm{TFD}_\beta \rangle \text{ and} \\ \varepsilon_g &= \frac{1}{L} \langle \mathrm{GS}_g | \mathcal{H}^0_{\mathrm{L}} | \mathrm{GS}_g \rangle. \end{aligned} \tag{2.14}$$

Fig. 2.2 depicts the nearest-neighbor correlations, i.e., $d = 1$, as a function of the energy density of the corresponding state. We find excellent agreement between $|\mathrm{GS}_g\rangle$ and $|\mathrm{TFD}_\beta\rangle$ at matching energy density, further motivating this approach to comparing the coupled ground state with a TFD.

Our procedure then becomes the following: we calculate $|\mathrm{GS}_g\rangle$ and then sweep β to find $|\mathrm{TFD}_\beta\rangle$ such that $|\varepsilon_g - \varepsilon_\beta| < \delta\varepsilon$ where we choose a small $\delta\varepsilon \sim 10^{-2}$ in natural units of the Hamiltonian. For small $\beta \lesssim 1$ we can use imaginary time evolution methods to obtain the thermofield-double state. For $\beta > 1$ and large system sizes, where imaginary time evolution becomes unfeasible, we employ algorithms using minimally entangled typical thermal states[71] which sample expectation values of Gibbs states.

Given the agreement at short range, Fig. 2.3 shows the long-range correlations in Eq. (2.13) at coupling strengths $g = 0.05, g = 0.6$ and $g = 2.0$. In Fig. 2.3a) ($g = 0.05$) we see that the correlations at short distances coincide for all three states, while the long-range values of the Gibbs

state differ from the other two. Interestingly the coupled and single ground states show similar correlations across the relevant length scales for $g = 0.05$. In the thermodynamic limit conformal invariance predicts that $|\psi_0\rangle$ exhibits power-law correlations

$$C(d) \equiv |\langle\psi_0|\hat{\sigma}^x_{S,\frac{L}{2}}\hat{\sigma}^x_{S,\frac{L}{2}+d}|\psi_0\rangle| \propto d^{-\Phi}$$

for some $\Phi > 0$. Due to $|GS_g\rangle$ having a finite gap to the first excited state for $g > 0$ we know that it must have a correlation length ξ_{GS} that diverges as $g \to 0$. In general, we expect the correlations of the coupled ground state to have the following form

$$C(d) \propto d^{-\Phi} \cdot e^{-\frac{d}{\xi_{GS}}},$$

i.e., a power-law at short distances and exponential decay at large separation d. A similar relation holds for the thermofield-double state but with a different correlation length ξ_{TFD}.

As the coupling strength between the two models is increased to $g = 0.6$ and $g = 2.0$ there is a clear separation between the coupled and single ground state with $|GS_g\rangle$ approaching the correlations of the Gibbs state (cf. Fig. 2.3b) and c)). We clearly observe the exponential decay predicted for $|GS_g\rangle$. While the long-range behaviors of the coupled ground state and the thermofield-double disagree at any of the displayed coupling strengths, this disagreement at large g and long distances is exponentially small due to the fast decay of the correlations.

One useful way of understanding the scaling of correlations is to investigate their correlation lengths ξ_{GS} and ξ_{TFD}, as we tune the coupling strength and the temperature. As previously discussed the renormalization group predicts that the correlation length scales as

$$\xi \propto |\tau|^{-\nu} \tag{2.15}$$

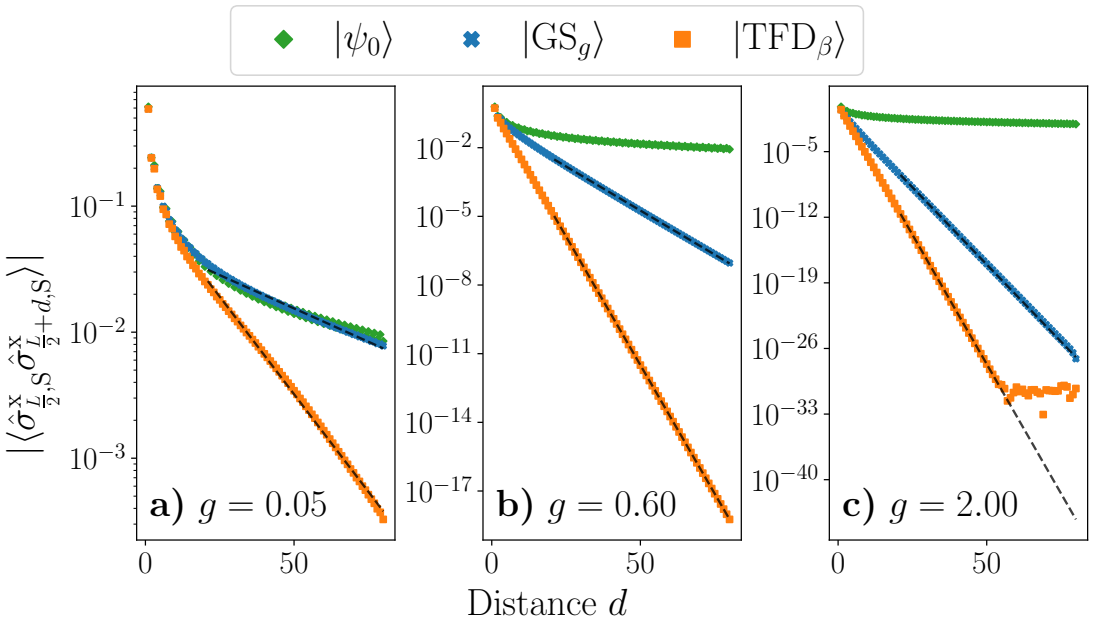

Figure 2.3: Comparison of spatial correlations for the coupled ground state $|\mathrm{GS}_g\rangle$, the Gibbs state $|\mathrm{TFD}_\beta\rangle$ and the single ground state $|\psi_0\rangle$ for **a)** $g = 0.05$, **b)** $g = 0.6$, and **c)** $g = 2.0$. Dashed lines correspond to the fit we used to extract the correlation length ξ. The values for $d > 50$ in c) are limited by numerical precision. $L = 256$.

with the critical exponent ν and a parameter τ controlling the strength of the perturbation. Here $\tau = g$ with ν_g for the coupled ground state. The correlation length of the Gibbs state has the same scaling with $\tau = T$ and exponent ν_T—we note however that this is not related to criticality but rather to the finite-temperature behavior of the conformal field theory[13].

Fig. 2.4 shows the correlation length extracted from correlations as in Fig. 2.3 for both the coupled ground state and the TFD state. We find $\nu_g = 0.94(6)$ for $L = 256$, where the error is given by the standard deviation of the fit. Conformal field theory[74,35] predicts the relation

$$\nu = \frac{1}{D - \Delta_\varepsilon} \tag{2.16}$$

for the critical exponent where D is the sum of the spatial and temporal dimensions (here $D = 2$)

and Δ_ε is the scaling dimension of the relevant operator in the perturbation. For Eq. 2.11, this is double the scaling dimension $\frac{1}{2}$ of the spin operator in each Heisenberg model, i.e., $\Delta_\varepsilon = 2 \cdot \frac{1}{2} = 1$. Therefore we expect $\nu_g = 1$ which is close to our observation.

For the thermal correlations a similar analysis gives $\nu_T = 0.94$ with a statistical error of ± 0.06. We note that obtaining the correlation length at intermediate temperatures $T \sim 1$ was a numerically challenging task resulting in possible outliers. However these had little impact on the fit. The ideal exponent ν_T can be obtained from the finite-temperature behavior of the CFT for the quantum model. This behaves like the finite-size scaling by identifying the inverse temperature $\beta = T^{-1}$ with the system size L [13]. Conformal invariance then gives

$$\xi_{\mathrm{TFD}} \propto L \propto \beta = T^{-1},$$

i.e., an exponent $\nu_T = 1$ which is close to our result. While we find that the exponents for the thermal state and the ground state of the coupled model are consistent with predictions within the error margin, the agreement between them is remarkable. It is noteworthy that the agreement in the CFT predictions, i.e., $\nu_g = \nu_T$, is specific for the model considered here and not a general feature.

The scaling of the correlation lengths suggests that $|\mathrm{GS}_g\rangle$ and $|\mathrm{TFD}_\beta\rangle$ can be matched via their correlation lengths. This would imply an equivalence between the coupling strength g and the temperature T as

$$\frac{\xi_{\mathrm{GS}}}{\xi_{\mathrm{TFD}}} \propto \frac{g}{T} = \text{const.}$$

However neither the energy densities nor the short-range correlations would agree in that case, raising questions about the physical interpretation of this matching approach.

At small coupling strength we can use perturbation theory to study the properties of the coupled

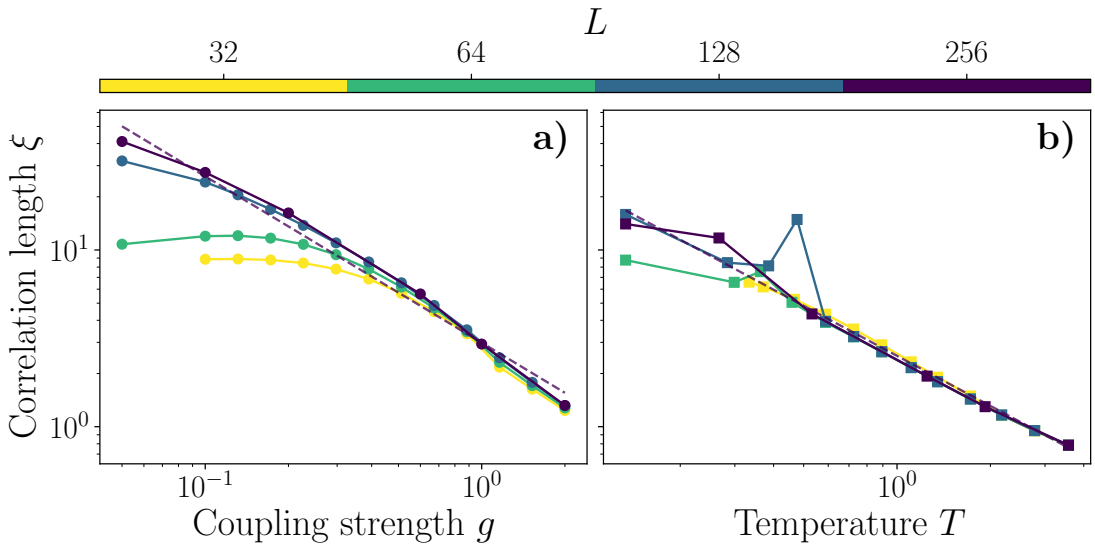

Figure 2.4: Finite-size scaling of the correlation length ξ for the coupled ground state and the thermofield-double state. **a)** The correlation length of $|\mathrm{GS}_g\rangle$ as a function of the coupling strength g for system sizes $L = 32$ to $L = 256$. A power-law emerges at sufficiently large g with saturation at weak coupling strength. We identify a scaling of $\xi_{\mathrm{GS}} \propto g^{-0.94}$. **b)** The correlation length of the TFD also exhibits a power-law scaling with the exponent $\nu_T = 0.94$ which agrees well with the exact CFT prediction $\nu_T = 1$ [13,6]. At low temperature, we see an improvement in the finite-size scaling from $L = 32$ to $L = 256$.

ground state. Importantly this limit is of particular interest as it corresponds to low temperatures. Consider the limit $g \to 0$ which recovers the single ground state in each model, i.e., the $T = 0$ thermofield-double, and the limit $g \to \infty$ giving an infinite-temperature TFD on each leg of the ladder. The energy of the coupled ground state is a monotonic function of g, as is the energy of the thermofield-double state, meaning that there must be some monotonic function relating g and T. From this argument we know that at sufficiently small coupling strength the Gibbs state at the same energy will be at very low temperature which is ultimately our region of interest.

Consider the following Hamiltonian

$$\mathcal{H}^0_{\mathrm{LR}} = \mathcal{H}^0_{\mathrm{L}} + \mathcal{H}^0_{\mathrm{R}} - g\, V_{\mathrm{d}} \tag{2.17}$$

where we define V_{d} as the inter-chain Hamiltonian in Eq. (2.4) restricted to the diagonal subspace

$$V_{\mathrm{d}} = \sum_{k=1}^{N} \sum_{n,m} \langle E_{n,\mathrm{L}}, E^*_{n,\mathrm{R}} | \hat{\mathcal{O}}_{k,\mathrm{L}} \otimes \hat{\mathcal{O}}^*_{k,\mathrm{R}} | E_{m,\mathrm{L}}, E^*_{m,\mathrm{R}} \rangle \cdot | E_{n,\mathrm{L}}, E^*_{n,\mathrm{R}} \rangle \langle E_{m,\mathrm{L}}, E^*_{m,\mathrm{R}} |.$$

Following the arguments of Cottrell et al. the ground state of $|\psi^0_{\mathrm{gs}}\rangle$ of $\mathcal{H}^0_{\mathrm{LR}}$ takes the form of the thermofield-double state $|\mathrm{TFD}_\beta\rangle$ at some $\beta = T^{-1}$. We then consider the perturbation

$$\begin{aligned} V_{\mathrm{o}} &= \mathcal{H}_{\mathrm{LR}} - V_{\mathrm{d}} \\ &= \sum_{k=1}^{N} \sum_{\substack{n,n',m,m' \\ n \neq n', m \neq m'}} \langle E_{n,\mathrm{L}}, E^*_{n',\mathrm{R}} | \hat{\mathcal{O}}_{k,\mathrm{L}} \otimes \hat{\mathcal{O}}^*_{k,\mathrm{R}} | E_{m,\mathrm{L}}, E^*_{m',\mathrm{R}} \rangle \cdot | E_{n,\mathrm{L}}, E^*_{n',\mathrm{R}} \rangle \langle E_{m,\mathrm{L}}, E^*_{m',\mathrm{R}} | \end{aligned} \tag{2.18}$$

which is given by Eq. (2.4) restricted to the offdiagonal subspace. The first-order correction in g to $|\psi^0_{\mathrm{gs}}\rangle$ is

$$\begin{aligned} |\psi^1_{\mathrm{gs}}\rangle &= g \sum_{k>0} |k\rangle \frac{\langle k | V_{\mathrm{o}} | \psi^0_{\mathrm{gs}} \rangle}{E_k - E_0} \\ &\approx \frac{g}{\Delta} \sum_{k>0} |k\rangle \langle k | V_{\mathrm{o}} | \psi^0_{\mathrm{gs}} \rangle \equiv \frac{g}{\Delta} \partial |\psi^1\rangle, \end{aligned} \tag{2.19}$$

where $|k\rangle$ are the excited states of $\mathcal{H}^0_{\mathrm{LR}}$ with energy E_k, E_0 is the energy of the ground state and $\Delta = E_1 - E_0 > 0$ is the energy gap to the first excited state. We approximate the gap to higher excited states to be constant $E_k - E_0 \approx \Delta$. It follows that the first-order correction to the unperturbed ground state scales as $\frac{g}{\Delta}$.

In Fig. 2.5 we investigate the scaling of the energy gap of Eq. (2.12) as a function of the coupling strength for increasingly large ladders. At large g we observe an absence of finite-size effects indicating good convergence. However as we approach smaller coupling strengths $g \approx 0.1$, there are clear deviations due to finite-size effects. Instead of decreasing with g, Δ saturates at some value Δ_0. This

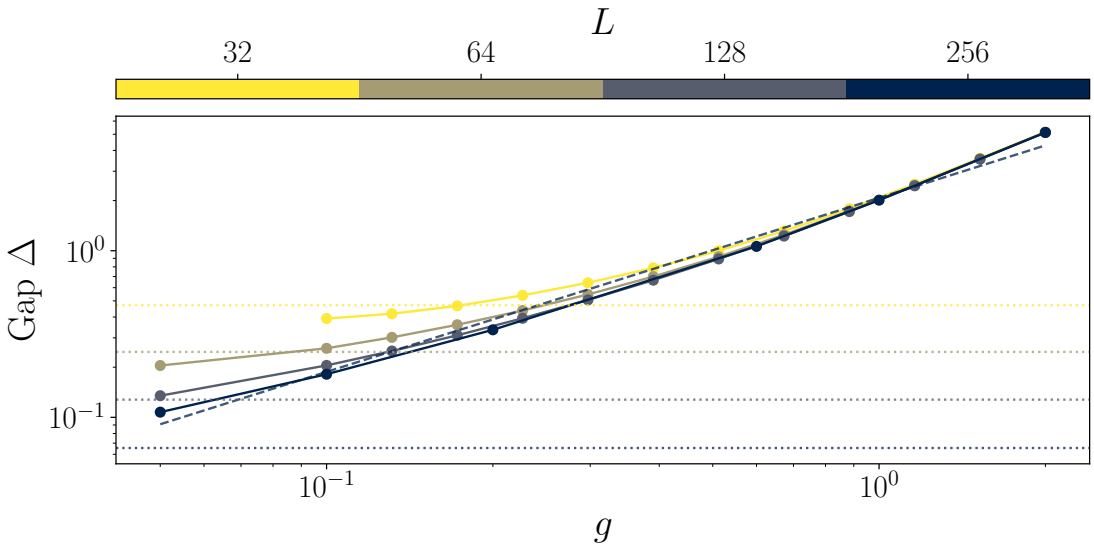

Figure 2.5: Scaling of the energy gap Δ of the coupled model as a function of the coupling strength g for chain sizes $L = 32$ to $L = 256$. While the gap is converged in system size for $g \gtrsim 1$, the low g regime shows finite-size effects due to the gap of the uncoupled model (dotted lines). We extract the scaling $\Delta \propto g^{1.04}$ from the fit for $L = 256$ (dashed line).

value decreases as the system size increases. We attribute this to the finite gap of the single Heisenberg models. For finite system sizes, the energy gap of Eq. 2.10 scales as $\Delta_0 \propto L^{-1}$ which we observe in the dashed lines in Fig. 2.5 [6].

This behavior at small coupling strengths is consistent with our results for the correlations: if the gap of the coupled ground state is below Δ_0, $|\mathrm{GS}_g\rangle$ is roughly given by the individual ground states of the decoupled chains, i.e., $|\mathrm{GS}_g\rangle \approx |E_0, E_0^*\rangle$. This may still be the case very close to Δ_0 explaining the observation that the correlations of the coupled ground state agrees remarkably well with those of the decoupled ground state $|\psi_0\rangle$ at low g.

Most importantly for our analysis, for $L = 256$ the scaling is approximately $\Delta \propto g^{1.04}$, where we extracted the exponent $1.04(5)$ from a power-law fit. From CFT arguments [6] one finds that the

energy gap of the model scales inversely proportional to the correlation length, i.e.,

$$\Delta \propto \xi_{\mathrm{GS}}^{-1} \propto g^{\nu_g},$$

as per our previous analysis, where we found $\nu_g = 0.94(6)$ which agrees reasonably well with our results from the gap scaling. We therefore assume that $\Delta \propto g$. The first-order correction to the TFD as the coupled ground state scales as

$$|\psi_{\mathrm{gs}}^1\rangle \approx \frac{g}{\Delta}\partial|\psi^1\rangle \propto \frac{g}{g}\partial|\psi^1\rangle = \partial|\psi^1\rangle,$$

i.e., it is marginal in the coupling strength. Therefore, we would expect to see no improvement in the agreement between the TFD and the coupled ground state as we approach $g = 0$. This is in line with our observations for the correlations.

Lastly we investigate the scaling between the coupling strength and the temperature at matching energy density to test the hypothesis by Cottrell et al. that the gap scales linearly in the temperature. As previously discussed we know that g and T must be uniquely related to one another. We find the scaling

$$T \propto g^{0.88}$$

with a statistical error of ± 0.05 for the exponent. Therefore, the gap $\Delta \propto T^{1.18}$ which is a significant deviation from the prediction of Cottrell et al.. While the Heisenberg model is integrable and therefore not accurately described by the eigenstate thermalization hypothesis, we note that our results did not change significantly upon adding integrability-breaking terms, e.g., a next-nearest neighbor interaction. This suggests that the ETH description may be incomplete, requiring a more thorough investigation for realistic models of the form in Eq. 2.3.

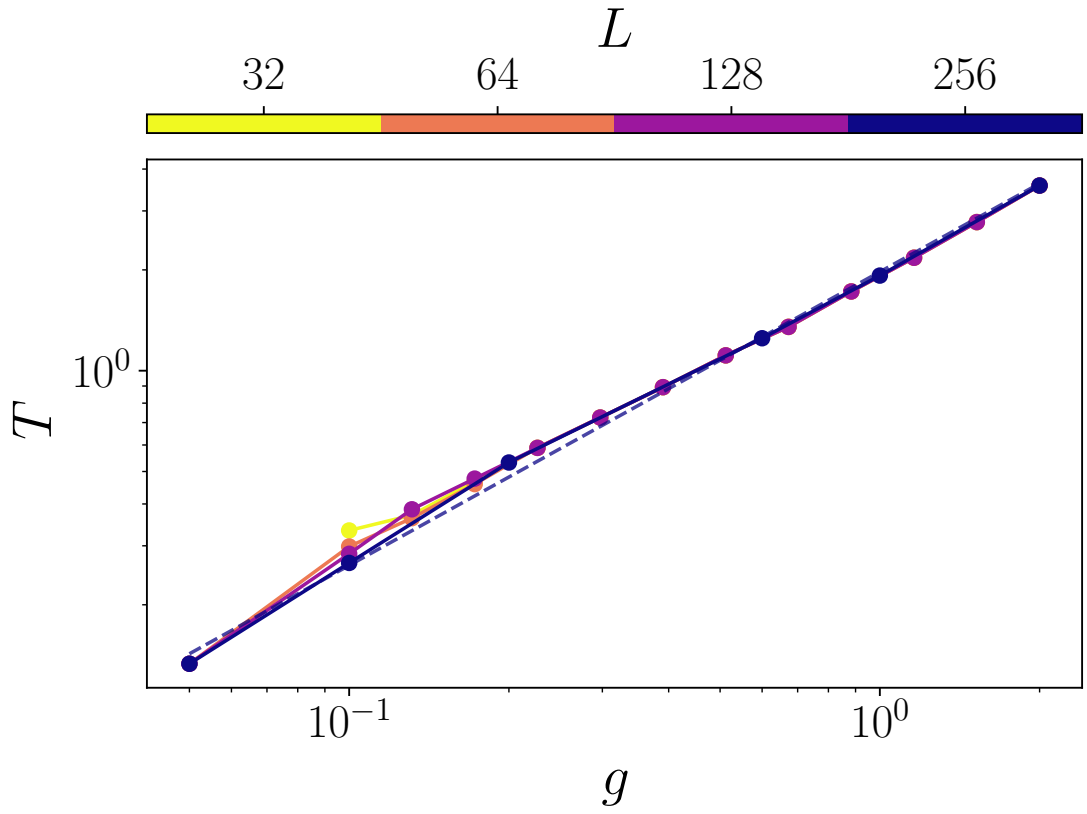

Figure 2.6: Relation between the temperature T and coupling strength g at matching energy density. The scaling for $L = 256$ corresponds to $T \propto g^{0.88}$, deviating from the prediction $T \propto g$ according to Cottrell et al.. This scaling is consistent across all system sizes.

3

Discussion and Outlook

In this section, we first recapitulate the results of our investigation on preparing low-entropy states in Rydberg atom arrays, provide a discussion of our results, and ultimately give an outlook for open questions and future investigations. As our approach is a proof of concept, we will also highlight how our ideas can be translated into other experimental platforms for quantum simulation including trapped ions and optical lattices.

Conformal Cooling using Rydberg Atom Tweezer Arrays

We investigated the 1D Rydberg blockade Hamiltonian as an interesting candidate to perform conformal cooling for two reasons: the ability to spatially modulate the interaction strength by changing the interatomic distance in a subsystem and its rich phase diagram. In particular our exploration focuses on the $\mathbb{Z}_2$ phase and the critical point between the $\mathbb{Z}_2$ and disordered phases. In the ordered phase we find that quantum many-body scars are a significant detriment for our procedure leading to nonthermal behavior and the subsequent break down of thermodynamic arguments for conformal cooling. This is likely caused by the factorization of the Hilbert space into dynamically disconnected subsectors. While the dynamics within each subsector may be ergodic on short time scales, ergodicity is broken on long time scales that exceed the scope of current numerical methods.

Recent research [12,53] suggests that many-body scarring breaks down near criticality. In our investigation we indeed find the restoration of ergodicity, however, a lack of diffusion persists. From the analysis of Ljubotina et al. and Chen et al. it is known that energy transport in this regime is superdiffusive. However thermalization did not occur in any of the systems probed here. This may be due to the long time scale for thermalization in this model, limiting the scope of the current investigation. In light of this, the observation, that cooling can surpass thermodynamic predictions for transient time scales, raises the question behind the necessity to thermalize. Instead, we can decouple the system from the ramp and bath regions when the cooling is optimal. Afterwards, the system can thermalize on its own, potentially to perform conformal cooling again by combining it with copies that were also subjected to conformal cooling. While it may seem sufficient to recycle the bath and rescale it appropriately to reach temperatures below the system's temperature during this repeated cooling process, this is inefficient in terms of the required time scale for thermalization. On the one hand, it may be necessary to go to very small rescaling factors $\lambda_{\text{bath}} \sim 0.1$ such that the time scale for thermalization increases and transport properties, e.g., the energy variance in the bath,

deteriorate. On the other hand, this can lead to long-lived modes localized at the boundary between the system and the bath which hinder energy transport[51]. Therefore it is crucial to repeat the process with identical copies—a disadvantage of this procedure is that the number of required copies increases with the number of cycles.

While the precise nature of overcooling is left for future investigation, we present evidence that it is a finite-size effect originating at the boundary of the system and the ramp. Intriguingly, the observation that this transient cooling is reversed after a short time is consistent with results for free fermions[36]. The work by Kuzmin et al. finds that the 1D transverse-field Ising model also exhibits cooling with rapid reabsorption. They explain this in terms of the propagation of low-energy quasiparticles. Importantly, due to the spatial modulation of the Hamiltonian these quasiparticles have a position-dependent velocity. This leads to the quasiparticles slowing down in the bath region effectively to get stuck there for some time, before being reflected at the boundary and returning into the system. This agrees well with our observations including the plateaus in Fig. 1.8a). While our work considers high-temperature initial states, Kuzmin et al. deal with initial states close the ground state. This leads us to believe that overcooling may be related to similar low-energy quasiparticles which are more mobile due to longer length-scales close to the critical point. This establishes an interesting connection between criticality, which mostly concerns low-energy behavior, and high-energy transport.

This quasiparticle picture also gives rise to a toy model explaining the t^2-scaling of the average energy density of the system during overcooling in Fig. 1.5b). Consider noninteracting particles with energy E hopping on a lattice. Every site i emits particles at a constant rate $\Gamma_i \propto \lambda_i \Gamma$ with the emission rate Γ in the system, i.e., sites in the system emit at a higher rate than particles in the bath. A particle hopping over the system-bath boundary into the bath constitutes a loss of energy E. The

rate at which the system loses energy is roughly given by

$$\Gamma_S(t) \equiv \frac{\partial}{\partial t} E_S \propto \Gamma \ (\lambda_{\text{bath}} - 1)\, A(t),$$

where we assume a flat bath with Hamiltonian magnitude λ_{bath}. $A(t)$ is the area whose particles can reach the boundary within time t. Given that the particles propagate ballistically at a constant rate from the system to the bath, we can reasonably assume that this area grows linearly in time, i.e., $A(t) \propto t$, such that

$$\Gamma_S(t) \propto \Gamma \ (\lambda_{\text{bath}} - 1) \ t.$$

By integrating this we find that the energy in the system decreases quadratically, as we find in the numerics. This toy model corresponds roughly to a biased random walk in 1D. This opens an interesting opportunity to study overcooling from a statistical mechanics perspective, e.g., by deriving a Boltzmann-type transport equation [36]. Of course, the presented toy model is highly simplified. More realistic models should take the finite heat capacity in the bath into account and consider a Stefan-Boltzmann law for the emission rate such that emission depends on the energy, or equivalently the temperature, of a given site. This requires careful consideration so we leave this for future studies.

There is an interesting prospect to exploit overcooling in 1D arrays by increasing the boundary between the system and the bath region. Instead of having one well-defined system region coupling to a bath, it may be possible to split the system into subsets with each coupling to a bath, e.g., via a periodic spatial modulation of the Hamiltonian. A similar setup was considered by Wen et al. however with periodic driving in a conformal field theory. They identify heating regions in space which absorb entropy and energy from the rest, leaving the reduced state of the cooling region in

its ground state. It would be interesting to investigate whether this also happens in models that are within experimental capabilities. Fig. 1.5a) shows that cooling is not uniform and that certain sites cool significantly more than the entire system region. Therefore, periodic spatial modulations could be useful to remove as much energy as possible from a series of small subsystems which are eventually combined. While this may lead to improvements in the energy density, we need to take into account that many-body correlations are limited to each small subsystem. It may be possible to equilibrate these small systems together to potentially resolve this limitation.

Quantum simulation algorithms at finite temperature may be another application that would not explicitly require equilibration[42]. A key feature is the efficient preparation of initial states at low, but finite energy density. We demonstrated that our approach can significantly decrease the energy density within a few microseconds (cf. Sec. 1.2.2) for reasonable experimental parameters[15,66]. This may be sufficient for the proposal of Lu et al. to study finite-temperature properties of many-body systems.

The transverse-field Ising model is a possible first toy model to test this idea of repeatedly performing conformal cooling on a system by decoupling the baths and "stitching" together the remaining system. In the second cooling cycle, some of these system would then take the role of the bath. This introduces a non-local coupling in the second cycle therefore precluding the Jordan-Wigner transformation. However despite this supposed breakdown of integrability, it still takes the form of a local transverse-field Ising model, limiting the growth of entanglement and making it amenable to matrix product state algorithms. In terms of conformal cooling this model does not thermalize according to ETH which means that thermodynamic arguments do not apply. For thermalizing models it may be possible to reach sufficiently large systems and time scales using density matrix truncation[83]. This numerical method has successfully been employed to study spin transport and may be adapted for conformal cooling[89].

Ultimately however the observed cooling was not sufficient to reach temperatures where we

would expect to see order. We identify two reasons: First, the temperature of the initial state is a limiting factor. Starting at very high temperature may require going to very low coupling strengths in the bath, $\lambda_{\text{bath}} \ll 1$, which can deteriorate the protocol as observed in our results. At the same time it is important to consider the temperatures needed to observe order. The Rydberg blockade model has a quantum phase transition with no finite-temperature order. This means that we need to cool below the energy gap of the Hamiltonian to observe the desired order. It is possible to circumvent this limitation by investigating models that exhibit finite-temperature phase transitions, e.g., as considered by Zaletel et al.. In the context of Rydberg atoms in tweezer arrays, the 2D quantum transverse-field Ising model is a candidate which can be straightforwardly implemented on current experimental setups [14] and exhibits a finite-temperature phase transition [78]. The temperatures required for this transition are on the order of the interaction strength which should be feasible for conformal cooling. Here it is also promising to use conformal cooling to prepare low-energy states that are then used for digital quantum simulation [42].

Another more speculative application of conformal cooling in the context of Rydberg atom tweezer arrays is in combination with adiabatic methods to achieve more efficient state preparation. As previously mentioned one key disadvantage of adiabatic preparation is its inefficiency upon approaching a critical point. We envision a protocol where one follows an adiabatic path close to the critical point, then performs conformal cooling across the region where the energy gap closes and finally continues on an adiabatic path. Assuming that the ground state on one side of, but still close to, the phase transition is an low-energy state with regards to a near-critical Hamiltonian on the other side of the critical point, conformal cooling may be useful to remove the low-energy excitations, that are created during the quench, leaving behind a subsystem close to its ground state. Therefore it may also improve the quantum Kibble-Zurek mechanism [90]. The overall idea falls under the category of shortcuts to adiabaticity and would be most useful for models with a gap that vanishes exponentially in the system size at the critical point, where adiabatic methods fail. A re-

cent example of such a model is given by Schiffer et al. as a quasi-1D Rydberg blockade model with a unit cell of three Rydberg atoms arranged in an isosceles triangle. While Schiffer et al. study this model from the perspective of quantum optimization, it is an interesting model to explore many-body phases using conformal cooling in near-term experiments.

Adiabatic Preparation of Thermofield-Double States using Rydberg Tweezer Arrays

In addition to the dynamical conformal cooling protocol we also studied the adiabatic preparation of thermofield-double states. Here we investigated the ground state of two coupled isotropic antiferromagnetic Heisenberg chains. This is motivated by predictions that this ground state is approximately given by a thermofield-double state [10,45] which would open the possibility of preparing Gibbs states using tweezer arrays to study finite-temperature phenomena. Our investigation reaches system sizes surpassing any previous study by employing matrix product state algorithms (cf. App. A). We also provide conformal field theory arguments to complement our numerical results.

While we find excellent agreement between the short-range correlations of the coupled ground state and the Gibbs states at matching energy density, there is disagreement at long separations. Our tensor network approach enables this comparison whereas previous studies were limited to short length scales. In particular, we extract the correlation length from these results which are an important figure of merit for studying phases of matter. Interestingly our results indicate the same correlation length scaling exponent of $\nu = 1$ for both states which is in agreement with predictions from conformal field theory. Here it is important that the exponent of the thermal correlation length is always fixed. This is in contrast to the coupled ground state for which it depends on the scaling dimension of the perturbing operator Δ_ε, $\nu = (D - 2\Delta_\varepsilon)^{-1}$ in $D + 1$ dimensions. Therefore it is merely coincidental that the scaling agrees for this model and choice of coupling operators

and is not a general feature. Given that the observed disagreement is exponentially vanishing in the distance, we believe that a mismatch of correlation lengths is not necessarily detrimental to our approach.

On the other hand, a perturbative argument suggests that the first-order correction to the TFD is proportional to g/Δ, where Δ is the energy gap between the ground and first excited state of the coupled model. In the isotropic antiferromagnetic Heisenberg model the gap scales as $\Delta \propto g$ in good agreement with CFT predictions, such that the correction is marginal, i.e., nonvanishing as g goes to 0. This suggests that we need to identify a model with a sublinear gap scaling $\Delta \propto g^{\alpha}$ ($\alpha < 1$) for the first-order correction to vanish in the limit $g \to 0$. An example of this is the critical spin-1 Potts model, a generalization of the Ising model for spin-1 particles. For the right choice of local coupling operators it can be shown that the gap scales as $\Delta \propto g^{\frac{2}{3}}$. Thus, the first-order correction vanishes as $g^{\frac{1}{3}} \to 0$ for $g \to 0$ in the thermodynamic limit. This is a natural next step to verify this perturbative argument. We note however that the Potts model is not easily implemented in current Rydberg atom tweezer arrays. The (an-)isotropic antiferromagnetic Heisenberg model on the other hand has been studied before by coupling two highly excited Rydberg states and dressing one of them with the electronic ground state, leading to an interaction as in Eq. (2.9)[2,7].

Near-Term Experimental Implementations

Both of our approaches, conformal cooling quenches and adiabatic preparation of thermofield-double states, are studied with current Rydberg atom tweezer array experiments in mind.

Our adiabatic approach should be straightforward to adopt: First, one prepares L pairs of Rydberg atoms in singlet states at large separation—this corresponds to the $g \to \infty$ or infinite-temperature limit. Afterwards one would move these pairs closer together, leading to interactions between them, assuring adiabaticity along this path. This constraint is fairly straightforward to

follow given the known gap scaling of $\Delta \propto g$. The runtime of the algorithm can then be lower-bounded by $(\min_g(\Delta))^{-2} = g_f^{-2}$ [77] where g_f is the desired final coupling strength. While this diverges as $g_f \to 0$, adiabatic passage is ensured for any finite g_f with the advantage that one can stop the evolution when it becomes too slow and still obtain a ground state close to a TFD state at some temperature determined by the final coupling strength. At the end of this evolution, one would simply discard the Rydberg atoms in one of the two ladders which corresponds to taking the partial trace, leaving the rest of the Rydberg atoms in a reduced state that is similar to a Gibbs state at short-range. Spatial adiabatic passage [48] is a well-established method for ultracold atoms trapped in tweezer arrays. Therefore our proposal for the adiabatic preparation of thermofield-double states is well within experimental capabilities and presents an opportunity to study finite-temperature phenomena using analog Rydberg atom array simulators.

Conformal cooling on the other hand requires the more specialized ability to spatially modulate the Hamiltonian which is not yet fully developed. The interaction terms can be rescaled rather easily based on the movement of the optical tweezers. There are also ongoing developments [1] to establish this capability for the laser detuning Δ using AODs leaving only the site-dependent Rabi frequency Ω as a necessary ingredient. This requires a magnetic field gradient across the tweezer array. While magnetic field gradients are a standard tool in many atomic experiments, e.g., in the context of magneto-optical traps, it may be difficult to generate them at the required micrometer scale in the context of optical tweezers. As of the time of writing this, we are not aware of any efforts on this end.

Interestingly it may be possible to perform conformal cooling using Rydberg atom tweezer arrays in the XXZ model instead. As previously pointed out, this can be naturally implemented as well by coupling two highly excited Rydberg states and dressing one of them with the electronic ground state. This results in a flip-flop interaction that decays as R^{-3} in the interatomic distance R. A recent investigation has identified multiple many-body phases and interesting critical behavior [39]

making it a natural alternative for exploring conformal cooling. While it is noteworthy that long-range interactions may lead to subtleties in the treatment of conformal cooling, we think that this is negligible as they decay sufficiently fast—we confirmed this in the long-range Rydberg blockade model (cf. Eq. (1.6)) in comparison with the nearest-neighbor model.

As pointed out by Zaletel et al. ultracold polar molecules or atoms in optical lattices are another candidate for implementing conformal cooling. These systems are commonly used to perform analog quantum simulation of the Fermi-Hubbard model which is widely believed to offer insights into high-temperature superconductivity[21]. Entropy extraction remains an elusive challenge limiting explorations of the low-energy physics[26]. Spatially modifying the magnitude of the Hamiltonian may be achieved by modulating the density of particles in the bath[90] or by appropriately changing the optical potentials[36]. While both Zaletel et al. and Kuzmin et al. have been successful in cooling this model using both adiabatic and diabatic methods, both studies used relatively low-temperature initial states.

Trapped ions are another natural platform to consider conformal cooling for two reasons: their long-range interactions proportional to R^{-2} for the interparticle distance R and their finite-temperature phase transition between a ferromagnetic and paramagnetic phase[61]. The Hamiltonian can be described by a long-range version of the transverse-field Ising model

$$\mathcal{H}_{\mathrm{TI}} = -J\sum_{i<j}\frac{1}{r_{ij}^2}\hat{\sigma}_i^z\hat{\sigma}_j^z - \Omega\sum_i \hat{\sigma}_i^x \tag{3.1}$$

where r_{ij} is the distance between the ions at sites i and j. Schuckert et al. recently used the algorithm proposed by Lu et al. to study the finite-temperature transition that this model exhibits. Given that the required temperatures are on the order of $T/J \sim 1$, both conformal cooling and the adiabatic preparation of TFD states may be useful alternatives for studying this transition using analog quantum simulators.

Alternatives Approaches to Cooling in Analog Quantum Simulators

Finally, we want to provide an outlook over alternatives to our cooling proposals that may be suited for analog quantum simulation in Rydberg atom tweezer arrays. The first comprises a generalized approach similar to *adiabatic demagnetization* in solid-state systems[47]. Here, a spin system has controlled interactions with a thermal bath and is subjected to an external magnetic field. This can be used to polarize the spin ensemble and reach temperatures in the μK range. In the context of programmable quantum simulation, Matthies et al. consider a setup where one has N interacting qubits* in a random state with an arbitrary Hamiltonian and N noninteracting spin-$\frac{1}{2}$ particles, which are fully polarized and act as the bath. There is a time-dependent interaction between each qubit and a corresponding bath spin with a time-dependent magnetic field acting on the bath spins. The refrigeration cycle works by adiabatically turning on the qubit-spin interaction and slowly reducing the magnetic field at the same time. Therefore the system and bath remain in thermal equilibrium, resulting in an energy flow from the system to the bath. At the end, each bath spin is measured and reset to its original polarization. This was demonstrated for a one-dimensional mixed-field Ising model by Matthies et al.. While this model may be naturally implemented on a Rydberg atom array, the requirements for adiabatic evolution and noninteracting degrees of freedom in the bath may be difficult to realize.

Another approach is *sympathetic cooling*, wherein the system degrees of freedom couple coherently to bath degrees of freedom that are dissipatively driven to continuously extract energy from the bath[56]. In the Rydberg atom tweezer array that we discussed so far, engineering a dissipatively driven subsystem while maintaining coherent interactions with the system may be challenging. As pointed out by Singh et al. dual-species neutral atom tweezer arrays may be a natural candidate for implementing sympathetic cooling. Here, two atomic species, e.g., rubidium and ce-

*A synonym for a two-level system, more commonly used in information theory contexts.

sium, are trapped in the tweezer array and can be individually addressed due to the different atomic level structures. This has the crucial advantage that one species can be optically driven but not the other—all the while maintaining strong Rydberg interactions between them. Following the proposal of Raghunandan et al., it would be interesting to investigate how this approach works in the case of many interacting degrees of freedom in the bath. An intriguing advantage is that this approach does not necessarily rely on thermalization properties of the model or adiabatic methods, in contrast to the previously discussed approaches. Given the recent demonstration of a dual-species tweezer array by Singh et al., sympathetic cooling is a promising approach for preparing low-energy states on a programmable quantum simulator.

A

Numerical Techniques

Quantum many-body systems are notoriously hard to solve, both analytically and numerically. On the one hand, it is well known that many models—including the model presented in Eq. (1.6)—are generally not exactly solvable, leaving numerical simulation as the only viable option. On the other hand, the exponential growth of the Hilbert space of a system with the number of constituents notoriously complicates this task for classical computing. However, small systems up to roughly 16 particles can be studied exactly via exact diagonalization of the Hamiltonian. For larger systems,

there are alternatives using tensor networks for approximate representations of the full quantum state. We note that there is a plethora of other methods, including Monte Carlo algorithms, approaches to sparse matrix problems and neural networks.

In this section we will give an overview over the computational approaches used in the main body. We will first discuss matrix product states (MPS) which are a particularly versatile ansatz for studying 1D quantum many-body problems. After a detailed introduction to familiarize us with the formalism, our focus becomes the specific algorithms that we employed in the scope of this work. This includes a discussion of time evolution using matrix product operators, the density-matrix renormalization group (DMRG) for finding ground states and minimally entangled typical thermal state algorithms which are useful for efficiently sampling expectation values of canonical ensembles. The aim of this work is not to provide in-depth knowledge into each topic, but rather to familiarize the reader with the key concepts. We refer interested readers to more detailed work and reviews at the relevant sections. Lastly we will discuss the specific case of the transverse-field Ising model. We will demonstrate how it can be analytically cast into a quadratic fermionic Hamiltonian that can be solved by exact diagonalization. Crucially this problem reduces to a free-fermion problem, making it tractable for classical computation.

A.1 Matrix Product States

Gaining popularity during the 2000s, matrix product states have since become a staple within the quantum many-body physics community due to their versatility. They are particularly well suited for studying one-dimensional problems, but have also been successfully applied to two-dimensional systems including the observation of continuous symmetry breaking in a 2D dipolar XY model[7]. What makes MPS appealing among other aspects is that they can be efficiently applied to study a wide range of dynamical systems, ground state problems and thermal properties. However MPS al-

gorithms have also sparked some interest outside of physics, e.g., in deep learning where similar ideas were employed to dynamically compress the layers of a neural network[70]. The following section introduces the key concepts behind matrix product states and follows the work of Schollwöck.

MPS make use of a rather efficient way of representing quantum states: the Schmidt decomposition. Given two quantum systems A, B and their state $|\psi_{AB}\rangle$ the Schmidt decomposition is given by

$$|\psi_{AB}\rangle = \sum_{\alpha=1}^{\chi} \lambda_\alpha |\alpha_A, \alpha_B\rangle, \tag{A.1}$$

where χ is the bond dimension, $\lambda_\alpha \in \mathbb{R}$ are the Schmidt values and $|\alpha_{A,B}\rangle$ are a distinct set of orthonormal states on A and B. The Schmidt values fulfill $\sum_\alpha \lambda_\alpha^2 = \langle\psi_{AB}|\psi_{AB}\rangle$—from now on we assume the state to be normalized, i.e., $\langle\psi_{AB}|\psi_{AB}\rangle = 1$. The bond dimension is equal to the minimum local Hilbert space dimension of A and B. We use $|\alpha_A, \alpha_B\rangle$ as shorthand notation for $|\alpha_A\rangle \otimes |\alpha_B\rangle$. As an illustrative example, consider the singlet state $\frac{1}{\sqrt{2}}(|01\rangle - |10\rangle)$ on two qubits. This state has the Schmidt values $\pm\frac{1}{\sqrt{2}}$ and the orthonormal Schmidt states $|0,1\rangle$ and $|1,0\rangle$.

The Schmidt decomposition effectively corresponds to a singular value decomposition (SVD). Given a complex $m \times n$ matrix $M \in \mathbb{C}^{m\times n}$ it iteratively constructs unitary matrices $U \in \mathbb{C}^{m\times m}$ and $V \in \mathbb{C}^{n\times n}$ as well as a real diagonal matrix $\Lambda \in \mathbb{R}^{m\times n}$ such that $M = U\Lambda V^\dagger$, where $V^\dagger$ is the Hermitian transpose of V. The trick to obtaining a matrix product state is by successively applying Schmidt decomposition and introducing the matrices $A_\alpha^{[A],j_A} = \langle j_A|\alpha_A\rangle$ and $A_\alpha^{[B],j_B} = \langle j_B|\alpha_B\rangle$, where $|j_{A,B}\rangle$ are a canonically chosen orthonormal basis, e.g., $\{|\uparrow\rangle, |\downarrow\rangle\}$ for spin-$\frac{1}{2}$ particle or $\{|\mathrm{g}\rangle, |\mathrm{r}\rangle\}$ for the Rydberg atom. This gives the equivalent representation

$$|\psi_{AB}\rangle = \sum_{j_A,j_B} \sum_{\alpha=1}^{\chi} A_\alpha^{[A],j_A} A_\alpha^{[B],j_B} \lambda_\alpha |j_A, j_B\rangle.$$

Keeping in mind that the sum over λ_α can be absorbed into one of the $A_\alpha^{[A,B],j_{A,B}}$ matrices and the sum over α replaced with a matrix product, resulting in the final form of the MPS

$$|\psi_{AB}\rangle = \sum_{j_A j_B} A^{[A],j_A} A^{[B],j_B} |j_A, j_B\rangle.$$

Note that the matrices $A^{[A],j_A}, A^{[B],j_B}$ here have just one index each ($\alpha = 1, \ldots, \chi$) meaning that they have one trivial dimension. As we will see below for larger systems, this is only true at the edge—the rest have two nontrivial dimension in general. For the singlet state, performing this trivially gives the four matrices

$$A^{[A],0} = \begin{pmatrix} 1 & 0 \end{pmatrix}, \; A^{[A],1} = \begin{pmatrix} 0 & 1 \end{pmatrix}$$
$$A^{[B],0} = \begin{pmatrix} 0 \\ -\frac{1}{\sqrt{2}} \end{pmatrix}, \; A^{[B],1} = \begin{pmatrix} \frac{1}{\sqrt{2}} \\ 0 \end{pmatrix}.$$

The true computational power of MPS comes by considering chains of d-level systems: let N be the length of the chain, d the local Hilbert space dimension of the constituents and $|\psi\rangle$ a state on the combined Hilbert space. We start with Eq. (A.1) where we consider the bipartition at the first bond such that A is the Hilbert space of the first site and B the one of the combined $N-1$ remaining sites:

$$|\psi\rangle = \sum_{\alpha_1=1}^{d} \lambda_{\alpha_1} |\alpha_{1,\mathrm{L}}, \alpha_{1,\mathrm{R}}\rangle.$$

We note that $|\alpha_{n,\mathrm{L}}\rangle$ and $|\alpha_{n,\mathrm{R}}\rangle$ refer to the Schmidt states left and right of the bond n between sites n and $n+1$. The first step is again analogous to the simple case described above by defining $A_{\alpha_1}^{[1],j_1} =$

$\langle j_1|\alpha_{1,\mathrm{L}}\rangle$ resulting in the state

$$|\psi\rangle = \sum_{j_1=1}^{d}\sum_{\alpha_1=1}^{\chi_1} A^{[1],j_1}_{\alpha_1}\lambda_{\alpha_1}|j_1,\alpha_{1,\mathrm{R}}\rangle.$$

Now the iterative procedure continues by decomposing the state of the second bond using an SVD into

$$|\psi\rangle = \sum_{\alpha_2=1}^{\chi_2}\lambda_{\alpha_2}|\alpha_{2,\mathrm{L}},\alpha_{2,\mathrm{R}}\rangle,$$

where the bond dimension χ_2 is the dimension of the combined Hilbert space of sites 1 and 2, i.e., d^2. We now see that we can introduce $A^{[2],j_2}_{\alpha_1,\alpha_2}$ such that

$$|\alpha_{2,\mathrm{L}}\rangle = \sum_{\alpha_1=1}^{\chi_1}\sum_{j_2=1}^{d}|\alpha_{1,\mathrm{L}},j_2\rangle\langle\alpha_{1,\mathrm{L}},j_2|\alpha_{2,\mathrm{L}}\rangle = \sum_{\alpha_1}^{\chi_1}\sum_{j_2=1}^{d}A^{[2],j_2}_{\alpha_1,\alpha_2}|\alpha_{1,\mathrm{L}},j_2\rangle.$$

Using this result we find

$$|\psi\rangle = \sum_{\alpha_1=1}^{\chi_1}\sum_{\alpha_2=1}^{\chi_2}\sum_{j_1,j_2=1}^{d}A^{[1],j_1}_{\alpha_1}A^{[2],j_2}_{\alpha_1,\alpha_2}\lambda_{\alpha_2}|j_1,j_2,\alpha_{2,\mathrm{R}}\rangle.$$

By defining $A^{[n],j_n}_{\alpha_{n-1},\alpha_n} = \langle\alpha_{n-1,\mathrm{L}},j_n|\alpha_{n,\mathrm{L}}\rangle$ $(N > n > 1)$ we can iteratively decompose the quantum state as follows

$$\begin{aligned}|\psi\rangle &= \sum_{\alpha_1=1}^{\chi_1}\sum_{\alpha_2=1}^{\chi_2}\cdots\sum_{\alpha_{N-1}=1}^{\chi_N}\sum_{j_1,j_2,\ldots j_N=1}^{d}A^{[1],j_1}_{\alpha_1}A^{[2],j_2}_{\alpha_1,\alpha_2}\ldots A^{[N],j_N}_{\alpha_{N-1}}\lambda_{\alpha_{N-1}}|j_1,j_2,\ldots,j_N\rangle\\ &= \sum_{j_1,j_2,\ldots,j_N=1}^{d}A^{[1],j_1}A^{[2],j_2}\ldots A^{[N],j_N}|j_1,j_2,\ldots,j_N\rangle. \qquad \text{(A.2)}\end{aligned}$$

The indices $j_{1,\ldots,N}$ are commonly referred to as the *physical* indices with $\alpha_{1,\ldots,N-1}$ being the *vir-*

tual indices. We replaced the summation over the virtual indices in Eq. (A.2) with matrix products in the second line and also absorbed the trivial, diagonal matrix $\lambda_{\alpha_{N-1}} = \lambda_{\alpha_{N-1},\alpha_{N-1}}$ into $A^{[N],j_{N-1}}$. We note that the first and last matrix $A^{[1],j_1}, A^{[N],j_N}$ only depend on one virtual index while all other depend on two in the case of open boundary conditions. For periodic boundary conditions, they also have the virtual indices α_N, α_1 and α_{N-1}, α_N which effectively corresponds to taking the trace over the matrix product in Eq. (A.2). The matrices $A^{[k],j_k}$ can be represented in graphical notation as a tensor with three *legs* corresponds to the virtual and physical indices.

The decomposition that we proposed also holds for more general matrices $A^{[n],j_n}$. It turns out that there is a particularly useful construction: the *canonical form* which is given by

$$|\psi\rangle = \sum_{j_1,j_2,\ldots,j_N=1}^{d} \Lambda_0 M^{[1],j_1} \Lambda_1 M^{[2],j_2} \Lambda_2 \ldots \Lambda_{N-1} M^{[N],j_N} \Lambda_N |j_1, j_2, \ldots, j_N\rangle. \tag{A.3}$$

The Λ_n are diagonal, real matrices with χ_n entries; we note that $\Lambda_0 = \Lambda_N = (1)$. We note that Eq. (A.2) is in canonical form up to identification $\Lambda_n = \lambda_n$ and $M^{[n],j_n} = (\lambda_{n-1})^{-1} A^{[n],j_n}$, which can be efficiently computed given that λ_n is diagonal. Furthermore, it is useful to define the matrices

$$L^{[n],j_n} = \Lambda_{n-1} M^{[n],j_n} \text{ and} \tag{A.4}$$

$$R^{[n],j_n} = M^{[n],j_n} \Lambda_n. \tag{A.5}$$

Eqs. (A.4) and (A.5) are commonly referred to as the *left-* and *right*-canonical form. This naming convention becomes apparent when considering that

$$|\alpha_{n+1,\mathrm{L}}\rangle = \sum_{\alpha_n=1}^{\chi_n} \sum_{j_{n+1}=1}^{d} L^{[n],j_n}_{\alpha_n,\alpha_{n+1}} |\alpha_{n,\mathrm{L}}, j_n\rangle$$

$$|\alpha_{n,\mathrm{R}}\rangle = \sum_{\alpha_{n+1}=1}^{\chi_{n+1}} \sum_{j_n=1}^{d} R^{[n],j_n}_{\alpha_n,\alpha_{n+1}} |j_n, \alpha_{n+1,\mathrm{R}}\rangle.$$

This means that the left-canonical form corresponds to the Schmidt states left of bond n and the right-canonical form to those to the right of bond n. While the iterative procedure that we introduced above results in the left-canonical form, we obtain an MPS in right-canonical form via successive SVDs starting at the right end. The mixed form corresponds to an MPS which is in left-canonical form left of site i and in right canonical form to its right. The matrix on site i is given by $\Theta^{[i],j_i} = \Lambda_{i-1} M^{[i],j_i} \Lambda_i$. This is useful as the state of the combined system can be written as

$$|\psi\rangle = \sum_{\alpha_{i-1}=1}^{\chi_{i-1}} \sum_{\alpha_i=1}^{\chi_i} \sum_{j_i=1}^{d} \Theta^{[i],j_i}_{\alpha_{i-1},\alpha_i} |\alpha_{i-1,\mathrm{L}}, j_i, \alpha_{i,\mathrm{R}}\rangle. \tag{A.6}$$

After doing some basic linear algebra we find that the expectation of any local operator $\hat{\mathcal{O}}_i$ becomes

$$\langle\psi|\hat{\mathcal{O}}_i|\psi\rangle = \sum_{\alpha_{i-1}=1}^{\chi_{i-1}} \sum_{\alpha_i=1}^{\chi_i} \sum_{j_i,j_i^*=1}^{d} \Theta^{[i],j_i}_{\alpha_{i-1},\alpha_i} \left(\Theta^{[i],j_i^*}_{\alpha_{i-1},\alpha_i}\right)^* \langle j_i^*|\hat{\mathcal{O}}_i|j_i\rangle$$

which depends solely on $\Theta^{[i],j_i}$ and does not require knowledge of the other matrices of the MPS. This makes it much more computationally tractible. Similar results can be shown for multi-site operators, where only the matrices between the farthest apart sites are needed for expectation values. Outside the efficient computation of expectation values the canonical forms are helpful for applying unitaries. Many of the algorithms that we will discuss in later section make use of the decomposition in Eq. (A.6) by only changing local matrix on one site or one bond at a time. This allows for efficient iterative procedures. The computational complexity of this process is $\mathcal{O}(N \cdot d^3 \cdot \chi_{\max}^3)$ using the big $\mathcal{O}$ notation where $\chi_{\max}$ is the maximum bond dimension.

It is important to point out that this decomposition does not circumvent the problem of the

exponentially large Hilbert space because the bond dimensions

$$\chi_n = \begin{cases} d^n, & \text{for } n \leq \lfloor \frac{N}{2} \rfloor \\ d^{N-n} & \text{for } n > \lfloor \frac{N}{2} \rfloor \end{cases}$$

still scale exponentially in the system size N making it inefficient to write down all coefficients for large systems. However it is often not necessary to write down *all* coefficients—instead Schmidt values below a certain threshold ε can be discarded in practice*. For example ground states of one-dimensional, gapped Hamiltonians with a finite range of interactions can be approximated with an MPS using a bond dimension that scales polynomially in N instead of exponentially[24,38].

To understand where this comes from, it is useful to take a step back and discuss how we measure the complexity of a state. One way of doing this is using the entanglement entropy S for a bipartition of the system into two subsystems A and B. It is defined as the von Neumann entropy

$$S = -\mathrm{Tr}\left[\rho_A \log\left(\rho_A\right)\right]$$

of the reduced density matrix ρ_A of A. Using the Schmidt decomposition, we equivalently find

$$S = -\sum_\alpha \lambda_\alpha^2 \log\left(\lambda_\alpha^2\right)$$

with the Schmidt values λ_α.

Using the convention $0 \cdot \log(0) = 0$ we see that if A and B are in a product state $|\psi_{AB}\rangle = |\varphi_A\rangle \otimes |\theta_B\rangle$, then their entanglement entropy is vanishing. Otherwise it is larger than zero and we call them entangled. If two systems are entangled, they are also correlated, meaning that $\langle \hat{\mathcal{O}}_A \hat{\mathcal{O}}_B \rangle - \langle \hat{\mathcal{O}}_A \rangle \langle \hat{\mathcal{O}}_B \rangle \neq 0$ for some operators $\hat{\mathcal{O}}_{A,B}$.

*In general we choose $\varepsilon = 10^{-10}$.

By discarding Schmidt values, the resulting MPS has a lower entanglement entropy. Therefore it is important that the Schmidt values decay sufficiently fast. In practice this happens for *area law* states. For these states the entropy S scales with the surface area $|\partial A|$ of the region A that is being considered. In contrast typical states, i.e., states drawn from a Haar measure, obey a volume law, $S \propto |A|$, making them intractible for efficient classical simulation. The area law originates in the finite correlation length ξ of the state, meaning that a sufficiently large region ($l_A \gg \xi$) is only entangled with the rest of the system at its boundary. In one dimension this means that the entanglement entropy is constant for $N > \xi$ such that we can approximate the state using an MPS efficiently. This is in fact a numerical challenge in Sec. 2.2.

Ground states of 1D gapped local Hamiltonians are not the only states of interest in the exponentially large zoo of states in the Hilbert space that can be well approximated using MPS with a fixed bond dimension. In practice this includes low-entanglement states and those which have only a few dominant singular values—this holds for both real and imaginary time evolution of product states for sufficiently short times. This observation is crucial for many of the algorithms that we will discuss in the following section.

A.1.1 Matrix Product Operators

The matrix product representation is not unique to quantum states but can also be applied to operators. For any operator $\hat{O}$ we can find matrices $W^{[k],i_k,j_k} \in \mathbb{C}^{d\times d}$ such that

$$\hat{O} = \sum_{\substack{i_1,\ldots,i_N \\ j_1,\ldots,j_N}} v_{\mathrm{L}} W^{[1],i_1,j_1} W^{[2],i_2,j_2} \ldots W^{[N-1],i_{N-1},j_{N-1}} W^{[N],i_N,j_N} v_{\mathrm{R}} |i_1,\ldots,i_N\rangle\langle j_1,\ldots,j_N|, \quad \text{(A.7)}$$

where v_{L} and v_{R} are auxiliary vectors at each end of the chain and $|i_k\rangle$, $|j_k\rangle$ are the basis states on site k. In graphical notation, the matrices $W^{[k],i_k,j_k}$ can be represented as tensors with four legs

corresponding to the two physical indices i_k, j_k and the two virtual indices β_k, β_{k+1}. For models with short-range interactions there is an efficient way of constructing the matrix product operator (MPO) representation for the Hamiltonian. For long-range models the bond dimension grows significantly which can be a limiting factor.

A.1.2 Time-evolution of Matrix Product States

As we are concerned with dynamics of quantum chains in this work, time evolution is a central topic of interest. While a plethora of methods have been developed over the years, we give a general overview in this section with a focus on the MPO W^{II} method, which we employ for all of our numerics. For a detailed review we refer to Paeckel et al..

In general we are interested in applying the unitary time-evolution operator

$$U(t) = \mathrm{e}^{-\mathrm{i}Ht}$$

which dictates the evolution under the time-independent Schrödinger equation for a Hamiltonian H up to time t. This means that $|\psi(t)\rangle = U(t)|\psi(0)\rangle$ for any initial state $|\psi(0)\rangle$. A significant problem is that this operator is dense, i.e., it requires an exponential number of coefficients in the system size N and acts highly nonlocal. A good first step is to consider splitting the time evolution into a series of small steps of size δt such that

$$U(t) = \left(\mathrm{e}^{-\mathrm{i}H\,\delta t}\right)^n = (U(\delta t))^n$$

where $n \cdot \delta t = t$. In general it is much more tractable to find a good approximation for $U(\delta t)$ and apply it to a state n times than to perform $U(t)$. For short-range Hamiltonians, in particular nearest-neighbor models, the time-evolving block decimation (TEBD) is a good method for approximating

this operator. To illustrate this, consider the following nearest-neighbor Hamiltonian

$$H = \sum_i \hat{h}_{i,i+1} = \sum_{i\,\text{even}} \hat{h}_{i,i+1} + \sum_{i\,\text{odd}} \hat{h}_{i,i+1} = H_{\text{even}} + H_{\text{odd}} \tag{A.8}$$

which we decompose into a series of terms acting only on even and odd bonds. We find that

$$\begin{aligned} U(\delta t) &= \mathrm{e}^{-\mathrm{i}H\,\delta t} = \mathrm{e}^{-\mathrm{i}(H_{\text{even}}+H_{\text{odd}})\delta t} \approx \mathrm{e}^{-\mathrm{i}H_{\text{even}}\delta t}\mathrm{e}^{-\mathrm{i}H_{\text{odd}}\delta t}\mathrm{e}^{-\mathrm{i}[H_{\text{even}},H_{\text{odd}}]\delta^2} \\ &\approx \mathrm{e}^{-\mathrm{i}H_{\text{even}}\delta t}\mathrm{e}^{-\mathrm{i}H_{\text{odd}}\delta t} + \mathcal{O}\left(\delta t^2\right) \end{aligned}$$

which is known as the Trotter-Suzuki decomposition where we used the Baker-Campbell-Hausdorff formula in the first line and introduced the commutator $[H_{\text{even}}, H_{\text{odd}}] = H_{\text{even}}H_{\text{odd}} - H_{\text{odd}}H_{\text{even}}$. Since all terms in H_{even} commute with one another, we can simply exponentiate them individually

$$\mathrm{e}^{-\mathrm{i}H_{\text{even}}\delta t} = \prod_{i\,\text{even}} \mathrm{e}^{-\mathrm{i}\hat{h}_{i,i+1}\delta t}.$$

The same also holds for H_{odd} such that it just simplifies to applying $\exp(-\mathrm{i}h_{i,i+1}\delta t)$ on all even bonds, performing SVDs on all bonds and then doing the same for all odd bonds. We note that terms acting only on a single site at once can easily be accommodated. Extensions to longer-range models exist but rely on a growing number of swap gates that swap sites i and $i+1$ to turn a next-nearest into a nearest-neighbor interaction and then swap back.

A key advantage of TEBD is that it can be parallelized as every term in $U(\delta t)$ only acts on two sites at once. There are also generalization to reduce the error from $\mathcal{O}(\delta t^2)$ to $\mathcal{O}(\delta t^5)$ at the cost of more unitary matrices to apply per time step.

A.1.3 MPO W^{II} Method

For systems with sufficiently long-range interactions, e.g., trapped Rydberg atoms or ions, and two-dimensional systems, TEBD is generally inefficient so new methods are needed. The MPO W^{II} method was developed by Zaletel et al. to address this problem by exploiting the MPO representation of the Hamiltonian. We consider a Hamiltonian

$$H = \sum_j H_j,$$

where H_j are local operators that act only on a finite range of sites around site j. The traditional Euler approximation for the time-evolution operator gives

$$U(\delta t) = \sum_n \frac{(-\mathrm{i}\,\delta t)}{n!} H^n \approx 1 - \mathrm{i}\,\delta t \sum_j H_j + \mathcal{O}(\delta t^2)$$

with the factorial $n! = \prod_{m=1}^{n} m$. There are on the order of N^2 terms in the $\mathcal{O}(\delta t^2)$ contribution from H^2 resulting in an error per site of $\mathcal{O}(N\,\delta t^2)$. This makes studying large system sizes significantly more difficult. Zaletel et al. propose an improved Euler step

$$U(\delta t) \approx 1 - \mathrm{i}\,\delta t \sum_j H_j - \delta t^2 \sum_{j,k\in M} H_j H_k + \mathcal{O}(N\delta t^2) + \mathcal{O}(\delta t^3) \equiv U^{\mathrm{II}}(\delta t) \tag{A.9}$$

where M is the set of sites j, k such that H_j and H_k act at most on one common site, e.g., terms like $\hat{n}_j \otimes \hat{n}_k \hat{\sigma}^{\mathrm{x}}_k$ are included while $\hat{n}_j \hat{n}_j \otimes \hat{n}_k \hat{n}_k$ is not in Eq. (1.6). While this has still an error $\mathcal{O}(\delta t^2)$, the number of terms that are not included is on the order of N, leading to an error that is constant per site. A main advantage is that the operator $U^{\mathrm{II}}(\delta t)$ can be approximated by an efficient MPO representation, $W^{\mathrm{II}}(\delta t)$, making it easy to apply to an MPS. The error of $W^{\mathrm{II}}(\delta t)$ is $\mathcal{O}(\delta t^3)$. This is comparable to a straightforward implementation of a higher-order Trotter scheme for the TEBD

algorithm previously discussed. There are details, e.g., on the construction of $W^{\mathrm{II}}(\delta t)$ not included here—we refer the interested reader to the works of Zaletel et al. and Paeckel et al. for more thorough reviews of the topic.

While these methods were discussed in the context of real time evolution, i.e., $t \in \mathbb{R}$, this can be straightforwardly generalized for imaginary time evolution where t is a negative imaginary number. Under this condition $U(t)$ is no longer unitary and the norm of the state is not preserved by the transformation. This can be circumvented by explicitly normalizing the state. This is important when dealing with imaginary time evolution which we employ to calculate thermal expectation values.

A.1.4 Density-matrix Renormalization Group

Besides dynamic properties of the quantum chains, we are also interested in their low-energy physics, i.e., the ground state. A powerful tool for these systems is the *density-matrix renormalization group* (DMRG) which was first introduced by White. It is a variational method that iteratively performs updates to the local matrices $A^{[k],i_k}$ in Eq. (A.2) to minimize

$$\langle\psi|H|\psi\rangle,$$

i.e., the energy of the state $|\psi\rangle$. It has been very successful in the context of one-dimensional, local Hamiltonians with a finite gap.

Assume that $|\psi\rangle$ is in mixed canonical form at site i such that

$$|\psi\rangle = \sum_{j_1,\dots j_N} L^{[1],j_1} \dots L^{[i-1],j_{i-1}} \Lambda_i R^{[i],j_i} \dots R^{[N],j_N} \tag{A.10}$$

where $L^{[k],j_k}$ are the left-canonical matrices at site $k = 1, \dots, i-1$ and $R^{[k],j_k}$ are the right-canonical

matrices at site $k = i, \ldots, N$. We then define the two site tensor

$$\Theta^{j_i,j_{i+1}}_{\alpha_i,\alpha_{i+2}} = \sum_{\alpha'_i,\alpha_{i+1}} \Lambda_{\alpha_i,\alpha'_i} R^{[i],j_i}_{\alpha'_i,\alpha_{i+1}} R^{[i+1],j_{i+1}}_{\alpha_{i+1},\alpha_{i+2}}$$

which defines the reduced density matrix on sites $i, i+1$ as

$$\left(\rho_{i,i+1}\right)^{j_i j_{i+1} j'_i j'_{i+1}}_{\alpha_i,\alpha_{i+2},\alpha'_i,\alpha'_{i+2}} = \sum_{\alpha_i,\alpha_{i+2}} \Theta^{j_i,j_{i+1}}_{\alpha_i,\alpha_{i+2}} \left(\Theta^{j'_i,j'_{i+1}}_{\alpha_i,\alpha_{i+2}}\right)^* .$$

Next we define the effective Hamiltonian acting on this reduced density matrix using the MPO representation of the Hamiltonian

$$\begin{aligned}
&\left(H_{\text{eff}}\right)^{j_i j_{i+1} j'_i j'_{i+1}}_{\alpha_i,\alpha_{i+2},\alpha'_i,\alpha'_{i+2}} = \\
&\sum_{\substack{j_1,\ldots,j_{i-1},j_{i+2},\ldots j_N \\ j'_1,\ldots j'_{i-1},j'_{i+2},\ldots,j'_N}} \sum_{\substack{\alpha_1,\ldots,\alpha_{i-1},\alpha_{i+3},\ldots,\alpha_N \\ \alpha'_1,\ldots,\alpha'_{i-1},\alpha'_{i+3},\ldots,\alpha'_N}} \sum_{\beta_1,\ldots,\beta_{N+1}} \left(L^{[1],j_1}_{\alpha_1} L^{[2],j_2}_{\alpha_1,\alpha_2} \ldots L^{[i-1],j_{i-1}}_{\alpha_{i-1},\alpha_i} R^{[i+2],j_{i+2}}_{\alpha_{i+2},\alpha_{i+3}} \ldots R^{[N-1],j_{N-1}}_{\alpha_{N-1},\alpha_N} R^{[N],j_N}_{\alpha_N}\right) \\
&\cdot \left(v_{\text{L},\beta_1} W^{[1],j_1,j'_1}_{\beta_1,\beta_2} \ldots W^{[i],j_i,j'_i}_{\beta_i,\beta_{i+1}} \ldots W^{[i+1],j_{i+1},j'_{i+1}}_{\beta_{i+1},\beta_{i+2}} \ldots\ldots W^{[N],j_N,j'_N}_{\beta_N,\beta_{N+1}}\right) \\
&\cdot \left(L^{[1],j'_1}_{\alpha'_1} L^{[2],j'_2}_{\alpha'_1,\alpha'_2} \ldots L^{[i-1],j'_{i-1}}_{\alpha'_{i-1},\alpha'_i} R^{[i+2],j'_{i+2}}_{\alpha'_{i+2},\alpha'_{i+3}} \ldots R^{[N-1],j'_{N-1}}_{\alpha'_{N-1},\alpha'_N} R^{[N],j'_N}_{\alpha'_N}\right)^* .
\end{aligned} \tag{A.11}$$

DMRG performs an update on that state of sites i and $i+1$ by reshaping H_{eff} into a square matrix with indices $(j_i, j_{i+1}, \alpha_i, \alpha_{i+2})$ and $(j'_i, j'_{i+1}, \alpha'_i, \alpha'_{i+2})$. From the construction of this effective Hamiltonian one can see that the energy expectation value of the Hamiltonian is

$$\langle\psi|H|\psi\rangle = \text{Tr}\left(\rho_{i,i+1} H_{\text{eff}}\right)$$

per performing the necessary tensor contractions. The optimization step of DMRG then suggests finding the $\rho_{i,i+1}$ that minimizes the energy, i.e., the ground state of H_{eff} which can be found ef-

ficiently using exact diagonalization or Lanczos methods. The resulting vector corresponds to an updated $\Theta^{j_i j_{i+1}}_{\alpha_i,\alpha_{i+2}}$ which can be split into the single-site tensors using SVDs. DMRG performs *sweeps* across the chain wherein the two-site tensors are iteratively optimized from site to site to minimize the energy of the state $|\psi\rangle$ in the hopes of converging to the ground state. We note that DMRG can also be used to find low-energy excited states by projecting into the Hilbert space orthogonal to the ground state.

While this procedure has been proven useful, there are some limitations: First the computational complexity is limited by the size of H_{eff} which is a $d^2\chi^2 \times d^2 \times \chi^2$ matrix. For $d = 2$ and a reasonable estimate for the bond dimension $\chi \sim 1000$, we find $\dim(H_{\text{eff}}) = 4 \times 10^6$. Second the updates on the state are only performed locally on sites i and $i+1$ at a time. This can limit long-range entanglement and correlations such that the state only converges to a local minimum, i.e., not the true ground state of H. This is especially important in the context of critical and near-critical ground states which exhibit long-range entanglement and divergent correlation lengths. A method to prevent this limitation is to introduce small perturbations to the wavefunction for the first few sweeps to avoid convergence to a local minimum. In terms of numerical convergence, it is also noteworthy that sweeps are performed until the energy has converged up to an error of $\delta E = 10^{-8}$ with regard to the maximum bond dimension of the MPS. For small gapped Hamiltonians, we found good convergence with 50 sweeps. For the chains of size $L = 2 \times 256 = 512$ in Sec. 2.2 we needed up to 150 sweeps.

A.1.5 Minimally Entangled Typical Thermal States

In the previous two sections we have discussed methods to study dynamical and low-energy properties of the Hamiltonian. While the approach for performing real time evolution technically also works for imaginary time evolution by choosing a negative imaginary time step, this is in practice

limited to short time scales, i.e., the high-temperature regime. This is because the Gibbs state

$$\rho_\beta = \frac{\exp\left(-\beta H\right)}{\mathcal{Z}}$$

is generally a dense matrix for $\beta > 0$, i.e., we need an exponential number of coefficients in the number of constituents to represent the state for sufficiently large $\beta > 0$. $\mathcal{Z} = \mathrm{Tr}\left[\exp\left(-\beta H\right)\right]$ is the partition sum. However if one is only interested in expectation values of that state

$$\langle \hat{O} \rangle_\beta = \mathrm{Tr}\left(\rho_\beta \hat{O}\right)$$

there are efficient sampling methods to approximate this value. One such approach are based on *minimally entangled typical thermal states* (METTS) which were first introduced by Stoudenmire & White. Starting from the expectation value that we want to estimate, we find

$$\begin{aligned} \langle \hat{O} \rangle_\beta &= \frac{1}{\mathcal{Z}} \sum_i \langle i | \mathrm{e}^{-\beta H/2} \hat{O} \mathrm{e}^{-\beta H/2} | i \rangle \\ &= \frac{1}{\mathcal{Z}} \sum_i p_i \langle \varphi_i | \hat{O} | \varphi_i \rangle \end{aligned} \tag{A.12}$$

where $\{|i\rangle\}$ are a complete basis and we define

$$|\varphi_i\rangle = \frac{1}{\sqrt{p_i}} \mathrm{e}^{-\beta H/2} |i\rangle$$

with $p_i = \langle i | \mathrm{e}^{-\beta H} | i \rangle$. By sampling $|\varphi_i\rangle$ with probability $p_i/\mathcal{Z}$ we can approximate $\langle \hat{O} \rangle_\beta$. While the choice for the basis $|i\rangle$ is not unique, the computational basis is a natural choice because they are not entangled and are expected to produce states $|\psi_i\rangle$ with low entanglement for small β. It is also noteworthy that the $\{|\varphi_i\rangle\}$ resemble typical states for this choice: at high temperatures they behave classical and at low temperatures they can exhibit spontaneous symmetry breaking, in line with the

expected behavior of the Gibbs state. This provides an intuitive explanation for the name minimally entangled typical thermal states.

The sampling algorithm is a random walk through the set of METTS as introduced by Stoudenmire & White:

1. Choose a (random) computational basis state $|i\rangle$.
2. Compute the corresponding METTS $|\varphi_i\rangle = \mathrm{e}^{-\beta H/2}|i\rangle/\sqrt{p_i}$.
3. Calculate $\langle\varphi_i|\hat{O}|\varphi_i\rangle$.
4. Collapse $|\varphi_i\rangle$ to a new state in the computational basis $|j\rangle$ with probability $p(i \to j) = |\langle j|\varphi_i\rangle|^2$ and return to step 2.

This procedure ensures that the distribution samples with the correct probability $p_i/\mathcal{Z}$ because the probability to obtain $|j\rangle$ is

$$\begin{aligned}\sum_i \frac{p_i}{\mathcal{Z}} p(i \to j) = \sum_i \frac{p_i}{\mathcal{Z}} |\langle j|\varphi_i\rangle|^2 &= \sum_i \frac{p_i}{\mathcal{Z}} \frac{|\langle j|\mathrm{e}^{-\beta H/2}|i\rangle|^2}{p_i} \\ &= \sum_i \frac{\langle j|\mathrm{e}^{-\beta H/2}|i\rangle\langle i|\mathrm{e}^{-\beta H/2}|j\rangle}{\mathcal{Z}} = \frac{\langle j|\mathrm{e}^{-\beta H}|j\rangle}{\mathcal{Z}} = \frac{p_j}{\mathcal{Z}}.\end{aligned}$$

This is a consequence of detailed balance $p(i \to j)/p(j \to i) = p_j/p_i$. Two advantages of the above mentioned sampling algorithm is that every sample is used to estimate $\langle\hat{O}\rangle_\beta$ and that it can be easily parallelized. To perform the imaginary time evolution to go from $|i\rangle$ to $|\varphi_i\rangle$ we use the previously discussed MPO W^{II} method (cf. Sec. A.1.3). The entanglement grows sufficiently slowly for the imaginary time evolution of computational basis states making this algorithm suitable for obtaining correlations for low-temperature Gibbs states in Ch. 2.

As pointed out by Stoudenmire & White the freedom to choose any complete basis for the states $|i\rangle$ can be used to optimize the convergence of this algorithm. It turns out that ergodicity of the

samples can be improved by alternating between two different bases, e.g., the $\hat{\sigma}^z$ and $\hat{\sigma}^x$ eigenstates. Assuming that $|i^z\rangle$ is a state in the z-basis, we collapse $|\varphi_i^z\rangle$ to a state $|j^x\rangle$ in the x-basis and vice versa. This leads to a significant reduction in the autocorrelation time such that expectation values of $|\varphi_i\rangle$ approach thermal values after 5–10 samples in practice. The results in Ch. 2.2 converged for 2000 total samples where we excluded the first 5 samples in each sampling procedure. A downside of this method is that sampling small expectation values requires a larger amount of samples in general—given the exponential decay of correlations for the finite-temperature states that we consider, this is indeed a limitation at sufficiently large temperatures.

Numerical Resources for Matrix Product States

All numerical results in the main body were obtained using matrix product state simulations. Here we want to comment on the numerical resources that were required to obtain the results. We acknowledge and thank the Harvard Odyssey cluster for providing these resources.

In Ch. 1 we mainly used the MPO W^{II} method to simulate quantum chains out of equilibrium. The run times for the simulations with system size $N = 37$ (cf. Figs. 1.4 and 1.5) are roughly 5000 core hours. For $N = 24$ (cf. Fig. 1.6) we needed approximately 1500 core hours to reach the required time scales. This means that generating Fig. 1.6 took 60000 core hours. This estimate comes from the 40 runs, each of which were performed in parallel.

The numerical calculations in Ch. 2 include both a DMRG, the MPO W^{II} method and METTS. The low-energy calculations took up to 1500 core hours to obtain the ground state and gap for $L = 256$—however the run time is significantly lower at smaller system sizes. We note that the chain is a total length of $2L$ due to the ladder configuration. Similarly the imaginary time evolution for the exact TFD state took up to 1000 core hours—this failed to reach the required system sizes however, so we instead turned to METTS to obtain thermal expectation values. The longest METTS simulation took 10000 core hours for $L = 256$ and inverse temperature $\beta = 7.5$. Due to efficient

parallelization we were able to perform 500 sampling procedures in parallel such that the total time was less than two days.

A.2 Free Fermion Mapping for the Transverse-Field Ising Model

While matrix product states have opened new possibilities for studying quantum many-body systems, they are still limited by the inherent growth of entanglement in the system. This is particularly true for nonintegrable models that are generally expected to exhibit ergodic dynamics as we will discuss in App. B. However this is not necessarily the case for integrable models because dynamics reduce to single particles—for a discussion of why that is the case, we refer to the corresponding section in App. B. The work of Surace & Tagliacozzo provides a detailed review of the numerical methods.

The spin-$\frac{1}{2}$ transverse-field Ising model (TFIM) in one dimension is a paradigmatic model that allows studying dynamics for large system sizes and long times because it can be mapped to free, i.e., noninteracting, fermions. We consider the Hamiltonian of a TFIM arranged in a chain of length N

$$\mathcal{H}_{\mathrm{TFIM}} = \sum_{i=1}^{N} \lambda_i \left(J \hat{\sigma}_i^{\mathrm{x}} \otimes \hat{\sigma}_{i+1}^{\mathrm{x}} + \Omega \hat{\sigma}_i^{z} \right) \tag{A.13}$$

where we assume open boundary conditions ($\hat{\sigma}_0^{\mathrm{x}} = \hat{\sigma}_{N+1}^{\mathrm{x}} = 0$) and a spatial modulation $\lambda_i \in [0,1]$ as in Ch. 1. Up to a unitary rotation $U = \prod_i \exp(-\mathrm{i}\pi\hat{\sigma}^{y}/4)$ this can be mapped to a Rydberg atom array for a specific choice of parameters as we discuss in App. C.

The Jordan-Wigner transformation allows a way of solving this model by mapping it to fermions. We introduce the fermionic annihilation and creation operators $\hat{c}_i$ and $\hat{c}_i^{\dagger}$, where † stands for the Hermitian conjugate. These obey the canonical anticommutation relations $\{\hat{c}_i, \hat{c}_j^{\dagger}\} = \delta_{ij}$, $\{\hat{c}_i, \hat{c}_j\} =$

0. Let $\eta_i = \exp(-i\pi \sum_{j<i} \hat{c}_j^\dagger \hat{c}_j)$ be the Jordan-Wigner string and identify the following operators

$$\begin{aligned} \hat{\sigma}_i^+ &= \eta_i \hat{c}_i^\dagger \\ \hat{\sigma}_i^- &= \eta_i \hat{c}_i \end{aligned} \tag{A.14}$$

where $\hat{\sigma}_i^+ = (\hat{\sigma}_i^x + \hat{\sigma}_i^y)/2$ and $\hat{\sigma}_i^- = (\hat{\sigma}_i^x - i\hat{\sigma}_i^y)/2$ are the raising and lowering operators of the spins. Then we can identify

$$\begin{aligned} \hat{\sigma}_i^x &= \hat{\sigma}_i^+ + \hat{\sigma}_i^- = \eta_i(\hat{c}_i + \hat{c}_i^\dagger) \\ \hat{\sigma}_i^z &= 1 - 2\hat{\sigma}_i^+ \hat{\sigma}_i^- = 1 - 2\hat{c}_i^\dagger \hat{c}_i. \end{aligned} \tag{A.15}$$

Plugging this into Eq. (A.13) we get

$$\mathcal{H}_{\text{TFIM}} = \sum_{i=1}^{N} \lambda_i \left(J(\hat{c}_i^\dagger - \hat{c}_i)(\hat{c}_{i+1}^\dagger + \hat{c}_{i+1}) + g(1 - 2\hat{c}_i^\dagger \hat{c}_i) \right)$$

by using $\hat{c}_i \exp(i\pi \hat{c}_i^\dagger \hat{c}_i) = \hat{c}_i(1 - 2\hat{c}_i^\dagger \hat{c}_i) = -\hat{c}_i$ and $\hat{c}_i^\dagger(1 - 2\hat{c}_i^\dagger \hat{c}_i) = -\hat{c}_i^\dagger$ and open boundary conditions ($\hat{c}_{N+1} = \hat{c}_{N+1}^\dagger = 0$). Up to a constant term that can be discarded the Hamiltonian takes the form

$$\begin{aligned} \mathcal{H}_{\text{FF}} &= \sum_{i=1}^{N} \lambda_i \left[\frac{J}{2}(\hat{c}_i^\dagger \hat{c}_{i+1} + \hat{c}_{i+1}^\dagger \hat{c}_i - \hat{c}_{i+1}\hat{c}_i^\dagger - \hat{c}_i \hat{c}_{i+1}^\dagger + \hat{c}_i^\dagger \hat{c}_{i+1}^\dagger - \hat{c}_{i+1}^\dagger + \hat{c}_{i+1}\hat{c}_i - \hat{c}_i \hat{c}_{i+1}) + \Omega(\hat{c}_i \hat{c}_i^\dagger - \hat{c}_i^\dagger \hat{c}_i) \right] \\ &= \sum_{i,j} h_{i,j}(\hat{c}_i^\dagger \hat{c}_i - \hat{c}_i \hat{c}_i^\dagger) + k_{i,j} \hat{c}_i^\dagger \hat{c}_j^\dagger + k_{i,j}^* \hat{c}_i \hat{c}_j, \end{aligned} \tag{A.16}$$

where we introduce the block matrices h and k such that

$$\begin{aligned} h_{i,i} &= -\lambda_i \Omega, \quad h_{i,i+1} = h_{i+1,i} = \lambda_i \frac{J}{2} \\ k_{i,i+1} &= \lambda_i \frac{J}{2} = -k_{i+1,i}. \end{aligned}$$

Eq. (A.16) is a quadratic fermionic Hamiltonian which we can rewrite as

$$\mathcal{H}_{\mathrm{FF}} = \begin{pmatrix} \vec{c}^{\dagger} & \vec{c} \end{pmatrix} \begin{pmatrix} h & k \\ -k & -h \end{pmatrix} \begin{pmatrix} \vec{c} \\ \vec{c}^{\dagger} \end{pmatrix}$$

where $\vec{c} = (\hat{c}_i, \ldots, \hat{c}_N)$ and $\vec{c}^{\dagger} = (\hat{c}_i^{\dagger}, \ldots, \hat{c}_N^{\dagger})$. Since h and k are $N \times N$ matrices with real coefficients, they can be efficiently stored on a classical computer and solved using exact diagonalization for system sizes exceeding $N \sim 1000$. An intuitive explanation for why this works is that the dynamics reduce to particles traveling through the chain without scattering—in analogy to classical systems this problem is much easier to solve than if the particles had interactions leading to elastic or inelastic collisions.

To solve for the dynamics of the fermions, we consider the time evolution of the fermionic operators. This is governed by the Heisenberg equation of motion

$$\frac{\partial}{\partial t}\hat{A} = \mathrm{i}\left[\mathcal{H}_{\mathrm{FF}}, \hat{A}\right] \tag{A.17}$$

for any operator $\hat{A}$. We plug the fermionic operators into this equation and use $[\hat{A}\hat{B}, \hat{C}] = A\{\hat{B}, \hat{C}\} - \{\hat{A}, \hat{C}\}\hat{B}$ for any three operators $\hat{A}$, $\hat{B}$, and $\hat{C}$. We obtain

$$\begin{aligned} \frac{\partial}{\partial t}\hat{c}_i &= \mathrm{i}\left[\mathcal{H}_{\mathrm{FF}}, \hat{c}_i\right] \\ &= \mathrm{i}\left[\lambda_{i-1} J(\hat{c}_{i-1}^{\dagger} - \hat{c}_{i-1}) - \lambda_i 2\Omega \hat{c}_i + \lambda_i J(\hat{c}_{i+1}^{\dagger} + \hat{c}_{i+1})\right] \end{aligned} \tag{A.18}$$

for the annihilation operator $\hat{c}_i$ and

$$\begin{aligned}\frac{\partial}{\partial t}\hat{c}_i^\dagger &= \mathrm{i}\left[\mathcal{H}_{\mathrm{FF}}, \hat{c}_i^\dagger\right] \\ &= -\mathrm{i}\left[\lambda_{i-1}J(\hat{c}_{i-1} - \hat{c}_{i-1}^\dagger) - \lambda_i 2\Omega\hat{c}_i + \lambda_i J(\hat{c}_{i+1} + \hat{c}_{i+1}^\dagger)\right] = \left(\frac{\partial}{\partial t}\hat{c}_i\right)^\dagger \end{aligned} \tag{A.19}$$

for the creation operator $\hat{c}_i^\dagger$. This corresponds to $2N$ linear coupled differential equations of the form

$$\frac{\partial}{\partial t}\begin{pmatrix}\vec{c}\\ \vec{c}^\dagger\end{pmatrix} = \mathrm{i}\begin{pmatrix}\alpha & \beta\\ \beta^T & -\alpha\end{pmatrix}\begin{pmatrix}\vec{c}\\ \vec{c}^\dagger\end{pmatrix}$$

$$\text{with } A \equiv \begin{pmatrix}\alpha & \beta\\ \beta^T & -\alpha\end{pmatrix}$$

which has the solution

$$\begin{pmatrix}\vec{c}(t)\\ \vec{c}^\dagger(t)\end{pmatrix} = \mathrm{e}^{\mathrm{i}\,A\,t}\begin{pmatrix}\vec{c}(0)\\ \vec{c}^\dagger(0)\end{pmatrix}$$

for the initial operators $(\vec{c}(0), \vec{c}^\dagger(0))$. We note that β^T stands for the transpose of the matrix β. The elements of the block matrices α and β are

$$\alpha_{i,i} = \lambda_i 2\Omega, \alpha_{i,i+1} = \alpha_{i+1,i} = -\lambda J$$

$$\beta_{i,i+1} = -\lambda_i J = -\beta_{i+1,i}.$$

The time-evolved operators then take the form

$$\hat{c}_i(t) = \sum_j \Lambda_{i,j}(t)\hat{c}_j(0) + \Gamma_{i,j}(t)\hat{c}_j^\dagger(0) \tag{A.20}$$

$$\hat{c}_i^\dagger(t) = \sum_j \Gamma_{i,j}^*(t)\hat{c}_j(0) + \Lambda_{i,j}^*(t)\hat{c}_j^\dagger(0) \tag{A.21}$$

where we introduced the time evolution block matrices $\Lambda(t)$ and $\Gamma(t)$ such that

$$e^{iAt} = \begin{pmatrix} \Lambda(t) & \Gamma(t) \\ \Gamma^*(t) & \Lambda^*(t) \end{pmatrix}.$$

We can use Wick's theorem to evaluate expectation values for correlation functions of the form

$$\langle \mathrm{GS}|\hat{A}\hat{B}|\mathrm{GS}\rangle$$

where $\hat{A}$ and $\hat{B}$ are operators and $|\mathrm{GS}\rangle$ is the ground state with $\hat{c}_i(0)|\mathrm{GS}\rangle = 0$ for all $i = 1, \ldots, N$. Using Wick's theorem we find

$$\begin{aligned}
\langle \mathrm{GS}|\hat{c}_i(t)^\dagger c_j(t)|\mathrm{GS}\rangle &= (\Gamma^*\Gamma^T)_{ij}(t) \\
\langle \mathrm{GS}|\hat{c}_i(t) c_j(t)^\dagger|\mathrm{GS}\rangle &= (\Lambda\Lambda^\dagger)_{ij}(t) \\
\langle \mathrm{GS}|\hat{c}_i(t)^\dagger c_j(t)^\dagger|\mathrm{GS}\rangle &= (\Gamma^*\Lambda^\dagger)_{ij}(t) \\
\langle \mathrm{GS}|\hat{c}_i(t) c_j(t)|\mathrm{GS}\rangle &= (\Lambda\Gamma^T)_{ij}(t).
\end{aligned} \tag{A.22}$$

We can use this to calculate expectation values of the local energy density operator (cf. Eq. (1.9))

$$\begin{aligned}\hat{b}_i &= \frac{J}{2}\left(\lambda_i \hat{\sigma}_i^x \otimes \hat{\sigma}_{i+1}^x + \lambda_{i-1}\hat{\sigma}_{i-1}^x \otimes \hat{\sigma}_i^x\right) + \lambda_i \Omega \hat{\sigma}_i^z \\ &= \frac{J}{2}\Big[\lambda_i(\hat{c}_i^\dagger \hat{c}_{i+1} + \hat{c}_{i+1}^\dagger + \hat{c}_i^\dagger \hat{c}_{i+1}^\dagger + \hat{c}_{i+1}\hat{c}_i) \\ &\quad + \lambda_{i-1}(\hat{c}_{i-1}^\dagger \hat{c}_i + \hat{c}_i^\dagger + \hat{c}_{i-1}^\dagger \hat{c}_i^\dagger + \hat{c}_i \hat{c}_{i-1})\Big] + \lambda_i \Omega(1 - 2\hat{c}_i^\dagger \hat{c}_i). \end{aligned} \tag{A.23}$$

A significant limitation to this procedure is that the ground state $|\mathrm{GS}\rangle$ in Wick's theorem is given by the ground state of the fermionic operators $\hat{c}_i$. It turns out that this can be generalized to the ground state of an TFIM with any choice of parameters J, Ω in Eq. (A.13). The fermionic operators corresponding to the ground state $|\mathrm{GS}_b\rangle$ are $\hat{b}_i, \hat{b}_i^\dagger$. Then there exists a unitary mapping V connecting the two sets such that

$$\begin{pmatrix} \vec{c} & \vec{c}^\dagger \end{pmatrix}(0) = \begin{pmatrix} \alpha & \beta \\ \gamma & \delta \end{pmatrix} \begin{pmatrix} \vec{b} & \vec{b}^\dagger \end{pmatrix}(0).$$

It turns out that the time evolution operator changes as

$$A(t)' \equiv A(t)V = \begin{pmatrix} \Lambda(t) & \Gamma(t) \\ \Gamma^*(t) & \Lambda^*(t) \end{pmatrix} \begin{pmatrix} \alpha & \beta \\ \gamma & \delta \end{pmatrix} \equiv \begin{pmatrix} \nu(t) & \theta(t) \\ \zeta(t) & \chi(t) \end{pmatrix}.$$

Finally we just plug this into Eq. (A.22) to obtain the new result.

We used this method to perform conformal cooling in the transverse-field Ising model where we can reach system sizes up to $N \approx 1000$ with reasonable run times of a few minutes on a commercial laptop. For more details we refer to App. D.

B

Thermalization in Closed Quantum Systems

Thermalization is a process that one encounters regularly in their day-to-day life. To enjoy a cold, refreshing beverage on a warm summer day, one may put it in the refrigerator to cool it down. This empirical observation that physical system tend to equilibrate with their environment is a remarkable feature of statistical physics that is encapsulated by the second law of thermodynamics[57]: heat

flows from high-temperature to low-temperature regions. While there exist a lot different formulations of the second law of thermodynamics, they all share this property. This process describes well how macroscopic systems, e.g., a hot cup of tea, thermalize with their environment. The steady state has a uniform temperature which is determined by energy conservation of the entire system. One implication of the second law of thermodynamics is that the entropy of the entire system increases for spontaneous processes which essentially breaks time reversibility. While the process of thermalization is fairly well understood on a macroscopic scale, its microscopic nature in particular in quantum mechanical systems remains an open question.

A detailed review of thermalization in closed quantum systems would be beyond the scope of this thesis—instead we want to provide a practical perspective on arguments for thermalization in quantum many-body models with a focus on the *eigenstate thermalization hypothesis* (ETH). We will also comment on the role of integrability. For a more thorough review and more detailed analysis we refer the reader to the review article by D'Alessio et al. which acted as the basis for this appendix.

Thermalization in Classical Systems

Before we discuss nonequilibrium dynamics of isolated quantum systems it may be useful to give a short overview of thermalization in classical systems. A key feature is the ergodic hypothesis which states that the state of the system visits every point in phase space, that is compatible with constraints on the system, e.g., energy conservation, with equal probability for sufficiently long times. Chaos plays an intricate role in this process and is deemed an essential ingredient—meaning that a small perturbation to the initial condition can lead to arbitrarily large deviations at later times.

One thing to note is that adding an extensive number of constraints will generally result in ergodicity breaking because only a small subspace is accessible for the dynamics. It turns out that this

holds both in the classical and the quantum setting where we discuss it in the context of integrability.

The equal probability sampling of the phase space implies that the long-time averages of observables give a good estimate of microcanonical expectation values which are used for isolated systems. Strictly speaking the time scale to explore the entire compatible phase space grows exponentially in the degrees of freedom, implying that macroscopic thermalization may be an extraordinarily difficult process—of course empirical evidence suggests the opposite. A way to resolve this is by considering that there are *typical* states which make up the majority of the phase space and give roughly the same expectation value. For instance it is much more likely that N particles are uniformly distributed in a box than all of them ending up in one half and none in the other. This leads to the expected behavior that systems tend to thermalize quickly, as it is much more likely that the system evolves to a typical state resulting in the expected behavior. While the Poincaré recurrence theorem predicts the state will always return to a point in phase space which is arbitrarily close to the initial state, this also takes exponentially long and has little effect on the time averages of expectation values which are dominated by typical states.

Closed Quantum Qystems

Ultimately we are interested in the nonequilibrium dynamics of closed quantum systems and their behavior at long times. For this purpose we consider the Schrödinger equation which governs the time evolution of closed quantum system under a time-independent Hamiltonian H

$$\frac{\partial}{\partial t}|\psi(t)\rangle = -\mathrm{i}H|\psi(t)\rangle. \tag{B.1}$$

This is a linear differential equation for the state $|\psi(t)\rangle$. The solution is simply given by

$$|\psi(t)\rangle = \mathrm{e}^{-\mathrm{i}Ht}|\psi(0)\rangle, \tag{B.2}$$

where $|\psi(0)\rangle$ is the initial state of the system and $U(t) \equiv \mathrm{e}^{-\mathrm{i}Ht}$ is unitary. It is interesting to note that the Schrödinger equation lacks nonlinearity which is an essential ingredient for chaos in classical systems. While two trajectories in phase space which are initially close together will generically diverge, this is not true for quantum states. In fact, their overlap remains unchanged throughout the evolution

$$|\langle\varphi(t)|\psi(t)\rangle| = |\langle\varphi(0)|U^\dagger(t)U(t)|\psi(0)\rangle| = |\langle\varphi(0)|\psi(0)\rangle|$$

where $U^\dagger(t) = U^{-1}(t)$ is the Hermitian conjugate of the unitary matrix $U(t)$. Therefore, the trajectory of the quantum state is not a suitable analog of trajectories in phase space to probe chaotic dynamics. Therefore we need a different notion to describe chaotic quantum system as the classical description fails.

It turns out that it is useful to study how much a quantum state is delocalized in energy space, i.e., in terms of the eigenstates of the Hamiltonian, to resolve this problem. The energy eigenstates fulfill

$$H|n\rangle = E_n|n\rangle$$

with $E_n \in \mathbb{R}$ such that its time evolution under the Schrödinger equation becomes trivial

$$|n(t)\rangle = \mathrm{e}^{-\mathrm{i}E_n t}|n(0)\rangle.$$

Effectively these states only pick up a phase and remain stationary otherwise. The set of energy eigenstates forms a complete basis of the Hilbert space, $\sum_n |n\rangle\langle n| = \mathbb{I}$ such that we can decompose any state as a linear combination of $\{|n\rangle\}$

$$|\psi\rangle = \sum_n c_n |n\rangle.$$

Here $c_n = \langle n|\psi\rangle \in \mathbb{C}$ are complex coefficients and we require $\sum_n |c_n|^2 = 1$. The same holds for density matrices ρ which evolve as

$$\frac{\partial}{\partial t}\rho = -\mathrm{i}[H,\rho] \tag{B.3}$$

according to the von Neumann equation. In terms of the energy eigenstates the time-evolved density matrix becomes

$$\rho(t) = \sum_{m,n} \mathrm{e}^{\mathrm{i}(E_n - E_m)t} \rho_{nm}(0) |n\rangle\langle m| \tag{B.4}$$

where $\rho_{nm} = \langle n|\rho|m\rangle$. Since we are interested in the long-time dynamics, we study the density matrix averaged over late times

$$\tilde{\rho} = \lim_{t\to\infty} \frac{1}{t} \int_0^t \rho(t')dt' = \sum_n \rho_{nn} |n\rangle\langle n|$$

which is referred to as the diagonal ensemble. We would expect that this approximates microcanonical expectation values if the system thermalizes. A key insight is that this diagonal ensemble must be *delocalized* over the energy eigenstates for this to occur. This is motivated by the prediction that the energy eigenstates are effectively random for nonintegrable models, such that they take the role of the typical states that were considered in the classical setting. We note that this is a very subtle topic

but generally, and in particular for nonintegrable models, we expect the bulk of the energy eigenstates to be well described by random matrix theory. In analogy to a classical system, a quantum state thermalizes if it is delocalized across the spectrum.

There is a caveat to this line of thought however: under unitary evolution, such as the Schrödinger equation, a pure state will always remain pure. Therefore it is not immediately clear whether the argument concerning the diagonal ensemble still applies, as thermal states are described by mixed states. It turns out that this can understood in the context of the eigenstate thermalization hypothesis which provides a formal framework to study this topic. A key result is that, while the whole system may not thermalize, subsystems thermalize with the rest of the system such that expectation values of few-body observables approach thermal results.

Eigenstate Thermalization Hypothesis

We consider the evolution of some observable $\hat{O}$ in the basis of the Hamiltonian's eigenstates

$$\begin{aligned}\langle\psi(t)|\hat{O}|\psi(t)\rangle &= \sum_{n,m} c_n^* c_m \mathrm{e}^{\mathrm{i}(E_n-E_m)t}\langle n|\hat{O}|m\rangle \\ &= \sum_n |c_n|^2 O_{nn} + \sum_{\substack{n,m \\ n\neq m}} c_n^* c_m \mathrm{e}^{\mathrm{i}(E_n-E_m)t} O_{nm}\end{aligned} \tag{B.5}$$

where $O_{nm} = \langle n|\hat{O}|m\rangle$ and we used the decomposition of the state $|\psi(t)\rangle$ from Eq. (B.3). Requiring that the observable thermalizes, corresponds to the time average of this observable approaching the microcanonical prediction and fluctuations around that value to be small for late times. In the long-term average we would expect that the second term in Eq. (B.5) vanishes assuming a nonextensive number of degeneracies. Again, only the diagonal terms remain which is remiscent of the diagonal ensemble. A similar problem prevails however because the energy eigenvalues E_n are exponentially close together, so it may take exponentially long for the temporal average to vanish—this

time scale is also known as the *Heisenberg time*[9,40]. This is again in conflict with our expectation that systems thermalize relatively quickly.

The eigenstate thermalization hypothesis resolves this problem by making a particular ansatz for the matrix elements of the operator $\hat{O}$. The matrix elements of the operator $\hat{O}$ take the form (cf. Eq. (2.5))

$$O_{nm} = \delta_{nm} O(E_n) + \frac{1}{\sqrt{\rho(\bar{E})}} \xi_O(\bar{E}, \omega) R_{nm}. \tag{B.6}$$

Here δ_{nm} is the Kronecker delta, $O(E_n)$ is a smooth function of the energy E_n and $\rho(E)$ is the density of states at energy E. R_{ij} are elements of a random matrix with mean zero and unit variance. $\xi_{\mathcal{O}}(\bar{E}, \omega)$ is a smooth function of the average energy $\bar{E} = (E_n + E_m)/2$ and the energy difference $\omega = E_n - E_m$. R_{nm} are often taken to be Gaussian random variables. Crucially $O(E)$ is identical to the microcanonical expectation value at energy E.

Assuming validity of the ETH, it is easy to see from Eq. (B.5) that

$$\bar{O} = \lim_{t\to\infty} \frac{1}{t} \langle \psi(t) | \hat{O} | \psi(t) \rangle = \sum_n |c_n|^2 O_{nn} \approx O(E) \sum_n |c_n|^2 = O(E), \tag{B.7}$$

i.e., the long-time average approaches the microcanonical value. In practice this value is approached rapidly as the offdiagonal matrix elements average to 0 even in the presence of high degeneracy due to the form of R_{nm}. An interesting feature is that this result does not make assumptions regarding the form of the coefficients c_n. It only relies on properties of the energy eigenstates which encode a notion of ergodicity and typicality in the model.

While the ETH ansatz is motivated by random matrix theory, there is no universal understanding when this applies and when it fails. There is also no encompassing theory for the thermalization time of an observable. It is generally believed that it holds for all physical observables and that the

equilibrium value is approached relatively quickly. It is known however that the ETH fails for integrable models, which we will be the focus of our discussion in the following section.

Thermalization in Integrable Models

While the definition of integrability in quantum system is a subtle topic and still actively being discussed, following D'Alessio et al. we assume models to be integrable if they are subject to an extensive number of local conservation laws. For every such constraint there exists a local operator that commutes with the Hamiltonian. Every such operator corresponds to a conserved quantity, also known as the charge. The Hamiltonian, H, must then preserve each charge meaning that

$$\langle p|H|q\rangle = 0$$

where $|p\rangle, |q\rangle$ are states with different charges ($p \neq q$). This means that the Hamiltonian factorizes into disconnected blocks for each set of conserved properties. The defining feature is that the conserved quantities must be *local*. Trivially the Hamiltonian commutes with the projectors into each energy eigenstate resulting in an extensive number of conserved quantities which are however highly nonlocal. As an illustration a commonly encountered conserved quantity is the momentum for translation-invariant models, e.g., for periodic boundary conditions. $|p\rangle$ would then corresponds to a state with momentum eigenvalue p.

To find the steady state that describes the system's average long-term dynamics, we consider the state that maximizes the entropy subjected to the constraints—this is an implicit result from the second law of thermodynamics. As previously discussed, in the case of a few conserved quantities,

e.g., energy or momentum, this results in a Gibbs ensemble

$$\rho_{\mathrm{GE}} = \frac{\exp(-\beta H)}{\mathrm{Tr}\left(\exp(-\beta H)\right)},$$

where β is the inverse temperature of the state which determines the energy of the Gibbs ensemble. However for an extensive number of constraints, one finds that the state maximizing the entropy is instead a generalized Gibbs state

$$\rho_{\mathrm{GGE}} = \frac{\exp(-\sum_j \beta_j H_j)}{\mathrm{Tr}\left(\exp(-\sum_j \beta_j H_j)\right)},$$

where H_j are the conserved operators and β_j are parameters determined by the expectation value of ρ_{GGE}.

A plethora of integrable quantum models have been discovered including the spin-$\frac{1}{2}$ transverse-field Ising model and the spin-$\frac{1}{2}$ anisotropic Heisenberg model under certain conditions. These can be mapped to fermionic models using the Jordan-Wigner transformation with the resulting fermions exhibiting no interactions or specific interactions that factorize into two-body scattering. This means that the dynamics of the system can be reduced to single particles traversing the system with elastic collisions between them. This is a key difference to nonintegrable models where the collisions are inelastic leading to dispersion of energy between the individual degrees of freedom. We point out that the discussed properties manifest in the energy eigenstates leading to the failure of the ETH. Models close to integrablility can still exhibit traces of integrability leading to nonthermal behavior.

C

Mapping the Rydberg Atom Array Hamiltonian to a Spin-$\frac{1}{2}$ Model

The Hamiltonian in Eq. (1.6) can easily be mapped to a spin-$\frac{1}{2}$ model by exploiting that the Hamiltonian of any two-level system can be rewritten in terms of Pauli operators up to an irrelevant constant. The highly excited Rydberg state, $|\mathrm{r}\rangle$, and the electronic ground state, $|\mathrm{g}\rangle$, form the two-level

system. We map the two spin-$\frac{1}{2}$ states to the Rydberg states in the following way:

$$|\mathrm{g}\rangle \to |\downarrow\rangle \tag{C.1}$$

$$|\mathrm{e}\rangle \to |\uparrow\rangle. \tag{C.2}$$

For the number operator $\hat{n}$ in Eq. (1.6) we find that

$$\hat{n} = \frac{\hat{\sigma}^z + \mathbb{I}}{2} \tag{C.3}$$

where $\hat{\sigma}^z$ is the Pauli-z operator. We plug this result into the Rydberg atom array Hamiltonian and subsequently obtain

$$\begin{aligned}\mathcal{H} &= \sum_{i<j} \frac{C}{r_{ij}^6} \frac{\hat{\sigma}_i^z + \mathbb{I}}{2} \otimes \frac{\hat{\sigma}_j^z + \mathbb{I}}{2} + \sum_i \left(\frac{\Omega}{2} \hat{\sigma}_i^x - \Delta \frac{\hat{\sigma}_i^z + \mathbb{I}}{2} \right) \\ &= \sum_{i<j} \frac{1}{4} \frac{C}{r_{ij}^6} \hat{\sigma}_i^z \otimes \hat{\sigma}_j^z + \sum_i \left(\frac{\Omega}{2} \hat{\sigma}_i^x - \frac{\Delta}{2} \hat{\sigma}^z \right) + \sum_{i<j} \frac{1}{4} \frac{C}{r_{ij}^6} (\hat{\sigma}_i^z + \hat{\sigma}_j^z) + \text{const},\end{aligned} \tag{C.4}$$

where we discarded a constant term in the second line. Note that any summation over the indices i, j implies that we sum from $i, j = 1, \ldots, N$ unless explicitly stated otherwise. We use that $\sum_{i<j} = \frac{1}{2} \sum_{i \neq j}$

to simplify

$$
\begin{aligned}
&\sum_{i<j} \frac{1}{4} \frac{C}{r_{ij}^6} (\hat{\sigma}_i^z + \hat{\sigma}_j^z) \\
&= \frac{1}{2} \sum_i \frac{C}{4} \left(\sum_{j=1}^{i-1} \frac{1}{r_{ij}^6} + \sum_{j=i+1}^{N} \frac{1}{r_{ij}^6} \right) \hat{\sigma}_i^z \\
&+ \frac{1}{2} \sum_j \frac{C}{4} \left(\sum_{i=1}^{j-1} \frac{1}{r_{ij}^6} + \sum_{i=j+1}^{N} \frac{1}{r_{ij}^6} \right) \hat{\sigma}_j^z \\
&= \sum_i \frac{C}{4} \left(\sum_{\substack{j=1 \\ j \neq i}}^{N} \frac{1}{r_{ij}^6} \right) \hat{\sigma}_i^z .
\end{aligned}
$$

From the second to the third step the trick is identifying that the second and third line are identical up to exchange of i and j due to $r_{ij} = r_{ji}$. Combining this result with the rewritten terms in Eq. (C.4) we arrive at

$$
\mathcal{H} = \sum_{i<j} \frac{1}{4} \frac{C}{r_{ij}^6} \hat{\sigma}_i^z \otimes \hat{\sigma}_j^z + \sum_i \left\{ \frac{\Omega}{2} \hat{\sigma}_i^x + \left[\left(\frac{C}{4} \sum_{\substack{j=1 \\ j \neq i}}^{N} \frac{1}{r_{ij}^6} \right) - \frac{\Delta}{2} \right] \hat{\sigma}_i^z \right\} . \tag{C.5}
$$

In the limit of nearest-neighbor interactions, this corresponds to a mixed-field Ising model of the form

$$
\mathcal{H}_{\mathrm{MFIM}} = \sum_i \left(J^z \hat{\sigma}_i^z \otimes \hat{\sigma}_{i+1}^z + h^x \hat{\sigma}_i^x + h^z \hat{\sigma}_i^z \right) .
$$

Here we can identify the corresponding coefficients

$$\begin{aligned} J^z &= \frac{1}{4}\frac{C}{r_{i,i+1}^6} \\ h^x &= \frac{\Omega}{2} \\ h^z &= \frac{C}{2}\frac{1}{r_{i,i+1}^6} - \frac{\Delta}{2} = \frac{1}{2}(J-\Delta) \end{aligned} \tag{C.6}$$

in the case of periodic boundary conditions and for $J \equiv C/a^6$ with the interatomic distance a. For open boundary conditions, $h_{1,N}^z = J/4 - \Delta/2$ because the edge spins only have one nearest neighbor. Of course, this constitutes a finite-size effect. Most importantly, the mixed-field Ising model is nonintegrable in general, meaning that it is not exactly solvable. For $h^z = 0$ the model simplifies to the transverse-field Ising model which can be solved using the Jordan-Wigner transformation, resulting in a quadratic fermionic Hamiltonian (cf. App. A.2).

D

Scaling of Overcooling in the Critical Transverse-Field Ising Model

While it is numerically challenging to scale the chain lengths in the case of the Rydberg blockade Hamiltonian, we can use the spin-$\frac{1}{2}$ transverse-field Ising model (TFIM) as a paradigmatic model to study overcooling for large systems. While there are fundamental differences in these two models—integrability being one of them—, they share the same low-energy description at the critical point

between the paramagnetic and antiferromagnetic phases[68]. It is also noteworthy that Eq. (1.6) reduces to the transverse-field Ising model for $\Delta = J$ (cf. Eq. (C.6)). This motivates us to study conformal cooling quenches for the TFIM. The Hamiltonian is given by

$$\mathcal{H}_{\text{TFIM}} = J \sum_{i=1}^{N-1} \hat{\sigma}_i^{\text{x}} \otimes \hat{\sigma}_{i+1}^{\text{x}} + \Omega \sum_{i=1}^{N} \hat{\sigma}_i^{\text{z}}, \tag{D.1}$$

where $\hat{\sigma}^{\alpha}$ ($\alpha \in \{\text{x}, \text{y}, \text{z}\}$) are the Pauli spin-$\frac{1}{2}$ matrices. For $|J| \ll |\Omega|$ the ground state is paramagnetic due to the spins aligning with the magnetic field in the z-direction. $|J| \gg |\Omega|$ leads to antiferromagnetic order in the ground state for $J > 0$ and ferromagnetic order for $J < 0$. There is a critical point separating these two phases at $|J| = |\Omega|$ which is described by the 2D Ising CFT[68]. Slagle et al. find that this matches the CFT description of the critical point in the 1D Rydberg blockade model and show agreement in the low-energy spectrum of both models.

Eq. (D.1) can be mapped to free fermions using the Jordan-Wigner transformation[73], i.e., the model is integrable and has an extensive number of conservation laws. The dynamics can be reduced to N noninteracting particles which can be simulated efficiently[73].

In analogy to Eq. (1.8) we consider spatial modulations of Eq. (D.1)

$$\mathcal{H} = \sum_{i=1}^{N-1} \lambda_i \hat{\sigma}_i^{\text{x}} \otimes \hat{\sigma}_{i+1}^{\text{x}} + \sum_{i=1}^{N} \lambda_i \hat{\sigma}_i^{\text{z}}, \tag{D.2}$$

where $0 < \lambda_i \leq 1$ is the spatial modulation and we choose $J = \Omega = 1$ corresponding to the critical point between the paramagnetic and the antiferromagnetic phase. The spatial modulation of the Hamiltonian does not affect integrability so we can solve this Hamiltonian for large system sizes and long times using exact diagonalization—for numerical details we refer to App. A.2. Again, we consider long and shallow ramps with a slope $\alpha = 1.25 \times 10^{-3}$. We choose this slope to be so small, so we can go to system sizes between 100 and 1000 sites without violating the constraint $0 < \lambda_i \leq 1$.

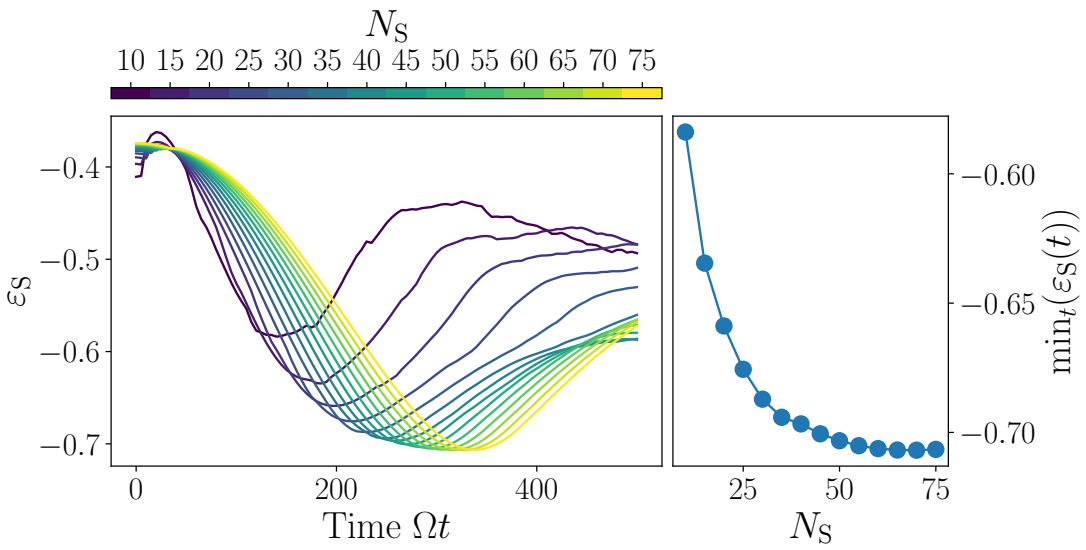

Figure D.1: Scaling of overcooling in the transverse-field Ising model for increasing system sizes N_S at a fixed system-ramp ratio $N_R/N_S = 10$ and ramp slope $\alpha = 1.25 \times 10^{-3}$. **a)** The average energy density in the system shows lower minima as the ramp size is increased. We observe saturation in the minimum beyond $N_S \gtrsim 80$. **b)** The optimal amount of cooling, $\min_t(\varepsilon_S(t))$, indeed saturates for large ramps, suggesting that overcooling can only remove a certain amount of energy.

We choose an easy-to-prepare initial state, a ground state in the paramagnetic region but close to the critical point ($J = -0.8$ and $\Omega = 1$), with an initial temperature that is similar to the ones considered in Ch. 1 ($T_i \sim 5$ in units of Ω).

We follow a similar procedure to the previous section: First, we fix the system size $N_S = 10$ and sweep the size of the ramp from $N_R = 10$ to $N_R \sim 100$. We observe significant overcooling in all of these cases and find an optimal system-ramp ratio of $N_R/N_S = 10$ beyond which there is little improvement in cooling.

Fig. D.1a) shows the average energy density in the system, ε_S, as a function of time as the system size is increased from $N_S = 10$ to 75—note that the ramp size is appropriately scaled to maintain $N_R/N_S = 10$. The definition for ε_S is completely analogous to the previous sections. We see qualitatively similar dynamics to the quenches at the Rydberg critical point for long and shallow

ramps: the energy in the system decreases rapidly before reabsorbing most of the emitted energy immediately afterwards. For larger chains the time to reach the minimum increases as one would expect. In Fig. D.1b) we plot the minimum of ε_S as a function of the system size. While there is a large improvement in the amount of cooling for smaller systems, this does not persist and saturation becomes evident in the thermodynamic limit. This underlines our finding that overcooling is a finite-size effect that does not provide an advantage over the thermodynamic expectation in the thermodynamic limit.

References

[1] The corresponding work was submitted in October 2023 but has not been published at the time of writing.

[2] Alves, R. F. (2022). *Realization of a Heisenberg XXZ spin system using Rydberg atoms*. PhD thesis, Ruperto-Carola-University of Heidelberg.

[3] Ashkin, A. & Laboratories, B. (2018). Optical Tweezers and their Application to Biological Systems.

[4] Bernien, H., Schwartz, S., Keesling, A., Levine, H., Omran, A., Pichler, H., Choi, S., Zibrov, A. S., Endres, M., Greiner, M., Vuletić, V., & Lukin, M. D. (2017). Probing many-body dynamics on a 51-atom quantum simulator. *Nature*, 551(7682), 579–584. Number: 7682 Publisher: Nature Publishing Group.

[5] Bluvstein, D., Levine, H., Semeghini, G., Wang, T. T., Ebadi, S., Kalinowski, M., Keesling, A., Maskara, N., Pichler, H., Greiner, M., Vuletić, V., & Lukin, M. D. (2022). A quantum processor based on coherent transport of entangled atom arrays. *Nature*, 604(7906), 451–456. Number: 7906 Publisher: Nature Publishing Group.

[6] Cardy, J. L. (1984). Conformal invariance and universality in finite-size scaling. *Journal of Physics A: Mathematical and General*, 17(7), L385.

[7] Chen, C., Bornet, G., Bintz, M., Emperauger, G., Leclerc, L., Liu, V. S., Scholl, P., Barredo, D., Hauschild, J., Chatterjee, S., Schuler, M., Läuchli, A. M., Zaletel, M. P., Lahaye, T., Yao, N. Y., & Browaeys, A. (2023a). Continuous symmetry breaking in a two-dimensional Rydberg array. *Nature*, 616(7958), 691–695. Number: 7958 Publisher: Nature Publishing Group.

[8] Chen, C., Chen, Y., & Wang, X. (2023b). Superdiffusive to Ballistic Transports in Nonintegrable Rydberg Chains. arXiv:2304.05553 [cond-mat].

[9] Colmenarez, L. (2022). *Fast, slow and super slow quantum thermalization*. PhD thesis, Max Planck Institute for the Physics of Complex Systems.

[10] Cottrell, W., Freivogel, B., Hofman, D. M., & Lokhande, S. F. (2019). How to Build the Thermofield Double State. *Journal of High Energy Physics*, 2019(2), 58. arXiv:1811.11528 [cond-mat, physics:hep-th, physics:quant-ph].

[11] D'Alessio, L., Kafri, Y., Polkovnikov, A., & Rigol, M. (2016). From quantum chaos and eigenstate thermalization to statistical mechanics and thermodynamics. *Advances in Physics*, 65(3), 239–362. Publisher: Taylor & Francis _eprint: https://doi.org/10.1080/00018732.2016.1198134.

[12] Daniel, A., Hallam, A., Desaules, J.-Y., Hudomal, A., Su, G.-X., Halimeh, J. C., & Papić, Z. (2023). Bridging quantum criticality via many-body scarring. *Physical Review B*, 107(23), 235108.

[13] Di Francesco, P., Mathieu, P., & Sénéchal, D. (1997). Finite-Size Scaling and Boundaries. In P. Di Francesco, P. Mathieu, & D. Sénéchal (Eds.), *Conformal Field Theory*, Graduate Texts in Contemporary Physics (pp. 409–438). New York, NY: Springer.

[14] Ebadi, S., Wang, T. T., Levine, H., Keesling, A., Semeghini, G., Omran, A., Bluvstein, D., Samajdar, R., Pichler, H., Ho, W. W., Choi, S., Sachdev, S., Greiner, M., Vuletić, V., & Lukin, M. D. (2021). Quantum phases of matter on a 256-atom programmable quantum simulator. *Nature*, 595(7866), 227–232. Number: 7866 Publisher: Nature Publishing Group.

[15] Eckner, W. J., Darkwah Oppong, N., Cao, A., Young, A. W., Milner, W. R., Robinson, J. M., Ye, J., & Kaufman, A. M. (2023). Realizing spin squeezing with Rydberg interactions in an optical clock. *Nature*, 621(7980), 734–739. Number: 7980 Publisher: Nature Publishing Group.

[16] Evered, S. J., Bluvstein, D., Kalinowski, M., Ebadi, S., Manovitz, T., Zhou, H., Li, S. H., Geim, A. A., Wang, T. T., Maskara, N., Levine, H., Semeghini, G., Greiner, M., Vuletić, V., & Lukin, M. D. (2023). High-fidelity parallel entangling gates on a neutral-atom quantum computer. *Nature*, 622(7982), 268–272. Number: 7982 Publisher: Nature Publishing Group.

[17] Feynman, R. P. (1982). Simulating physics with computers. *International Journal of Theoretical Physics*, 21(6), 467–488.

[18] Gao, P., Jafferis, D. L., & Wall, A. C. (2017). Traversable wormholes via a double trace deformation. *Journal of High Energy Physics*, 2017(12), 151.

[19] Goto, K., Guo, T., Nosaka, T., Nozaki, M., Ryu, S., & Tamaoka, K. (2023). Spatial deformation of many-body quantum chaotic systems and quantum information scrambling. arXiv:2305.01019 [cond-mat, physics:hep-th, physics:quant-ph].

[20] Goto, K., Nozaki, M., Tamaoka, K., Tan, M. T., & Ryu, S. (2021). Non-Equilibrating a Black Hole with Inhomogeneous Quantum Quench. arXiv:2112.14388 [cond-mat, physics:hep-th, physics:quant-ph].

[21] Gross, C. & Bloch, I. (2017). Quantum simulations with ultracold atoms in optical lattices. *Science*, 357(6355), 995–1001.

[22] Guéry-Odelin, D., Ruschhaupt, A., Kiely, A., Torrontegui, E., Martínez-Garaot, S., & Muga, J. (2019). Shortcuts to adiabaticity: Concepts, methods, and applications. *Reviews of Modern Physics*, 91(4), 045001.

[23] Halperin, B. I. (2019). Theory of dynamic critical phenomena | Physics Today | AIP Publishing.

[24] Hastings, M. B. (2007). An area law for one-dimensional quantum systems. *Journal of Statistical Mechanics: Theory and Experiment*, 2007(08), P08024.

[25] Hawking, S. W. (1975). Particle creation by black holes. *Communications in Mathematical Physics*, 43(3), 199–220.

[26] Ho, T.-L. & Zhou, Q. (2009). Squeezing out the entropy of fermions in optical lattices. *Proceedings of the National Academy of Sciences*, 106(17), 6916–6920. Publisher: Proceedings of the National Academy of Sciences.

[27] Ho, W. W., Choi, S., Pichler, H., & Lukin, M. D. (2019). Periodic Orbits, Entanglement, and Quantum Many-Body Scars in Constrained Models: Matrix Product State Approach. *Physical Review Letters*, 122(4), 040603. Publisher: American Physical Society.

[28] Jafferis, D., Zlokapa, A., Lykken, J. D., Kolchmeyer, D. K., Davis, S. I., Lauk, N., Neven, H., & Spiropulu, M. (2022). Traversable wormhole dynamics on a quantum processor. *Nature*, 612(7938), 51–55. Number: 7938 Publisher: Nature Publishing Group.

[29] Kaufman, A. M. & Ni, K.-K. (2021). Quantum science with optical tweezer arrays of ultracold atoms and molecules. *Nature Physics*, 17(12), 1324–1333. Number: 12 Publisher: Nature Publishing Group.

[30] Keesling, A., Omran, A., Levine, H., Bernien, H., Pichler, H., Choi, S., Samajdar, R., Schwartz, S., Silvi, P., Sachdev, S., Zoller, P., Endres, M., Greiner, M., Vuletić, V., & Lukin, M. D. (2019). Quantum Kibble–Zurek mechanism and critical dynamics on a programmable Rydberg simulator. *Nature*, 568(7751), 207–211. Number: 7751 Publisher: Nature Publishing Group.

[31] Khemani, V., Laumann, C. R., & Chandran, A. (2019). Signatures of integrability in the dynamics of Rydberg-blockaded chains. *Physical Review B*, 99(16), 161101.

[32] Kim, H. & Huse, D. A. (2013). Ballistic spreading of entanglement in a diffusive nonintegrable system. *Physical Review Letters*, 111(12), 127205. arXiv:1306.4306 [cond-mat, physics:quant-ph].

[33] Kim, K., Yang, F., Mølmer, K., & Ahn, J. (2023). Realization of an extremely anisotropic heisenberg magnet in rydberg atom arrays.

[34] Kirk, D. E. (2004). *Optimal Control Theory: An Introduction*. Courier Corporation. Google-Books-ID: fCh2SAtWIdwC.

[35] Kossow, M., Schupp, P., & Kettemann, S. (2012). CRITICAL EXPONENTS FOR ANTIFERROMAGNETIC SPIN CHAINS OBTAINED FROM BOSONISATION. *International Journal of Modern Physics: Conference Series*, 11, 183–190.

[36] Kuzmin, V., Zache, T. V., Kokail, C., Pastori, L., Celi, A., Baranov, M., & Zoller, P. (2022). Probing infinite many-body quantum systems with finite-size quantum simulators. *PRX Quantum*, 3(2), 020304. arXiv:2108.12378 [cond-mat, physics:quant-ph].

[37] Kuzmin, V. V. & Silvi, P. (2020). Variational quantum state preparation via quantum data buses. *Quantum*, 4, 290. arXiv:1912.11722 [quant-ph].

[38] Landau, Z., Vazirani, U., & Vidick, T. (2015). A polynomial time algorithm for the ground state of one-dimensional gapped local Hamiltonians. *Nature Physics*, 11(7), 566–569. Number: 7 Publisher: Nature Publishing Group.

[39] Lee, J. Y., Ramette, J., Metlitski, M. A., Vuletic, V., Ho, W. W., & Choi, S. (2023). Landau-Forbidden Quantum Criticality in Rydberg Quantum Simulators. *Physical Review Letters*, 131(8), 083601. arXiv:2207.08829 [cond-mat, physics:quant-ph].

[40] Lezama, T. L. M., Torres-Herrera, E. J., Pérez-Bernal, F., Bar Lev, Y., & Santos, L. F. (2021). Equilibration time in many-body quantum systems. *Physical Review B*, 104(8), 085117.

[41] Ljubotina, M., Desaules, J.-Y., Serbyn, M., & Papić, Z. (2023). Superdiffusive Energy Transport in Kinetically Constrained Models. *Physical Review X*, 13(1), 011033. arXiv:2210.01146 [cond-mat, physics:quant-ph].

[42] Lu, S., Bañuls, M. C., & Cirac, J. I. (2021). Algorithms for Quantum Simulation at Finite Energies. *PRX Quantum*, 2(2), 020321.

[43] Läuchli, A. M. & Schliemann, J. (2012). Entanglement spectra of coupled S = 1 2 spin chains in a ladder geometry. *Physical Review B*, 85(5), 054403.

[44] Maldacena, J. (2003). Eternal black holes in anti-de Sitter. *Journal of High Energy Physics*, 2003(04), 021.

[45] Maldacena, J. & Qi, X.-L. (2018). Eternal traversable wormhole. arXiv:1804.00491 [cond-mat, physics:gr-qc, physics:hep-th].

[46] Maldacena, J. & Stanford, D. (2016). Remarks on the Sachdev-Ye-Kitaev model. *Physical Review D*, 94(10), 106002.

[47] Matthies, A., Rudner, M., Rosch, A., & Berg, E. (2023). Programmable adiabatic demagnetization for systems with trivial and topological excitations. arXiv:2210.17256 [cond-mat, physics:quant-ph].

[48] Menchon-Enrich, R., Benseny, A., Ahufinger, V., Greentree, A. D., Busch, T., & Mompart, J. (2016). Spatial adiabatic passage: a review of recent progress. *Reports on Progress in Physics*, 79(7), 074401. Publisher: IOP Publishing.

[49] Mermin, N. D. & Wagner, H. (1966). Absence of Ferromagnetism or Antiferromagnetism in One- or Two-Dimensional Isotropic Heisenberg Models. *Physical Review Letters*, 17(22), 1133–1136.

[50] Moudgalya, S., Bernevig, B. A., & Regnault, N. (2022). Quantum many-body scars and Hilbert space fragmentation: a review of exact results. *Reports on Progress in Physics*, 85(8), 086501. Publisher: IOP Publishing.

[51] Olund, C. T., Yao, N. Y., & Kemp, J. (2023). Boundary Strong Zero Modes. arXiv:2305.16382 [cond-mat, physics:quant-ph].

[52] Paeckel, S., Köhler, T., Swoboda, A., Manmana, S. R., Schollwöck, U., & Hubig, C. (2019). Time-evolution methods for matrix-product states. *Annals of Physics*, 411, 167998.

[53] Peng, C. & Cui, X. (2022). Bridging quantum many-body scars and quantum integrability in Ising chains with transverse and longitudinal fields. *Physical Review B*, 106(21), 214311.

[54] Peschel, I. & Chung, M.-C. (2011). On the relation between entanglement and subsystem Hamiltonians. *Europhysics Letters*, 96(5), 50006.

[55] Poilblanc, D. (2010). Entanglement Spectra of Quantum Heisenberg Ladders. *Physical Review Letters*, 105(7), 077202.

[56] Raghunandan, M., Wolf, F., Ospelkaus, C., Schmidt, P. O., & Weimer, H. (2020). Initialization of quantum simulators by sympathetic cooling. *Science Advances*, 6(10), eaaw9268. Publisher: American Association for the Advancement of Science.

[57] Reichl, L. E. & Coppersmith, S. N. (1999). A Modern Course in Statistical Physics. *Physics Today*, 52(1), 65–66.

[58] Schiffer, B. F., Wild, D. S., Maskara, N., Cain, M., Lukin, M. D., & Samajdar, R. (2023). Circumventing superexponential runtimes for hard instances of quantum adiabatic optimization. arXiv:2306.13131 [cond-mat, physics:quant-ph].

[59] Scholl, P., Schuler, M., Williams, H. J., Eberharter, A. A., Barredo, D., Schymik, K.-N., Lienhard, V., Henry, L.-P., Lang, T. C., Lahaye, T., Läuchli, A. M., & Browaeys, A. (2021). Quantum simulation of 2D antiferromagnets with hundreds of Rydberg atoms. *Nature*, 595(7866), 233–238. Number: 7866 Publisher: Nature Publishing Group.

[60] Schollwöck, U. (2011). The density-matrix renormalization group in the age of matrix product states. *Annals of Physics*, 326(1), 96–192.

[61] Schuckert, A., Bohrdt, A., Crane, E., & Knap, M. (2023). Probing finite-temperature observables in quantum simulators of spin systems with short-time dynamics. *Physical Review B*, 107(14), L140410.

[62] Schuster, T., Kobrin, B., Gao, P., Cong, I., Khabiboulline, E. T., Linke, N. M., Lukin, M. D., Monroe, C., Yoshida, B., & Yao, N. Y. (2022). Many-Body Quantum Teleportation via Operator Spreading in the Traversable Wormhole Protocol. *Physical Review X*, 12(3), 031013.

[63] Seki, K. & Yunoki, S. (2020). Emergence of a thermal equilibrium in a subsystem of a pure ground state by quantum entanglement. *Physical Review Research*, 2(4), 043087.

[64] Semeghini, G., Levine, H., Keesling, A., Ebadi, S., Wang, T. T., Bluvstein, D., Verresen, R., Pichler, H., Kalinowski, M., Samajdar, R., Omran, A., Sachdev, S., Vishwanath, A., Greiner, M., Vuletić, V., & Lukin, M. D. (2021). Probing topological spin liquids on a programmable quantum simulator. *Science*, 374(6572), 1242–1247. Publisher: American Association for the Advancement of Science.

[65] Serbyn, M., Abanin, D. A., & Papić, Z. (2021). Quantum many-body scars and weak breaking of ergodicity. *Nature Physics*, 17(6), 675–685. Number: 6 Publisher: Nature Publishing Group.

[66] Shaw, A. L., Chen, Z., Choi, J., Mark, D. K., Scholl, P., Finkelstein, R., Elben, A., Choi, S., & Endres, M. (2023). Benchmarking highly entangled states on a 60-atom analog quantum simulator. arXiv:2308.07914 [physics, physics:quant-ph].

[67] Singh, K., Anand, S., Pocklington, A., Kemp, J. T., & Bernien, H. (2022). Dual-Element, Two-Dimensional Atom Array with Continuous-Mode Operation. *Physical Review X*, 12(1), 011040.

[68] Slagle, K., Aasen, D., Pichler, H., Mong, R. S. K., Fendley, P., Chen, X., Endres, M., & Alicea, J. (2021). Microscopic characterization of Ising conformal field theory in Rydberg chains. *Physical Review B*, 104(23), 235109. Publisher: American Physical Society.

[69] Stamper-Kurn, D. (2009). Shifting entropy elsewhere. *Physics*, 2, 80.

[70] Stoudenmire, E. & Schwab, D. J. (2016). Supervised Learning with Tensor Networks. In *Advances in Neural Information Processing Systems*, volume 29: Curran Associates, Inc.

[71] Stoudenmire, E. M. & White, S. R. (2010). Minimally entangled typical thermal state algorithms. *New Journal of Physics*, 12(5), 055026.

[72] Su, V. P. (2021). Variational preparation of the thermofield double state of the Sachdev-Ye-Kitaev model. *Physical Review A*, 104(1), 012427.

[73] Surace, J. & Tagliacozzo, L. (2022). Fermionic Gaussian states: an introduction to numerical approaches. *SciPost Physics Lecture Notes*, (pp.54).

[74] Sénéchal, D. (1999). An introduction to bosonization. arXiv:cond-mat/9908262.

[75] Tilly, J., Chen, H., Cao, S., Picozzi, D., Setia, K., Li, Y., Grant, E., Wossnig, L., Rungger, I., Booth, G. H., & Tennyson, J. (2022). The Variational Quantum Eigensolver: a review of methods and best practices. *Physics Reports*, 986, 1–128. arXiv:2111.05176 [quant-ph].

[76] Turner, C. J., Michailidis, A. A., Abanin, D. A., Serbyn, M., & Papić, Z. (2018). Weak ergodicity breaking from quantum many-body scars. *Nature Physics*, 14(7), 745–749. Number: 7 Publisher: Nature Publishing Group.

[77] van Dam, W., Mosca, M., & Vazirani, U. (2001). How powerful is adiabatic quantum computation? In *Proceedings 42nd IEEE Symposium on Foundations of Computer Science* (pp. 279–287). ISSN: 1552-5244.

[78] Vecsei, P. M., Lado, J. L., & Flindt, C. (2022). Lee-Yang theory of the two-dimensional quantum Ising model. *Physical Review B*, 106(5), 054402.

[79] Vitanov, N. V., Rangelov, A. A., Shore, B. W., & Bergmann, K. (2017). Stimulated Raman adiabatic passage in physics, chemistry, and beyond. *Reviews of Modern Physics*, 89(1), 015006.

[80] Wang, Y., Li, G., & Wang, X. (2021). Variational Quantum Gibbs State Preparation with a Truncated Taylor Series. *Physical Review Applied*, 16(5), 054035.

[81] Wang, Y., Zhang, X., Corcovilos, T. A., Kumar, A., & Weiss, D. S. (2015). Coherent Addressing of Individual Neutral Atoms in a 3D Optical Lattice. *Physical Review Letters*, 115(4), 043003.

[82] Wen, X., Fan, R., & Vishwanath, A. (2022). Floquet's refrigerator: Conformal cooling in driven quantum critical systems.

[83] White, C. D., Zaletel, M., Mong, R. S. K., & Refael, G. (2018). Quantum dynamics of thermalizing systems. *Physical Review B*, 97(3), 035127.

[84] White, S. R. (1992). Density matrix formulation for quantum renormalization groups. *Physical Review Letters*, 69(19), 2863–2866.

[85] Wilson, K. G. (1975). The renormalization group: Critical phenomena and the Kondo problem. *Reviews of Modern Physics*, 47(4), 773–840.

[86] Wu, J. & Hsieh, T. H. (2019). Variational Thermal Quantum Simulation via Thermofield Double States. *Physical Review Letters*, 123(22), 220502.

[87] Xia, T., Lichtman, M., Maller, K., Carr, A., Piotrowicz, M., Isenhower, L., & Saffman, M. (2015). Randomized Benchmarking of Single-Qubit Gates in a 2D Array of Neutral-Atom Qubits. *Physical Review Letters*, 114(10), 100503.

[88] Yao, Z., Pan, L., Liu, S., & Zhai, H. (2022). Quantum Many-Body Scars and Quantum Criticality. *Physical Review B*, 105(12), 125123. arXiv:2108.05113 [cond-mat].

[89] Ye, B., Machado, F., Kemp, J., Hutson, R. B., & Yao, N. Y. (2022). Universal Kardar-Parisi-Zhang Dynamics in Integrable Quantum Systems. *Physical Review Letters*, 129(23), 230602.

[90] Zaletel, M. P., Kaufman, A. M., Stamper-Kurn, D. M., & Yao, N. Y. (2021). Preparation of Low Entropy Correlated Many-body States via Conformal Cooling Quenches. *Physical Review Letters*, 126(10), 103401. arXiv:1611.04591 [cond-mat, physics:physics, physics:quant-ph].

[91] Zaletel, M. P., Mong, R. S. K., Karrasch, C., Moore, J. E., & Pollmann, F. (2015). Time-evolving a matrix product state with long-ranged interactions. *Physical Review B*, 91(16), 165112.

[92] Zeng, P., Sun, J., & Yuan, X. (2022). Universal quantum algorithmic cooling on a quantum computer. arXiv:2109.15304 [cond-mat, physics:quant-ph].

[93] Zhu, D., Johri, S., Linke, N. M., Landsman, K. A., Huerta Alderete, C., Nguyen, N. H., Matsuura, A. Y., Hsieh, T. H., & Monroe, C. (2020). Generation of thermofield double states and critical ground states with a quantum computer. *Proceedings of the National Academy of Sciences*, 117(41), 25402–25406. Publisher: Proceedings of the National Academy of Sciences.

[94] Šibalić, N. & Adams, C. S. (2018). *Rydberg Physics*. IOP Publishing.